INFORMATION TO USERS

This manuscript has been reproduced from the microfilm master. UMI films the text directly from the original or copy submitted. Thus, some thesis and dissertation copies are in typewriter face, while others may be from any type of computer printer.

The quality of this reproduction is dependent upon the quality of the copy submitted. Broken or indistinct print, colored or poor quality illustrations and photographs, print bleedthrough, substandard margins, and improper alignment can adversely affect reproduction.

In the unlikely event that the author did not send UMI a complete manuscript and there are missing pages, these will be noted. Also, if unauthorized copyright material had to be removed, a note will indicate the deletion.

Oversize materials (e.g., maps, drawings, charts) are reproduced by sectioning the original, beginning at the upper left-hand corner and continuing from left to right in equal sections with small overlaps.

Photographs included in the original manuscript have been reproduced xerographically in this copy. Higher quality 6" x 9" black and white photographic prints are available for any photographs or illustrations appearing in this copy for an additional charge. Contact UMI directly to order.

Computational Studies on the Properties and Reactions of Biological Radicals

by

Fuqiang Ban

Submitted in partial fulfillment of the requirements

for the degree of Doctor of Philosophy

at

Dalhousie University
Halifax, Nova Scotia
July, 2001

DALHOUSIE UNIVERSITY

FACULTY OF GRADUATE STUDIES

The undersigned hereby certify that they have read and recommend to the

Faculty of Graduate Studies for acceptance a thesis entitled "Computational

Studies on the Properties and Reactions of Biological Radicals" by Fuqiang Ban,

in partial fulfillment of the requirements for the degree of Doctor of Philosophy.

Dated: _____August 24, 2001_____

External Examiner:

Research Supervisor:

Examining Committee:
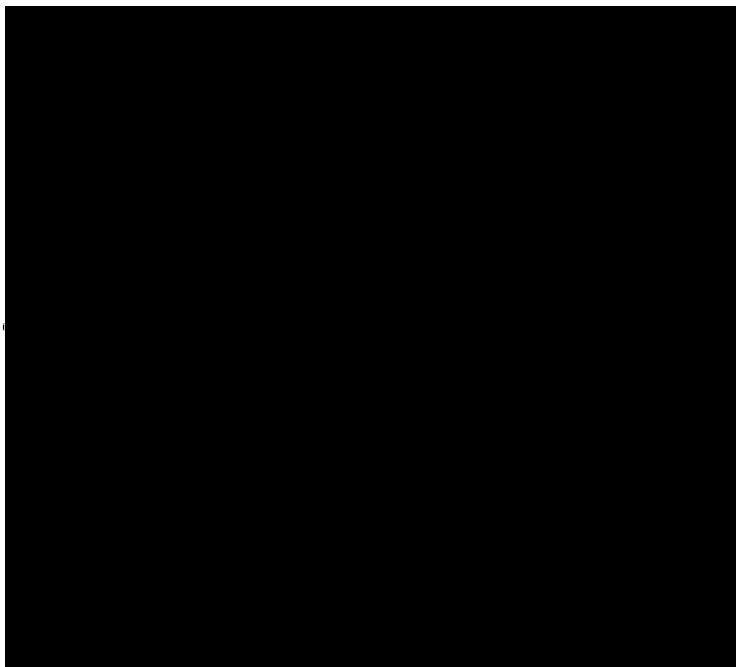
DALHOUSIE UNIVERSITY

Date: September 6, 2001

Author: _____ Fuqiang Ban _____

Title: _____ Computational Studies on the Properties and Reactions _____
_____ of Biological Radicals _____

Department or School: _____ Department of Chemistry _____

Degree: Ph. D.   Convocation: October   Year: 2001

Permission is herewith granted to Dalhousie University to circulate and to have copied for non-commercial purposes, at its discretion, the above title upon the request of individuals or institutions.

_____
Signature of Author

The author reserves other publication rights, and neither the thesis nor extensive extracts from it may be printed or otherwise reproduced without the author's written permission.

The author attests that permission has been obtained for the use of any copyrighted material appearing in this thesis (other than brief excerpts requiring only proper acknowledgement in scholarly writing), and that all such use is clearly acknowledged.

iii

To my family.

Contents

List of Figures

List of Schemes

List of Tables

Abstract

Numerous biological radical systems have been discovered that are fundamental to understanding the catalysis of enzymes, the oxidative damage to DNA and proteins, and the mechanisms of anticancer drugs. Spectroscopic techniques are powerful tools for monitoring radicals. However, highly reactive and short-lived radical species are extremely difficult to characterize in experiments. Fortunately, recent advancements in density functional theory offer a complementary approach to solving chemical problems for biological systems of reasonable sizes.

This thesis describes the application of density functional theory to predicting properties and reaction mechanisms of several biological radical systems. In the first part of the thesis, the structures and hyperfine coupling constants of a number of amino acid-derived radicals generated upon irradiation are investigated systematically. A valid computational scheme for obtaining the zwitterionic form of amino acid radicals is provided. The second part of the thesis concentrates on selected reaction mechanisms for the radical systems of DNA. In particular, the cross-linking mechanisms of a DNA base and an amino acid residue in a nucleohistone and the actions of an antitumor drug that leads to cleavage of DNA strands are investigated. The preferred mechanisms are identified on the basis of computed potential energy surfaces for possible reaction pathways, providing great insight into the radical-mediated oxidative damage to DNA and into the chemistry of tumor-selective drugs. The observations from the amino acid-derived and DNA-based radicals provide a fundamental basis for future work on biological radical systems.

List of Symbols

Ψ wave function

$\hat{H}$ total Hamiltonian

E energy

$\hat{T}$ kinetic energy operator

$\hat{V}$ potential energy operator

r_{ij} the distance between two particles

q_i electric charge

M_A the mass of the Ath nucleus

R_{AB} the distance between nuclei A and B

χ_i spin orbital

$\hat{F}$ Fock operator

ψ_i i^{th} molecular orbital

ε_i i^{th} orbital energy

$\hat{J}_j$ Coulomb operator

$\hat{K}_j$ exchange operator

ϕ_μ μ^{th} atomic orbital

$F_{\mu\upsilon}$ element of the Fock matrix

$P_{\mu\upsilon}$ element of the density matrix

$S_{\mu\upsilon}$ element of the overlap matrix

$C_{\mu i}$ expansion coefficient

$(\mu\upsilon|\lambda\sigma)$ two-electron integral

Φ_0 exact total molecular function

ν_i i^{th} vibrational frequency

a_0 radius of a fixed spherical cavity

ρ electron density

E_{xc}	exchange-correlation functional
$T[\rho]$	kinetic energy functional
$J[\rho]$	Coulomb repulsion energy functional
$V_{ee}[\rho]$	interelectronic potential energy functional
E_x	exchange functional
E_c	correlation functional
V_{eff}	effective potential
h	Planck's constant
ε	dielectric constant
g_e	electronic g-factor
β_e	electronic magneton
g_N	nuclear g-factor
β_N	nuclear magneton
$\rho^{\alpha-\beta}$	spin density
B	field strength
Z	nuclear charge
$\hat{S}$	electronic spin operator
S	electronic spin
$\hat{I}$	nuclear spin operator
I	nuclear spin
A_{iso}	isotropic hyperfine coupling constant
T_{ij}	ij^{th} component of the anisotropic hyperfine coupling tensor
α	alpha spin
β	beta spin

List of Abbreviations

HF	Hartree-Fock
UHF	Unrestricted Hartree-Fock
ROHF	Restricted open-shell Hartree-Fock
STO	Slater-type orbital
GTO	Gaussian-type orbital
CI	Configuration interaction
MRCI	Multi-reference configuration interaction
QCI	Quadratic configuration interaction
DFT	Density functional theory
LDA, LSDA	Local (spin) density approximation
GGA	Generalized-gradient approximation
HK	Hohenberg-Kohn
KS	Kohn-Sham
B	Becke's 1988 exchange functional
B3	Becke's hybrid exchange functional
PW86	Perdew and Wang's 1986 exchange functional
LYP	Lee, Yang and Parr's correlation functional
P86	Perdew's correlation functional
PW91	Perdew and Wang's 1991 correlation functional
SCRF	Self-consistent reaction field
PCM	Polarized continuum model
HFCC	Hyperfine coupling constant
ESR	Electron spin resonance
ENDOR	Electron-nuclear double resonance

Acknowledgements

First and foremost, I would like to extend my sincere thanks to my supervisor Professor Russell J. Boyd. His careful supervision, excellent guidance, constant support and continuous encouragement are greatly appreciated.

Special thanks go to Dr. L. A. Eriksson for starting me on the DNA-protein cross-linking project and for providing me with an opportunity to visit Uppsala. His ideas and insightful directions are precious inspiration. I would also like to thank Dr. Stacey D. Wetmore who stimulated my interests in the hyperfine interactions of biological radicals. Her knowledge on the hyperfine coupling tensor was a gift for my research on amino acid-derived radicals. Her assistance with my departmental seminar will never go without notice.

Special thanks go to Dr. James W. Gauld, a perfectionist, whose writing moral "Little extras make it better, simple is the best" had significant polarization effects on this thesis. His knowledge and skills in quantum chemistry and related software were the main sources of help when needed. His 'Mac-power' entertained me and made my graphical editing job easier. I would also like to thank Dr. Zhenming Hu for his support, patience and interesting discussions.

The other members of the Boyd group were extremely supportive during my studies. In particular, I would like to thank Dr. Kent Worsnop for his input, and Kathryn Rankin and Nelanie Mora-Diez for their cooperation, encouragement and friendship.

I would like to thank Maria Lundquist, Martin Agback, Bo Durbeej, Yani Wang, and Magnus Jansson for their hospitality and assistance during my stay in Sweden.

I am grateful to Drs Roderick Wasylisher, Philip D. Pacey, T. Bruce Grindley and Frances L. Cozens for their valuable advice. In addition, the assistance from Dr. Guy Bernard, Elizabeth Lewis and Hong Liang will never be forgotten.

The Killam Trust Fund and the Dalhousie Graduate Fellowship Fund are gratefully appreciated for their financial support.

Last but not least, I would like to extend my sincere thanks to my wife Yingxin and son Henry for their continuous understanding, encouragement and support.

Introduction

Biological radicals, species existing in living cells that contain one or more unpaired electrons, have become one of the most exciting topics in molecular biology.[1-3] The increasing interest in biological radicals is due in part to the realization of the importance of many radical reactions in normal cellular chemistry and to their role in the mechanisms of many toxins.[4] In particular, the discoveries of hypoxia-selective drugs that induce damage to tumors are noteworthy.[5-7]

Due to their central roles in cellular chemistry, DNA-[8] and protein-derived[9] radicals are of particular interest for understanding the functionality of biological radicals. In general, except for situations in which radicals act as catalytic centres of an enzyme, biological radicals in high concentration can seriously damage living organisms. The accumulation of damage in both DNA and proteins potentially induces various pathological conditions, for which cancer, Alzheimer's and many other diseases are of particular concern for human health. Hence, extensive experimental[8,10] and theoretical[11,12] studies have been performed on various biological radical systems.

In general, DNA and protein radicals originate by the attack of reactive oxygen species (ROS) of which the more common ones are the superoxide anion ($O_2^{-\bullet}$), hydroperoxyl ($HOO^\bullet$) and hydroxyl ($^\bullet OH$) radicals and hydrogen peroxide (H_2O_2). The

1

primary free radical in most oxygenated biological systems is O_2^- $^\bullet$, generated from the

electron transport chains of mitochondria, chloroplastic and endoplasmic reticulum.

Futhermore, biological systems may convert O_2^- $^\bullet$ to other reactive species such as

peroxyl ($ROO^\bullet$), alkoxyl ($RO^\bullet$) and $^\bullet OH$ radicals. The hydroxyl radical is the most

reactive and damaging of the ROS to both DNA and proteins. Hydroxyl radicals can be

generated by the Fenton reaction (I), UV radiation (II) or ionizing radiation (III)

$$\text{I.} \qquad Fe^{2+} + H_2O_2 \longrightarrow Fe^{3+} + {}^\bullet OH + OH^-$$

$$\text{II.} \qquad H_2O_2 \xrightarrow{\quad UV \quad} 2\,{}^\bullet OH$$

$$\text{III.} \qquad H_2O \xrightarrow{\quad \text{Ionizing radiation} \quad} H^\bullet + {}^\bullet OH$$
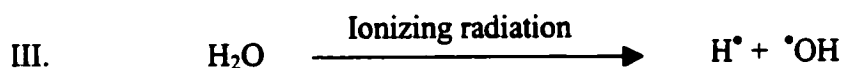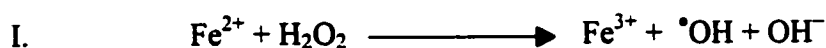
The attack of $^\bullet OH$ on DNA and proteins generates amino acid-, DNA base-, and

sugar-derived radical species. When the efficiency of repair enzymes decreases with age,

the reaction of these radicals with each other often leads to permanent alterations of DNA

or modifications of proteins.

While oxidative damage to DNA and proteins is recognized to be toxic towards

living cells, techniques have been developed that utilize the toxicity of biological radicals

for medical purposes. Radiation therapy is one of the first and most effective treatments

for many cancers. The high energy of radiation initially produces significant amounts of

$^\bullet OH$ radicals. When focused on tumors, further propagation of radical reactions can lead

to DNA strand breaks, thus destroying the tumor cells. Sugar radicals have been found to

be the crucial intermediates for DNA strand breaks, as illustrated below.
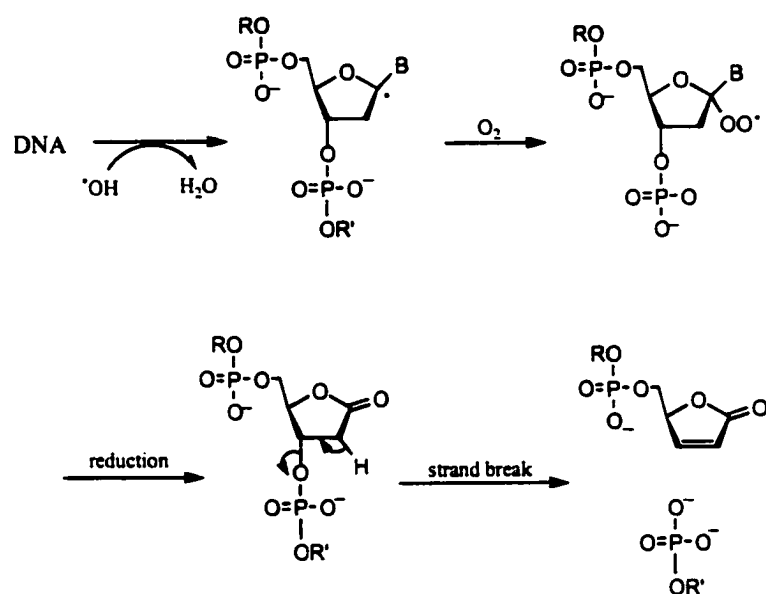
Figure 1.1 Single strand DNA break via a sugar radical.

The above mechanism depends on molecular oxygen. Unfortunately, many regions of solid tumors are found to be hypoxic, having a lower oxygen level than normal cells. Thus, radiation would more easily kill normal cells than hypoxic tumor cells. Hence, the development of hypoxia-selective antitumor drugs has attracted great attention. In particular, the combination of radiation with such drugs has shown high efficacy in experiments.[5-7]

A general feature of radical species is their high reactivity and short life-times. Thus, radical species are often extremely difficult to characterize experimentally. For computational chemistry, however, the study of such species is generally as straightforward as the study of conventional long-lived stable species.

The development of efficient density functional theory methods[13,14] and the emergence of faster computers have stimulated an increase in the application of the methods of computational chemistry in all branches of chemistry and biochemistry. The state-of-the-art of computational chemistry is the quantitative prediction of the properties and reaction mechanisms of important chemical systems. The work presented in this thesis focuses on computational studies of the properties and chemistry of biological radicals, in particular, oxidative damage or radiation induced DNA- and protein-derived radicals.

1.1 Thesis Summary

A brief overview of theoretical chemistry and of the methods employed in this thesis is presented in Chapter 2

In Chapter 3, the radicals which have been proposed to be formed upon irradiation of glycine crystals are investigated. The results suggest that the radicals are R1: $^+NH_3C^•HCOO^-$; R2: $^•CH_2COOH$; R3: $NH_2C^•HCOOH$ and R4: $NH_2CH_2COC^•HCOOH$. A C_s structure for R1, obtained using the Onsager model, gives hyperfine coupling constants in agreement with experiment. Hyperfine coupling constants computed for R2 are in agreement with unassigned experimental data. The computed hyperfine coupling constants for R4 are in good agreement with the experimental data previously assigned to the zwitterionic form $^+NH_3CH_2COC^•HCOO^-$. It is shown that the structure of R3 is influenced significantly by the glycine crystal environment. Protonation of R3 gives rise

to hyperfine couplings similar to the experimental values assigned to one conformer of R3.

In Chapter 4, the radiation products (radicals R1: $^\bullet$CH(CH$_3$)COOH, R2: H$_3$N$^+$C$^\bullet$(CH$_3$)COO$^-$ and R3: H$_2$NC$^\bullet$(CH$_3$)COOH) of L-α-alanine are investigated. Four conformers were found for R1 and R3. The zwitterionic form of radical R2 was obtained using the Onsager model. The relative energies of each of the four conformers of R1 and R3 show that structures with intramolecular hydrogen bonding are more stable. The computed hyperfine couplings are shown to be in good agreement with the results obtained from electron spin resonance spectroscopy. The effects of rotation about the N—C bond on the hyperfine coupling constants (HFCCs) of the amino protons in R2 support the previous suggestion that the amino protons are fixed by intermolecular hydrogen bonding in L-α-alanine crystals. Moreover, a good correlation between the structure of the amino group and HFCCs in the four conformers of R3 was found.

The radiation products of hydroxyproline have been investigated in Chapter 5. In the resulting radicals, the choice of the apical ring atom was found to be dependent on the nature and strength of the intramolecular hydrogen bonding. The observed hyperfine couplings previously assigned to two zwitterionic conformers of the hydroxyproline primary radical anion are found to be better described by its non-zwitterionic isomers and corresponding neutral protonated isomers. Similarly, the observed hyperfine couplings for radicals formed by cleavage of the C$_\alpha$—N bond (deamination) are in closest agreement with those calculated for their neutral forms. Theoretical proton hyperfine couplings support the experimental assignment of the radical cation formed by

decarboxylation and the radicals resulting from hydrogen abstraction from the C_2 and C_3 positions. The proton hyperfine couplings are sensitive to the conformations of the radicals, which in turn are highly dependent upon the extent of intramolecular hydrogen bonding.

The mechanisms for the formation of a cytosine-tyrosine cross-link in a nucleohistone are investigated in Chapter 6. The reactions are modelled by use of smaller systems of cytosine, phenol and the major radicals derived from their reactions with hydroxyl radicals. The calculated reaction potential energy surfaces suggest that the direct radical combination mechanism of the C_5-hydroxylated cytosine radical and tyrosyl radical is preferred over the radical addition mechanisms of both tyrosyl radical to cytosine and the C_5-hydroxylated cytosine radical to tyrosine. Water and hydrogen bonding interactions are suggested to play a key role in catalyzing the subsequent hydrogen transfer step of the reaction.

In Chapter 7, the experimentally proposed mechanisms by which the antitumor drug tirapazamine may react with a DNA sugar-C_1' radical to give the sugar derivative deoxyribonolactone, with concomitant DNA strand cleavage are investigated. For the previously proposed minor pathway, ionization of the sugar-C_1' radical by tirapazamine, the calculated ionization energy and the electron affinity of the models of the sugar-C_1' radical of DNA and tirapazamine suggest that tirapazamine must be protonated in order for it to be able to oxidize the sugar-C_1' radical. The preferred mechanism for reaction of tirapazamine with a sugar-C_1' radical, in agreement with experimental observations, is found to proceed by direct attack of an N-oxide oxygen of tirapazamine at the sugar-C_1'

position, followed by homolytic cleavage of the N—O bond of the drug moiety. Possible alternative mechanisms are also investigated.

Finally, global conclusions and possible directions for future research are provided in Chapter 8.

References

1. Stubbe J.; van der Donk, W. A. *Chem. Rev.* **1998**, *98*, 705.

2. Garrison, W. M. *Chem. Rev.* **1987**, *87*, 361.

3. Pogozelski, W. K.; Tullius, T. D. *Chem. Rev.* **1998**, *98*, 1089.

4. Halliwell, B.; Gutteridge, J. M. C. *Free Radicals in Biology and Medicine*, Oxford University Press Inc.: New York, 1999.

5. Denny, W. A.; Wilson, W. R. *Exp. Opin. Invest. Drugs* **2000**, *9*, 2889.

6. Brown, J. M. *Cancer Res.* **1999**, *59*, 5863.

7. Brown, J. M. *Br. J. Cancer* **1993**, *67*, 1163.

8. von Sonntag, C. *The Chemical Basis of Radiation Biology*, Taylor & Francis: London, 1987.

9. Dean, R. T.; Fu, S.; Stocker, R.; Davies, M. J. *Biochem. J.* **1997**, *324*, 1.

10. Varadarajan, S.; Kanski, J.; Aksenova, M.; Lauderback, C.; Butterfield, D. A. *J. Am. Chem. Soc.* **2001**, *123*, 5625.

11. Rauk, A.; Armstrong, D. A. *J. Am. Chem. Soc.* **2000**, *122*, 4185.

12. *Theoretical Biochemistry: Processes and Properties of Biological Systems*, Eriksson, L. A. Ed.; Elsevier: Amsterdam, 2001.

13. Hohenberg, P.; Kohn, W. *Phys. Rev. B* **1964**, *136*, 864.

14. Kohn, W.; Sham, L. J. *Phys. Rev. A* **1965**, *140*, 1133.

Theoretical Background

2.1 Introduction

Quantum chemistry is based on the laws of quantum mechanics and is being applied to an ever increasing range of chemical and biochemical problems. Theoretical chemistry, as it is often called, can provide an alternative independent approach to experiment for the chemist. It has opened great possibilities in describing the behaviour of electrons in atoms and molecules.

In principle, most chemical phenomena, if not all, can be predicted exactly. In practice, however, the fundamental equations of quantum chemistry cannot be solved exactly except for the simplest of systems, e.g., the hydrogen atom. However, this problem can be circumvented by application of various approximations, so that it is possible to obtain approximate, yet often highly accurate, results.

The development of density functional theory and the foundation of a hierarchy of well-calibrated computational methods are highlights of the progress in theoretical chemistry for the past several decades. In particular, the methods of theoretical chemistry can, in general, be applied as straightforwardly to reactive or transient species as they can to conventional long-lived species.

In this chapter, a brief overview of theoretical chemistry is given. In addition, some of the methods used in this thesis are described and their application in the investigation of various chemical properties is outlined.

2.2 The Schrödinger Equation

A fundamental postulate of quantum chemistry is that all information about a chemical system is described by some wave function Ψ. Essentially, most quantum chemical studies of chemical problems are concerned with the time-independent Schrödinger equation[1]

$$\hat{H}\Psi(r,R) = E\Psi(r,R) \tag{2.1}$$

where $\hat{H}$ is the Hamiltonian operator of the system. The Hamiltonian operator is the sum of kinetic energy ($\hat{T}$) and potential energy ($\hat{V}$) operators,

$$\hat{H} = \hat{T} + \hat{V} \tag{2.2}$$

The terms $\hat{T}$ and $\hat{V}$ are given by the expressions:

$$\hat{T} = -\sum_i \frac{h^2}{8\pi^2 m_i} \nabla_i^2 \tag{2.3}$$

$$\hat{V} = \sum_{i<j} \frac{q_i q_j}{r_{ij}} \tag{2.4}$$

where the sum is over all particles i (nuclei and electrons), m_i is the mass of particle i, h is Planck's constant, r_{ij} is the distance between two particles, and q_i and q_j are the electric charges of particles i and j, respectively. For electrons, $q_i = -e$ where e is the fundamental unit of charge (1.60210×10^{-19} C), while for a nucleus with atomic number Z_i, $q_i = +Z_i e$.

In atomic units the Hamiltonian operator for a system of n_E electrons and N_N nuclei is given by

$$\hat{H} = -\sum_{A=1}\frac{1}{2M_A}\nabla_A^2 - \sum_i \frac{1}{2}\nabla_i^2 - \sum_i \sum_A \frac{Z_A}{r_{iA}} + \sum_{i<j}\frac{1}{r_{ij}} + \sum_{A<B}\frac{Z_A Z_B}{R_{AB}} \qquad (2.5)$$

where, A, B and i, j are the indices for the N_N nuclei and the n_E electrons, respectively. M_A is the mass of the Ath nucleus and R_{AB} is the distance between nuclei A and B.

2.3 The Born-Oppenheimer Approximation and Electronic Problems

Because the Schrödinger equation (2.1) of molecular systems is generally too complicated to be solved exactly, approximations must be made to in order for it to be practically applicable.

The first common technique for simplifying the problem is to separate the nuclear and electronic motions based on the Born-Oppenheimer approximation.[2,3] Since the nuclei are much heavier and move much more slowly than the electrons, the electrons can be treated as moving in a field of fixed nuclei. As a consequence, the energy terms depending on the nuclear coordinates can be separated; that is, the nuclear kinetic term can be neglected and the nuclear potential term can be treated as a constant. Hence, the electronic Hamiltonian is given by

$$\hat{H}^{ele} = -\tfrac{1}{2}\sum_i \nabla_i^2 - \sum_i \sum_A \frac{Z_A}{r_{iA}} + \sum_{i<j}\frac{1}{r_{ij}} \qquad (2.6)$$

and the electronic form of the Schrödinger equation can be written as

$$\hat{H}^{ele}\Psi(r) = E^{ele}\Psi(r) \qquad (2.7)$$

where E^{ele} is the electronic energy. The total energy for a particular nuclear arrangement

is given by

$$E^{total}(R) = E^{ele} + \sum_{A<B} \frac{Z_A Z_B}{R_{AB}}$$ (2.8)

Equation (2.8) defines the molecular potential energy surface for different nuclear

configurations (see Section 2.9).

2.4 Hartree-Fock Theory

Due to the inseparable electron-electron repulsion term in (2.6), the electronic

Schrödinger equation (2.7) cannot be solved analytically for molecules with more than

one electron. Thus, the Hartree-Fock (HF) approximation, or the independent particle

model, was devised to break down the many-electron Schrödinger equation (2.7) into a

set of one-electron Hartree-Fock equations.

2.4.1 The Hartree-Fock Approximation

In the Hartree-Fock approximation,[3-5] all electrons in a molecule are assumed to

be independent. More specifically, any electron can be treated as a free electron moving

in an effective field of the other electrons where the electron-electron repulsion is treated

in an average way. Thus, the motion of each electron can be described by a single

electron wave function or the spin orbital (χ_i); a product of the molecular orbital (a spatial

function $\psi(r_i)$) and a spin function (α or β). If the spin orbitals are obtained for each

electron, a Hartree product of the spin orbitals can be constructed as a molecular wave

function. However, in order to satisfy the antisymmetry principle, the molecular wave function can be written as a Slater determinant

$$\Psi_0(1,2,...,N) = (N!)^{-\frac{1}{2}} |\chi_1(1)\chi_2(2)...\chi_N(N)| \tag{2.9}$$

where N is the number of electrons. Representation of the molecular wave function by a single Slater determinant (2.9) is the simplest approximation and is referred to as a single reference or single determinantal wave function.

Hartree-Fock theory is based on the variational method[3] of quantum mechanics. When a normalized single Slater determinant is used as a trial function for the ground state, the variational principle allows us to obtain the optimum approximate wave function by minimizing the expectation energy with respect to the spin orbitals without directly solving the Schrödinger equation. This mathematical treatment[4] leads to a set of Hartree-Fock (HF) equations.

$$\hat{F}\psi_i = \varepsilon_i \psi_i \qquad i = 1, 2, ..., N \tag{2.10}$$

$$\hat{F} = -\tfrac{1}{2}\nabla^2 - \sum_A \frac{Z_A}{r_A} + \sum_j (2\hat{J}_j - \hat{K}_j) \tag{2.11}$$

where $\hat{F}$ is the Fock operator and ε_i is the ith orbital energy. The sum over j is over the occupied orbitals. The summation of the Coulomb operator $\hat{J}_j$ and the exchange operator $\hat{K}_j$ describes the effective potential seen by the electron in the ith spin orbital.

Since the Fock operator in equation (2.10) has a functional dependence on the spin orbitals, the HF equations can only be solved by an iterative procedure.

2.4.2 The LCAO Approximation and the Roothaan-Hall Equations

The HF equations can be solved numerically for atoms with the corresponding solutions being the well-known atomic orbitals. However, numerical solution for molecules is impractical. Hence, Roothaan[6a] and Hall[6b] simplified the problem of solving the HF differential equations for molecules to that of solving a set of algebraic equations by using the LCAO approximation in which the unknown molecular orbitals (ψ_i) are expanded as a linear combination of a set of atomic orbitals $\{\phi_\mu\}$

$$\psi_i = \sum_{\mu}^{M} C_{\mu i}\phi_\mu \qquad (2.12)$$

where $C_{\mu i}$ is a coefficient and M is the number of atomic orbitals. The atomic orbitals used in the expansion are described by the basis set (see Section 2.5).

Substituting equation (2.12) into the HF equations (2.10), and applying the variational method leads to the Roothaan-Hall equations,

$$\sum_{\mu=1}^{M} C_{\mu i}(F_{\mu v} - \varepsilon_i S_{\mu v}) = 0 \qquad v = 1, 2, ..., M \qquad (2.13)$$

where $F_{\mu v}$ is an element of the Fock-matrix and $S_{\mu v} = \langle \phi_\mu | \phi_v \rangle$ denotes the overlap integral. For closed-shell molecules, $F_{\mu v}$ is defined by

$$F_{\mu v} = H_{\mu v} + \sum_{\lambda}\sum_{\sigma} P_{\lambda\sigma}[(\mu v | \lambda\sigma) - \tfrac{1}{2}(\mu\lambda | v\sigma)] \qquad (2.14)$$

$$H_{\mu v} = \langle \phi_\mu | -\tfrac{1}{2}\nabla^2 - \sum_{A}\frac{Z_A}{r_{1A}} | \phi_v \rangle \qquad (2.15)$$

where $P_{\lambda\sigma}$ $(=2\sum\limits_{i=1}^{occ}C_{\lambda i}C_{\sigma i})$ represents the density matrix and the $(\mu\nu|\pi\sigma)$ are the classical

electron-electron repulsion integrals defined by

$$(\mu\nu \mid \lambda\sigma) = \left\langle \phi_\mu(1)\phi_\nu(1)\left|\frac{1}{r_{12}}\right|\phi_\lambda(2)\phi_\sigma(2)\right\rangle \tag{2.16}$$

The $C_{\mu i}$ expansion coefficients can be obtained by standard matrix techniques.

For open-shell molecules, it is more appropriate to introduce different spin orbitals for electrons with different spins. The independent variation of two sets of coefficients leads to the unrestricted Hartree-Fock (UHF) formalism in which more flexibility is given to describe the interactions between same spin electrons and opposite spin electrons. Thus, UHF produces a better description for radical species and for the dissociation of molecules. The main deficiency of the UHF method is that the wave functions are not eigenfunctions of the spin operator $\hat{S}^2$, hence they contain spin contamination from higher multiplicities.

The restricted open-shell Hartree-Fock (ROHF) method is another possible HF-based approach for open-shell molecules. In ROHF all electrons are restricted to be paired except for the electrons in open-shell orbitals. The ROHF wave functions are eigenfunctions of the spin operator, however, the disadvantage of ROHF is that it raises the variational energy. Thus, the ROHF method is not as general and practical as the UHF approach. For example, ROHF does not provide a satisfactory description of bond breaking.

2.5 Basis Functions

As described in the previous section, when iteratively solving the Roothaan-Hall calculations for a molecule of interest, an approximate orbital wave function can be constructed by a linear combination of atomic orbitals of the constituent atoms of the molecule.

For describing the atomic orbitals, two types of functions[3,4] have received the most widespread use; Slater-type orbitals [an STO: $\phi_{nlm}^{STO} \propto r^{n-1} \exp(-\zeta r) Y_{lm}(\theta, \phi)$] and Gaussian-type orbitals, [a GTO: $\phi_{kmn}^{GTO} \propto x^k y^m z^n \exp(-\zeta r^2)$], where ζ depends on the type of orbitals, e.g., s, p, d ...

Both types of orbital have their advantages and weaknesses. Slater-type orbitals correctly describe the orbital cusp at the nucleus of an atom. However, STOs are expensive or impractical for computing electron-electron repulsion integrals for molecular systems. In contrast, Gaussian-type orbitals (GTOs) are computationally very efficient for electron-electron repulsion integrals; but GTOs have the wrong behavior both near and far from the nucleus. However, one can take a linear combination of GTOs $\{\phi_p^{GTO}\}$ to give a better description of an atomic orbital (ϕ_μ), i.e.,

$$\phi_\mu^{CGF} = \sum_{p=1}^{M} d_{p\mu} \phi_p^{GTO} \tag{2.17}$$

The coefficients $d_{p\mu}$ and the primitive GTO exponents are determined by minimizing the error in the fit of the M GTO's to the exact Slater orbital in a least squares sense. In particular, the optimized ratio of expansion coefficients of a particular set of primitive

GTOs is often fixed to approximate an STO basis function, known as the so-called contracted Gaussian-type basis function. Thus, we are able to use the computationally less-expensive GTOs while minimizing the error introduced by use of GTOs.

An infinite primitive GTO set would fit an atomic orbital precisely, however, one cannot use such a set. Hence, in practical applications, a hierarchy of finite contracted GTO basis sets has been developed.

To improve a basis set, polarization functions and diffuse functions may be included. Polarization functions are basis functions of higher angular momentum, while diffuse functions are basis functions with very small exponents. They can enhance the flexibility of a basis set for describing the anisotropic distribution of the electrons in a molecule. These functions are very important for higher level calculations.[7]

The well-known contracted Gaussian-type basis sets due to Pople and coworkers[8-10] are used throughout this thesis.

2.6 Electron Correlation

The general success of Hartree-Fock theory is due to the fact that the average interactions between electrons are the dominant part of electron-electron repulsion. As mentioned in Section 2.4.1, the HF molecular wave function takes the form of a Slater determinant, ensuring that electrons with the same spin are correlated. However, neither the HF molecular wave function nor the HF Hamiltonian considers the instantaneous correlation of electrons of opposite spin. Since every electron tends to avoid coming

close to another, neglect of the instantaneous electron correlation is a defect of Hartree-Fock theory. The total correlation energy is the difference between the exact nonrelativistic total energy and the HF energy obtained in the limit of a complete basis set,

$$E_{corr} = E^{exact} - E^{HF} \qquad (2.18)$$

Although the correlation energy is usually less than one percent of the total energy, electron correlation effects are often of great importance in quantitative predictions of molecular properties.

2.7 Conventional Correlated Methods

One way to account for electron correlation is to construct an accurate total molecular wave function based on the approximate HF Hamiltonian. One idea is to apply tractable approximations to truncate the exact wave function for desired accuracy. Many different approaches have been developed in wave function-based correlation theory, which are collectively referred to as the conventional correlated methods.

2.7.1 Configuration Interaction

Configuration interaction (CI) theory,[4,11,12] in which electron correlation effects are included by mixing configurations of excited states into the molecular wave function is conceptually the simplest approach. In CI theory, the excited state configurations are constructed using the HF Slater determinant for the ground state of a system as a single

reference. The determinant formed by moving only one electron from an occupied orbital of the HF configuration to a virtual orbital is called a singly excited configuration. Similarly, by multiple substitutions, doubly and higher excited configurations can be generated. According to the principle of superposition, the exact total molecular function, Φ_0, is given by a linear combination of all the possible configurations

$$\Phi_0 = C_0\Psi_0 + \sum_i C_i\Psi_i \tag{2.19}$$

where Ψ_0 is the HF configuration and the Ψ_i are excited configurations. All coefficients are varied to minimize the expectation value of the energy.

The energy obtained by a full CI treatment for a complete basis set corresponds to the exact non-relativistic energy of the molecular system. For a given basis set of N basis functions, the full CI (FCI) wave function and the corresponding full CI energy are the best possible.

2.7.2 Limited Configuration Interaction

While the full CI method will give, in principle, the exact solution to the Schrödinger equation, determining the full CI wave function using moderate basis sets is prohibitive even for small molecules. However, truncated CI methods, where only certain types of excitations are included in the CI wave function expansion (2.19), are suitable for studying various properties of chemical systems. The CIS method in which only single substitutions are included, may provide a proper description of one-electron properties such as dipole moment, while the CID method, in which only the doubly

excited configurations are included, may recover most of the correlation energy. The CISD method, in which all single and double substitutions are included, may further improve the results.

The CIS, CID and CISD methods are feasible for systems with a reasonably large number of electrons and basis functions. Furthermore, these methods are variational, i.e., the energy obtained is an upper bound to the exact energy. However, unlike the full CI method, the CID and CISD methods are not size-consistent, i.e., the energy calculated for a system composed of two fragments infinitely separated is not the same as the sum of the energies of the two separate fragments. This deficiency becomes increasingly apparent as the size of the system increases.

2.7.3 Multireference Configuration Interaction

The multireference configuration interaction method (MRCI) is one approach that may be taken to restore size-consistency by selectively including some triple- and quadruple-excited configurations. Firstly, the reference configurations are selected by a list of the more important excitation-determinants according to their energy contribution in a CISD calculation. Secondly, a subspace of all the singly and doubly excited configurations from the reference configurations is generated. Lastly, a predetermined energy threshold is often chosen for selecting important configurations from the subspace for the configuration interaction calculation. Thus, by systematically varying the basis set, reference space and energy threshold,[13,14] the MRCI method may approach the full

CI predictions using a reduced number of configurations. However, MRCI methods are not automated and too expensive for general application.

2.7.4 Quadratic Configuration Interaction

Quadratic configuration interaction (QCI) [15] is an effective approach developed by Pople and co-workers[15] to restore size consistency, and has found widespread application. QCI methods modify the wave function by adding quadratic terms. Thus, the QCISD method effectively includes contributions from all singles, doubles and some quadruples. However, the QCISD method takes inadequate account of the contributions of triple excitations. Because implementation of QCISDT for large systems is impractical, an approximate version, QCISD(T) has been devised by including the effects of triples via a perturbative approach. The QCI based methods are size-consistent, but not variational.

2.7.5 Møller-Plesset Perturbation Theory

An alternative approach to systematically recovering the correlation energy is Møller-Plesset (MP) perturbation theory,[16,17] in which the total Hamiltonian of the system (H) is written as the sum of a Hartree-Fock part (H_0) and a perturbation (λV):

$$H = H_0 + \lambda V \qquad (2.20)$$

The perturbation, V, is the difference between the exact Hamiltonian operator and the Hartree-Fock Hamitonian operator, i.e., the difference between the true interelectronic repulsion and the Hartree-Fock interelectronic potential.

According to Rayleigh-Schrödinger perturbation theory, the exact wave function

(Ψ) and energy (E) may be expanded as a Taylor series of λ. Thus, they can be written as

$$\Psi = \Psi^{(0)} + \lambda\Psi^{(1)} + \lambda^2\Psi^{(2)} + \ldots \tag{2.21}$$

and

$$E = E^{(0)} + \lambda E^{(1)} + \lambda^2 E^{(2)} + \ldots \tag{2.22}$$

The various orders of Møller-Plesset perturbation theory are obtained by setting λ

= 1, and truncating (2.21) and (2.22) to various orders.[3,4] The Møller-Plesset energy to

first-order corresponds to the Hartree-Fock energy. Corrections to the energy by

including the electron correlation are obtained by going to second order (MP2) and

higher-order MPn methods. The MP perturbation theory has the advantage of being size-

consistent, however, the energies are not variational.

Both configuration interaction methods and MP perturbation methods belong to

conventional correlated methods, which are based on determining the electronic wave

function. Computationally, they are often very expensive for incorporating the effects of

electron correlation.

2.8 Density Functional Theory

Density functional theory is an alternative approach to the electron correlation

problem. In comparison to the conventional correlated methods previously discussed,

density functional theory[18-20] looks at the molecular problem from a different perspective.

Only the average number of electrons located at any point in space is considered instead

of the motion of individual electrons. Density functional theory attempts to obtain all

information including the wave function from the electron density of the system. This simplicity of DFT has motivated many great developments in the past three decades.

2.8.1 Two Theorems of Density Functional Theory

The foundation, or the two fundamental theorems, of DFT were laid down by Hohenberg and Kohn (HK)[24] in 1964. The first theorem showed that the external potential v(r) of an N-electron system is uniquely determined by the electron density ρ(r); the Hamiltonian and wave function of the ground state depend only on the electron density. Thus, the energy of the system can be expressed as a functional of the density

$$E[\rho] = \int \rho(r)v(r)dr + T[\rho] + V_{ee}[\rho] \qquad (2.23)$$

where $T[\rho]$ is the kinetic energy and $V_{ee}[\rho]$ is the electron-electron interaction energy.

The second theorem is similar to the energy variation principle, in that for any trial electron density ρ'(r), the corresponding energy E[ρ'] is an upper bound to the exact energy of the ground state;

$$E[\rho'] \geq E[\rho] \qquad (2.24)$$

where E[ρ] is the true ground-state energy.

2.8.2 The Kohn-Sham Theory

In 1965, Kohn and Sham[25] founded the basis for practical applications of DFT by developing a theory in which the Schrödinger equation for an N-electron interacting

system is replaced with a set of single-particle equations that can provide the electron

density of the original system.

Setting up a non-interacting N electron reference system, Kohn and Sham

introduced N orbitals for N non-interacting electrons. The Hamiltonian is given by

$$\hat{H}_s = \sum_i^N -\tfrac{1}{2}\nabla_i^2 + V_N(r) \tag{2.25}$$

while the exact ground-state wave function is a normalized determinant

$$\Psi_s = \frac{1}{\sqrt{N!}}|\psi_1\psi_2...\psi_N| \tag{2.26}$$

where the ψ_i are the N lowest eigenfunctions of the one-electron Hamiltonian

$$\hat{h}_s = -\tfrac{1}{2}\nabla^2 + V_N(r) \tag{2.27}$$

$$\hat{h}_s\psi_i = \varepsilon_i\psi_i \tag{2.28}$$

The energy of the non-interacting system in the potential $V_N(r)$ can be obtained,

$$E_s[\rho] = T_s[\rho] + \int V_N(r)\rho(r)dr \tag{2.29}$$

where $T_s[\rho]$, the exact kinetic energy for the reference system, is given by

$$T_s[\rho] = \sum_i^N \langle\psi_i|-\tfrac{1}{2}\nabla^2|\psi_i\rangle \tag{2.30}$$

For the real interacting N-electron system, the classical Coulomb interaction $J[\rho]$

and the exchange-correlation energy $E_{xc}[\rho]$ need to be included. Thus, the total energy

of the real system is given by:

$$E[\rho] = T_s[\rho] + \int V_N(r)\rho(r)dr + J[\rho] + E_{xc}[\rho] \tag{2.31}$$

where $E_{xc}[\rho]$ is defined by

$$E_{xc}[\rho] = T[\rho] - T_s[\rho] + V_{ee}[\rho] - J[\rho] \tag{2.32}$$

and $T[\rho]$ is the exact kinetic energy functional of the real system. Thus, the effective potential can be written as

$$v_{eff}(r) = V_N(r) + \int \frac{\rho(r')}{|r - r'|} dr' + v_{xc}(r) \tag{2.33}$$

$$v_{xc}(r) = \frac{\delta E_{xc}[\rho]}{\delta \rho(r)} \tag{2.34}$$

where $v_{xc}(r)$ is the exchange-correlation potential.

Equation (2.28) allows a direct combination of the exact kinetic energy functional of the reference system and the effective potential of the real system, leading to the Kohn-Sham (KS) one-electron equations:

$$(-\tfrac{1}{2}\nabla^2 + v_{eff})\psi_i^{KS} = \varepsilon_i \psi_i^{KS} \qquad i=1, 2, ..., N \tag{2.35}$$

here the eigenfunction ψ_i^{KS} is the Kohn-Sham orbital. The electron density is obtained by

$$\rho(r) = \sum_i^N \left| \psi_i^{KS} \right|^2 \tag{2.36}$$

The KS equations (2.35) take a form analogous to the Hartree-Fock equations (2.10). When the LCAO approximation (2.12) is applied to the ψ_i^{KS}, the KS equations can be solved in exactly the same manner as the HF equations if the exchange-correlation functional $E_{xc}[\rho]$ in (2.34) is known.

Unfortunately, the exact form of $E_{xc}[\rho]$ is unknown. Thus, various models including the local density approximation (LDA)[18,19,23-25] and generalized gradient approximations (GGA)[26-31] have to be employed for practical calculations.

2.8.3 Local Density Approximation-based Functionals

In KS DFT theory, the first generation of effective approximate functionals for molecular purposes was based on the local spin density approximation (LSDA).[18,19,23] The LSDA exchange-correlation energy, is defined by

$$E_{xc}^{LSDA} = \int \rho(r) \varepsilon_{xc}^{LSDA} [\rho^\alpha (r), \rho^\beta (r)] dr \qquad (2.37)$$

where ε_{xc}^{LSDA} is the exchange correlation energy per particle. All explicit forms of E_{xc}^{LSDA} are obtained, based on the assumption that the E_{xc} can be separated into an exchange functional E_x and a correlation functional E_c. One such functional is SVWN, which is a linear combination of the Slater exchange term[24] and the correlation functional fitted by Vosko, Wilk and Nusair.[25] In general, LSDA performs fairly well. However, it grossly overestimates molecular bond energies.[29]

2.8.4 Generalized Gradient Approximation-based Functionals

To correct the non-uniformity of the electron density modelled by LSDA, the generalized gradient approximation (GGA) correction is introduced, in which the exchange-correlation functional depends explicitly on both the local densities and the local spin gradients, i.e.,

$$E_{xc}^{GGA} = \int [\rho^\alpha (r), \rho^\beta (r), \nabla \rho^\alpha (r), \nabla \rho^\beta (r)] dr \qquad (2.38)$$

The correlation corrections by Perdew (P86),[26] Lee, Yang, and Parr (LYP)[27], and by Perdew and Wang (PW91)[28] are in common use. In particular, the LYP functional provides a very good way to calculate correlation energies from electron densities.

The two most popular GGA-corrected exchange functionals are PW86[30] (Perdew and Wang) and B88 (Becke).[31]

2.8.5 Becke Half and Half Functional

Even the inclusion of GGA-correction to the LSDA approximations lacks chemical accuracy in thermochemical tests.[32] Inspired by the idea that exact-exchange-plus-LSDA-correlation improves certain atomic applications, Becke proposed a half and half theory based on an adiabatic connection formula.[33] The Becke half and half functional[34] is given by

$$E_{xc} = \tfrac{1}{2}E_x + \tfrac{1}{2}E_{xc}^{LSDA} \tag{2.39}$$

where E_x is the exact exchange in KS DFT theory and E_{xc}^{LSDA} is the exchange-correlation energy estimated by the LSDA approximation. The Becke half and half functional is reasonably successful for describing bond dissociation behaviour[35] and predicting reaction barrier heights.[36]

2.8.6 Becke's Three-parameter Hybrid Functional

Becke's three-parameter hybrid functionals are a linear combination of the exact HF exchange, LSDA for exchange-correlation, and the gradient corrections to exchange and correlation. The original functional[37a] is expressed by

$$E_{xc} = E_{xc}^{LSDA} + a_0\left(E_x^{exact} - E_x^{LSDA}\right) + a_x \Delta E_x^{B88} + a_c \Delta E_c^{PW91} \qquad (2.40)$$

The coefficients a_0, a_x and a_c were optimized to be 0.20, 0.72 and 0.81, respectively, by use of a standard set of thermochemical data. Combining Becke's hybrid exchange functional with various correlation functionals yields different DFT methods. For example, the B3LYP method[37ab] uses the LYP correlation functional.

Due to the inclusion of electron correlation, the DFT procedures are superior to HF methods. Gradient-corrected DFT, in particular Becke's three-parameter hybrid functional, often provides excellent results for molecular properties.

The principal advantages of DFT methods over the conventional correlated methods are the computational efficiency and the small disk requirements. At present, the DFT methods are the preferred choice for molecular systems that are too large to be treated by conventional correlated methods. One disadvantage of DFT is that when it fails there is no systematic way to improve the results as in the conventional correlated methods, other than improving the basis set used.

2.9 Exploring Potential Energy Surfaces

As shown in equation (2.8), within the Born-Oppenheimer approximation, the energy of a molecule can be considered as a function of the positions of the nuclei. Such functions define the potential energy surface of the molecule with all possible nuclear arrangements. Along the potential surface, the determination of equilibrium and transition structures is fundamental to understanding the chemistry of a molecular system. For example, Figure 2.1 shows the potential surface for an S_N2 reaction. Optimizing the equilibrium structures and transition structures for a reaction path is often a challenge in computational chemistry.
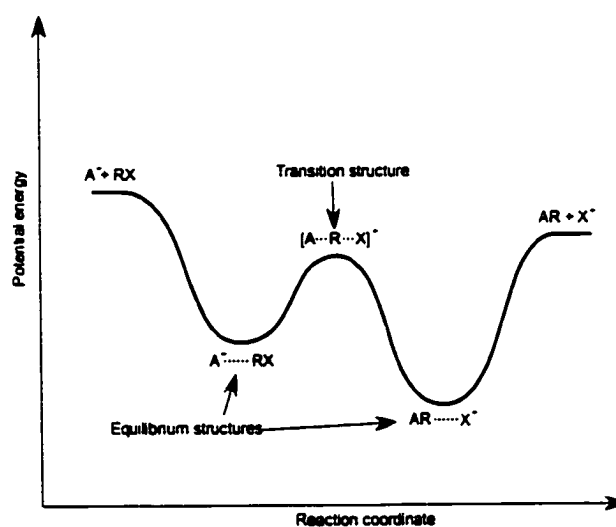
Figure 2.1 Schematic illustration of the potential energy surface for an S_N2 reaction in the gas phase illustrating equilibrium and transition structures.

2.9.1 Geometry Optimization

Mathematically, equilibrium structures and transition structures are stationary points on the potential energy surface where all first derivatives of the energy with respect to the 3N-6 internal coordinates of a molecular system of N nuclei are zero. They can be obtained analytically under the following requirements

$$\frac{\partial E}{\partial R_i} = 0 \qquad i = 1, 2, ..., 3N-6. \qquad (2.41)$$

2.9.2 Frequency Analysis

Equilibrium structures and transition structures are distinguished by examining the second derivatives of the energy, also referred to as the force constants,

$$\frac{\partial^2 E}{\partial R_i \partial R_j} \qquad i, j = 1, 2, ..., 3N-6. \qquad (2.42)$$

In practice, this is done by analysis of the harmonic vibrational frequency using standard methods.[38] Equilibrium structures are characterized by having all real frequencies because they are minima, while transition structures (first-order saddle points) have exactly one imaginary frequency.

2.9.3 The Zero Point Vibrational Energy Correction

An optimized equilibrium or transition structure is defined on the Born-Oppenheimer vibrationless potential energy surface, in a vacuum, at 0 K. When determining the relative energies of different species, the zero-point vibrational energy (ZPVE) should be included. The ZPVE is calculated as:

$$ZPVE = \frac{1}{2}\sum_i h\nu_i \qquad i = 1, 2, \ldots., n \qquad (2.43)$$

where ν_i is the ith vibrational frequency of the particular species. For transition structures, however, the imaginary frequency is not included in (2.43). Due to the neglect of anharmonicity and incomplete treatment of electron correlation, the calculated harmonic vibrational frequencies are often larger than the experimental vibrational frequencies (ν_i).[39,40] Thus, ZPVEs are often scaled by an appropriate factor obtained for the level of theory being used.

2.10 Approximation of Environmental Effects

The methods that have been discussed so far are for the gas phase without external environmental effects. While predictions for the gas phase are appropriate for systems that are weakly affected by an environment, approximation of specific environmental effects or bulk environmental effects must be included for a molecule whose nature is significantly modified or altered. For example, environmental effects

must be considered if one wishes to model a solvent-assisted reaction or obtain the zwitterionic structures of an amino acid in the solid state.

2.10.1 Reaction Field Models of Solvation

For chemical systems in solution, a common approach used for describing the electrostatic interaction between solute and solvent is the self-consistent reaction field (SCRF) approach. An advantage of the SCRF approach is that it models the bulk environmental effects at the same level of theory as the molecule is treated.

There are various SCRF methods implemented in GAUSSIAN 94[41a] and 98.[41b] They all treat the solvent as a polarizable medium with a dielectric constant, the magnitude of which is a measure of the polarity of the solvent. When a molecule of the gas phase is embedded in a cavity of the dielectric continuum, the dipole of the molecule will induce a dipole in the medium allowing them to interact electrostatically.
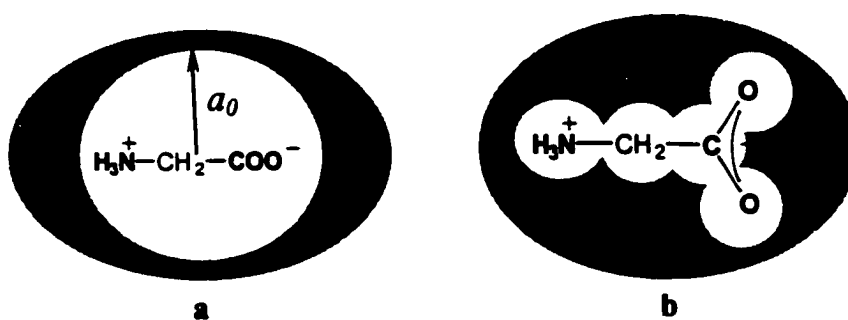
Figure 2.2 Schematic representation of the (a) Onsager model, and (b) polarized continuum model

The Onsager model[42,43] is the simplest method in the SCRF approach. In this method, the solute occupies a fixed spherical cavity (see Figure 2.2a) of radius a_0, which is estimated by calculation of the solute volume. Since the Onsager model is very

effective for geometry optimization and frequency calculations, it was combined with DFT methods for predicting zwitterionic radicals derived from amino acids in this thesis.

Another SCRF model that has been used for single point calculations in this thesis is the polarized continuum model (PCM).[44ab,45] The PCM differs from the Onsager model by defining a more realistic cavity (see Figure 2.2b) built with interlocking spheres centered on the atoms, thus enabling a more accurate description of the solvent effects. The effect of the polarization of the solvent continuum is calculated numerically. Thus, PCM provides a more accurate description of the solvent effect.

2.11 Hyperfine Structure: The Fingerprint of a Radical

The hyperfine structures displayed in an electron spin resonance (ESR) spectrum are the fingerprints of a radical species and may be reproduced by accurate theoretical calculations. As part of the research in this thesis is concerned with calculating the hyperfine structures of amino acid derived radicals, the basics of ESR[46] and the performance of theory[47] for interpreting the ESR spectrum are outlined.

2.11.1 Hyperfine Interaction

All radicals have one or more unpaired electrons with intrinsic spin. The possession by an electron of both a negative charge and spin gives rise to a magnetic moment for the unpaired electron,

$$\mu_e = -g_e\beta_e S \qquad (2.44)$$

where S is the electronic spin, and g_e and β_e are the electronic g-factor and magneton, respectively.

In addition to the unpaired electron, a radical may contain magnetic nuclei that are necessary for a measurement in magnetic resonance spectroscopy. These magnetic nuclei with nuclear spin and charge can provide other magnetic moments,

$$\mu_N = g_N \beta_N I \tag{2.45}$$

where I is the nuclear spin, and g_N and β_N are the nuclear g-factor and magneton, respectively.

As the unpaired electron is delocalized in a radical, there is a nonzero probability that the unpaired electron exists at the nucleus. Hence, the magnetic moment of the electron and a nucleus can interact, giving rise to the hyperfine interaction.

2.11.2 Isotropic and Anisotropic Hyperfine Coupling Constants

For a given nucleus, the hyperfine interaction can be described by the hyperfine coupling tensor A in the Hamiltonian of the hyperfine interaction,

$$\hat{H}_{hf} = \hat{I} \cdot A \cdot \hat{S} \tag{2.46}$$

where

$$A = \begin{bmatrix} A_{XX} & 0 & 0 \\ 0 & A_{YY} & 0 \\ 0 & 0 & A_{ZZ} \end{bmatrix} \tag{2.47}$$

The A_{ii} (i=X, Y and Z) are called the principal components of the hyperfine coupling tensor. The A tensor can be separated into two parts,

$$A = A_{iso} \cdot \begin{bmatrix} 1 & 0 & 0 \\ 0 & 1 & 0 \\ 0 & 0 & 1 \end{bmatrix} + \begin{bmatrix} T_{XX} & 0 & 0 \\ 0 & T_{YY} & 0 \\ 0 & 0 & T_{ZZ} \end{bmatrix} \qquad (2.48)$$

where A_{iso} is the isotropic hyperfine coupling constant describing the magnitude of the hyperfine interaction, and T_{XX}, T_{YY} and T_{ZZ} ($T_{XX} + T_{YY} + T_{ZZ} = 0$) are the anisotropic hyperfine coupling constants determining the orientation of the hyperfine interaction.

The isotropic hyperfine coupling arises from a quantum mechanical contact of the unpaired electron and the nucleus. Theoretically, A_{iso} can be calculated via the spin density at the nucleus,

$$A_{iso} = \frac{4}{3} g_e \beta_e g_N \beta_N < S_z >^{-1} \rho^{\alpha-\beta}(0) \qquad (2.49)$$

where $< S_z >^{-1}$ is the eigenvalue of the spin operator $\hat{S}_z$, and $\rho^{\alpha-\beta}(0)$ is the spin density at the nucleus. The units used for hyperfine coupling constants are typically gauss (G) or megahertz (MHz).

The anisotropic hyperfine coupling constants result from the electron-nuclear magnetic-dipole interactions and reflect the anisotropy of the spin distribution of a radical species. The ijth component of the anisotropic coupling can be computed from

$$T_{ij} = \frac{1}{2} g_e \beta_e g_N \beta_N < S_z >^{-1} \sum_{\mu\nu} \rho_{\mu,\nu}^{\alpha-\beta} < \phi_\mu \mid r_{kN}^{-5}(r_{kN}^2 \delta_{ij} - 3r_{kN,i} r_{kN,j}) \mid \phi_\nu > \qquad (2.50)$$

where $\rho_{\mu,\nu}^{\alpha-\beta}$ is an element of the spin density matrix.

2.11.3 Electron Spin Resonance

The hyperfine coupling constant is an observable in an applied magnetic field B. The interactions between the magnetic field and the electronic and nuclear magnetic moments, together with the hyperfine interaction, contribute to the spin Hamiltonian

$$\hat{H}_{spin} = g_e\beta_e B\cdot\hat{S} - g_N\beta_N B\cdot\hat{I} + \hat{I}\cdot A\cdot\hat{S} \qquad (2.51)$$

The first two terms in (2.51) represent the electronic and nuclear Zeeman interactions, respectively. Using the hydrogen atom in an applied magnetic field as an example, the energy splittings arising from the three terms in the spin Hamiltonian are shown schematically in Figure 2.3.
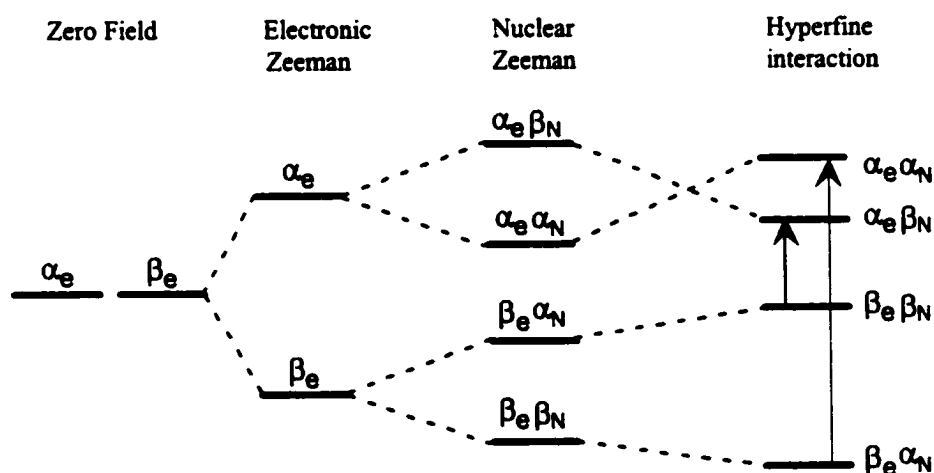
Figure 2.3 Schematic illustration of the splittings arising from various terms in the spin Hamiltonian for a hydrogen atom (α_e, β_e and α_N, β_N are the electronic and nuclear spin wave functions, respectively).

The spherical distribution of the unpaired electron of the H atom or the free tumbling of a radical in solution can average out the anisotopic components of the hyperfine couplings. The eigenvalues of the spin Hamiltonian for each spin state $m_s M_I$ are given by

$$E_{m_s M_I} = g_e \beta_e B_Z m_s - g_N \beta_N B_Z M_I + m_s M_I A_{iso} \qquad (2.52)$$

where m_s and M_I are the eigenvalues of $\hat{S}_Z$ and $\hat{I}_Z$, respectively, and Z is the direction of the applied magnetic field.

By applying another oscillating magnetic field perpendicular to the first static field, the $\Delta m_s = \pm 1$ and $\Delta M_I = 0$ of the selection rule allows transitions to be induced at two resonance frequencies

$$h\nu_{M_I} = g_e \beta_e B_Z + m_s M_I A_{iso} \qquad M_I = \pm \tfrac{1}{2}. \qquad (2.53)$$

This is the technique of electron spin resonance (ESR) by which the magnitude of the A_{iso} is measured as the absolute difference between the two resonance frequencies. However, the sign of the hyperfine coupling constants cannot be determined from ESR spectra. For the detection of a very small hyperfine coupling, the related technique of electron-nuclear magnetic double resonance (ENDOR) is more powerful. Similar to ESR transitions, ENDOR transitions are nuclear magnetic resonance transitions induced by applying an oscillating field, but at different frequencies. Using the above $S = \tfrac{1}{2}$ and $I = \tfrac{1}{2}$ system as an example, the selection rule of $\Delta M_I = \pm 1$ and $\Delta m_s = 0$ allows two nuclear magnetic resonances to be induced at

$$h\nu_{m_s} = -g_N \beta_N B_Z + m_s M_I A_{iso}, \quad m_s = \pm \tfrac{1}{2}. \qquad (2.54)$$

Analogous to ESR, ENDOR measures the A_{iso} as the difference of the two frequencies of nuclear magnetic resonance.

For radicals with N magnetic nuclei, the hyperfine interaction Hamiltonian is given by

$$\hat{H}_{hf} = \sum_{i=1}^{N} \hat{I}_i \cdot A_i \cdot \hat{S} \tag{2.55}$$

where the sum extends over all magnetic nuclei. As the number of coupled nuclei increases, ESR spectra become more complex. For complex spectra, ENDOR has the advantage of discriminating the hyperfine coupling constants arising from different magnetic nuclei in different radiofrequency ranges.

In the solid state, where a particular conformation of a radical is constrained, ESR or ENDOR spectra may provide both the isotropic and anisotropic hyperfine coupling constants for a given magnetic nucleus. This is extremely useful when trying to identify a radical species. However, solid-state ESR spectra are often complex with many overlapping lines and extremely difficult to interpret.

2.11.4 Performance of Theory for Calculating Hyperfine Interactions

Isotropic hyperfine coupling constants are related to the spin density at the nucleus. From a theoretical point of view, the origin of the spin density at a nucleus plays a key role in understanding the mechanisms of hyperfine coupling.

Sources of spin density have been traced[48] from the simplest ROHF method in which net contribution to spin density comes only from the singly occupied molecular

orbital being considered as the zero-order contribution. In comparison, in the UHF

formalism, each pair of electrons in a doubly occupied molecular orbital $\psi_i\alpha(j)\psi_i\beta(k)$ is

separately relaxed resulting in a configuration $\psi_i\alpha(j)\psi_{i'}\beta(k)$ in which the spatial orbital ψ_i

differs slightly from $\psi_{i'}$. As a consequence, electron k of β spin is more likely to be

polarized towards the unpaired electron than electron j of α spin. This phenomenon is

known as spin polarization. The difference between the UHF and ROHF spin densities is

considered as a first-order contribution. Higher-order contributions are due mainly to

electron correlation effects. Although the weight of each contribution may vary for

different radical species, a general trend can be easily seen by the performance of various

levels of theory using the CH radical as an example (Table 2.1).[47,48]

Table 2.1: Comparison of isotropic hyperfine coupling constants (MHz) for CH radical with various conventional methods in conjunction with the [9s6p5d1f/7s3p] basis set.

Method	^{13}C	^1H
ROHF	0.0	0.0
UHF	100.4	-84.4
MP2	37.4	-31.4
MP3	31.4	-58.0
MP4	35.0	-57.6
CIS	41.4	-57.1
CISD	30.0	-51.8
CISDT	45.8	-58.0
QCISD	43.7	-58.5
QCISD(T)	42.1	-57.2
MRCI	45.8	-58.5
exptl	46.8 ± 2.8	-57.7 ± 0.3

The results suggest that the erroneous behaviour of both the ROHF and UHF

methods arises from neglect of higher order corrections, while the good agreement with

experiment using the CIS method is due to cancellation of errors. Essentially, the

inclusion of single, double and triple excitations at the CISDT, MRCI or QCI levels of theory is necessary for obtaining accurate spin densities at the nuclei for isotropic hyperfine coupling constants. The performance of the theory is consistent with the fact that the probability of the unpaired electron appearing at a nucleus is physically associated with electron correlation.

As discussed previously, DFT methods may effectively include the electron correlation required for the calculation of hyperfine coupling constants. However, various combinations of the exchange functionals and correlation functionals may behave differently in obtaining the spin density. Because the spin density is insufficiently localized in LSDA, the resulting isotropic hyperfine couplings are often highly erroneous. The improvement from LSDA to GGA functionals mainly occurs for the heavy atoms for which the gradient corrections remove excess density from the tails of the core and the valence regions and place it in the core region of the atoms. Thus, GGA functions provide more reliable isotropic hyperfine couplings. In particular, extensive assessment[47,49] shows that the B3LYP and PWP86 functionals provide the most accurate hyperfine couplings so far. The relative accuracy of various DFT methods and QCISD for the hydroxyl radical is shown in Table 2.2.[50a-c]

Table 2.2: Comparison of calculated isotropic hyperfine coupling constants (G) calculated using various DFT methods and QCISD with experiment.

Method	SVWN[a]	PWP86[a]	B3LYP[a]	QCISD[b]	Exptl
^{17}O	-1.0	-17.5	-15.6	-17.3	-18.3
^{1}H	-21.4	-20.8	-22.1	-26.6	-26.2

[a] with IGLO-III. [b] with 6-311G+(2df,p).

Clearly, the PWP86 and B3LYP methods exhibit accuracy comparable with high-level conventional correlated methods.

The anisotropic hyperfine coupling components are integrated over all space rather than at only one point of the nucleus, thus, they are less sensitive to the quality of the method employed. At a level of theory that is suitable for the calculation of accurate isotropic hyperfine coupling, accurate anisotropic hyperfine coupling constants can certainly be obtained.

2.11.5 Basis Set Considerations for HFCC Calculations

The accurate description of the spin density at the nucleus for the isotropic hyperfine coupling constant demands high quality basis sets to be used at a suitable level of theory. Due to the deficiency of Gaussian functions not satisfying the cusp condition, a well-chosen basis set has to be used to obtain a good description of the core region. In particular, many s-functions and appropriate polarization functions must be included. In some cases, inclusion of diffuse functions may further improve the results. To meet these complicated requirements, basis sets of triple-zeta quality or better must be used to obtain accurate hyperfine coupling constants.

2.12 General Summary

The Hartree-Fock method is the simplest *ab initio* model that can be employed for studying chemical problems. The basis set used may be adjusted to obtain an improved

description of the molecular orbitals. The Hartree-Fock limit represents the best that can be done with a single electron configuration. The major deficiency of Hartree-Fock theory is its incomplete description of the correlation between the motions of the electrons.

Quantitative predictions often require going beyond the Hartree-Fock level. The conventional electron-correlation methods and the density functional theory are the two main approaches for incorporation of the effects of electron correlation.

A hierarchy of the conventional electron-correlation methods is best illustrated by a Pople diagram, such as shown in Figure 2.4. Following the hierarchy, the exact solution of the non-relativistic Schrödinger equation may be approached in a systematic manner. Such methods may be highly accurate, however, computationally they are often too expensive.

HF	MP2	...	CISD	...	QCI	...	...	Full CI

$\vdots$

6-31G(d)

6-31G(d,p)

6-31+G(d,p)

6-311G(d,p)

$\vdots$

6-311G(2df,p)

$\vdots$

HF limit

Improvement of electron correlation

Increasing basis set size

Exact solution
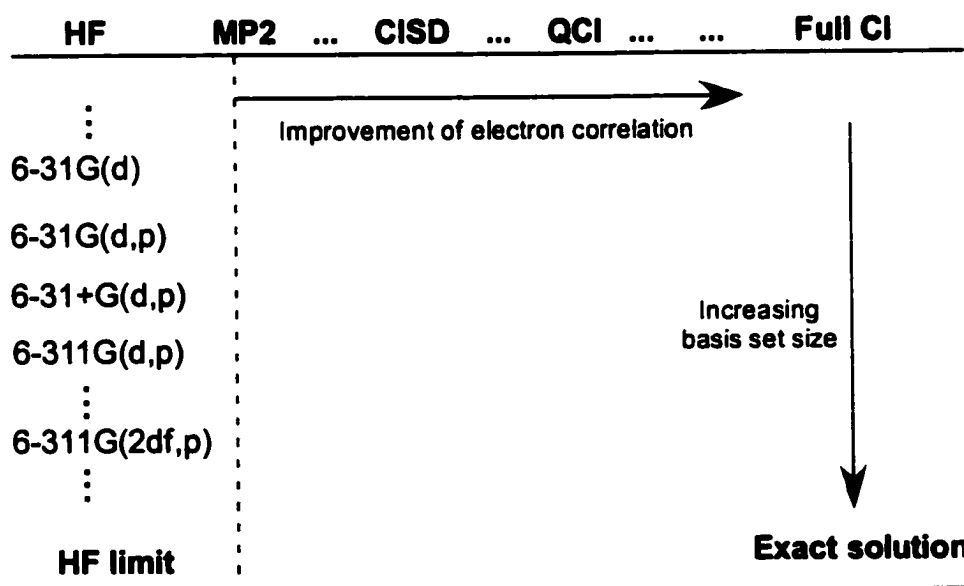
Figure 2.4 Hierarchy of conventional ab initio methods

It is not possible to construct a similar hierarchial diagram for the DFT methods. The accuracy of density functional theory methods depends on the density functional and also on the basis set used. Functionals, such as B3LYP, that have achieved chemical accuracy with some exceptions, are often the best choice for practical applications. Such methods are computationally less expensive than conventional electron correlation methods, being comparable in cost to Hartree-Fock level calculations. One more feature of the well-behaved DFT methods, such as B3LYP, is that they have been shown to often be less dependent on the size of the basis sets.

The level of theory being employed in a study is conventionally denoted as: method/basis set, e.g., B3LYP/6-31+G(d,p).

2.13 Practical Computational Scheme

Predicting electronic properties begins by searching for the optimal geometry of a molecular system. The reliability of any prediction depends on the quality of the optimized geometry. The molecular geometry depends only on the first derivatives of energy; reasonably accurate geometries can often be obtained at quite modest levels of theory. However, properties such as hyperfine coupling constants and the total energy of a radical species may only converge at a very high level of theory. Thus, single point calculations using more accurate methods with a larger basis set using a geometry obtained at a lower level of theory is often a sensible combination. This technique has been applied in this thesis to reduce computational cost, while maintaining reliable accuracy.

In such a combined computational scheme, the approach taken is conventionally written as

higher level (single point calculation)//lower level (geometry)

2.14 Technical Aspects

The calculations reported in this thesis were performed on IBM RS/6000 workstations in the Department of Chemistry, Dalhousie University and on the IBM SP parallel supercomputer of Dalhousie University. The Gaussian 94[41a] and Gaussian 98[41b] suites of programs were used for the geometry optimization and for obtaining the relative energies. The deMon programs[51] was used for calculating the hyperfine coupling constants.

In this thesis, the quantities reported are in the following units:

Property	Unit
Relative energy	kJ mol^{-1}
Hyperfine coupling constant	MHz
Bond length	angstrom (Å)
Angle	degree

The following conversion factors were used:

1 hartree (a.u.) = 2625.5 kJ mol^{-1}

1 gauss = 2.8025 MHz.

References

1. Schrödinger, E. *Ann. Physik* **1926**, *79*, 361.

2. Born, M.; Oppenheimer, J. R. *Ann. Physik* **1927**, *84*, 457.

3. Hehre, W. J.; Radom, L.; Schleyer, P. v. R; Pople, J. A. *Ab initio Molecular Orbital Theory*, John Wiley and Sons, 1986.

4. Szabo, A.; Ostlund, N. S. *Modern Quantum Chemistry: Introduction to Advanced Electronic Structure Theory*, Dover Publications, Inc., 1996.

5. Atkins, P. W.; Friedman, R. S. *Molecular Quantum Mechanics*, Oxford University Press, 1997.

6. (a) Roothaan, C. C. J. *Rev. Mod. Phys.* **1951**, *23*, 69. (b) Hall, G. G. *Proc. Roy. Soc. London A* **1951**, *205*, 541.

7. Davidson, E. R.; Feller, D. *Chem. Rev.* **1986**, *86*, 681.

8. (a) Ditchfield, R.; Hehre, W. J.; Pople, J. A. *J. Chem. Phys.* **1971**, *54*, 724. (b) Hehre, W. J.; Ditchfield, R.; Pople, J. A. *J. Chem. Phys.* **1972**, *56*, 2257. (c) Hariharan, P. C.; Pople, J. A. *Mol. Phys.* **1974**, *27*, 209. (d) Gordon, M. S. *Chem. Phys. Lett.* **1980**, *76*, 163. (e) Hariharan, P. C.; Pople, J. A. *Theor. Chim. Acta* **1973**, *28*, 213.

9. (a) Krishnan, R.; Binkley, J. S.; Seeger, R.; Pople, J. A. *J. Chem. Phys.* **1980**, *72*, 650. (b) McLean, A. D.; Chandler, G. S. *J. Chem. Phys.* **1980**, *72*, 563.

10. Frisch, M. J.; Pople, J. A.; Binkley, J. S. *J. Chem. Phys.* **1984**, *80*, 3265.

11. *Methods of Electronic Structure Theory*, Schaefer III H. F. Ed.; Plenum Press, 1977.

12. Levine, N. *Quantum Chemistry*, Allyn and Bacon Inc., 1983.

13. Buenker, R. J.; Peyerimhoff, S. D. *Theor. Chim. Acta* **1975**, *39*, 217.

14. Buenker, R. J.; Peyerimhoff, S. D. *Theor. Chim. Acta* **1974**, *35*, 33.

15. Pople, J. A; Head-Gordon, M.; Raghavachari, K. *J. Chem. Phys.* **1987**, *87*, 5968.

16. Møller, C.; Plesset, M. S. *Phys. Rev.* **1934**, *46*, 618.

17. (a) Krishnan, R.; Pople, J. A. *Int. J. Quantum Chem.* **1978**, *14*, 91. (b) Pople, J. A.; Krishnan, R.; Schlegel, H. B.; Binkley, J. S. *Int. J. Quantum Chem.* **1978**, *14*, 545. (c) Krishnan, R.; Frisch, M. J.; Pople, J. A. *J. Chem. Phys.* **1980**, *72*, 4244.

18. Parr, R. G.; Yang, W. *Density-Functional Theory of Atoms and Molecules*, Oxford University Press, 1989.

19. *Modern Density Functional Theory, A Tool for Chemistry*, Seminario, I. M.; Politzer, P., Eds.; Elsevier, 1995.

20. Parr, R. G.; Yang, W. *J. Phys. Chem.* **1996**, *100*, 12974.

21. Hohenberg, P.; Kohn, W. *Phys. Rev. B* **1964**, *136*, 864.

22. Kohn, W.; Sham, L. J. *Phys. Rev. A* **1965**, 140, 1133.

23. Ziegler, T. *Chem. Rev.* **1991**, *91*, 651.

24. Slater, J. C. *Quantum Theory of Molecules and Solids*, McGraw Hill: New York, 1974.

25. Vosko, S. H.; Wilk, L.; Nusair, M. *Can. J. Phys.* **1980**, *58*, 1200.

26. (a) Perdew, J. P. *Phys. Rev.* B. **1986**, *33*, 8822. (b) Perdew, J. P. *Phys. Rev.* B **1986** **34**, 7406.

27. Lee, C.; Yang, W.; Parr, R. G. *Phys. Rev.* B **1988**, *37*, 785.

28. Perdew, J. P.; Wang, Y. *Phys. Rev.* B **1992**, *45*, 13244.

29. *Density Functional Methods in Chemistry*, Labanowski, J. K.; Andzelm, J. W., Eds.; Springer: New York, 1991.

30. Perdew, J. P.; Wang, Y. *Phys. Rev.* B **1986**, *33*, 8800.

31. Becke, A. D. *Phys. Rev.* A **1988**, *38*, 3098.

32. Clementi, E.; Chakravorty, S. J. *J. Chem. Phys.* **1990**, 93, 2591.

33. (a) Harris, J.; Jones, R. O. *J. Phys.* F **1974**, *4*, 1170. (b) Gunnarsson, O.; Perdew, J. P. *J. Phys.* F. **1977**, *15*, 2884. (c) Harris, J. *Phys. Rev.* A **1984**, *29*, 1648.

34. Becke, A. D. *J. Chem. Phys.* **1993**, *98*, 1372.

35. Zhang, Y; Yang, W. *J. Chem. Phys.* **1998** *109*, 2604.

36. Lynch, B. J.; Truhlar, D. G. *J. Phys. Chem.* A **2001**, *105*, 2936.

37. (a) Becke, A. D. *J. Chem. Phys.* **1993**, *98*, 5648. (b) A slightly modified form of the original three-parameter hybrid is implemented in the Gaussian programs: Stephens, P. J.; Devlin, F. J.; Chablowski, C. F.; Frisch, M. J. *J. Phys. Chem.* **1994**, *98*, 11623.

38. Wilson, E. B.; Decius, J. C.; Cross, P. C. *Molecular Vibrations*, McGraw-Hill: New York, 1955.

39. Scott, A. P.; Radom, L. *J. Phys. Chem.* **1996**, *100*, 16502.

40. Schaefer, H. F.; Thomas, J. R.; Yamaguchi, Y.; DeLeeuw, B. J.; Vacek, G. In *Modern Electronic Structure Theory, Part I*; Yarkony, D. R. Ed.; World Scientific Publishing: Singapore, 1995; Vol. 2.

41. (a) Frisch, M. J.; Trunks, G. W.; Schlegel, H. B.; Gill, P. M. W.; Johnson, B. G.; Robb, M. A.; Cheeseman, J. R.; Keith, T. A.; Petersson, G. A.; Montgomery, J. A.; Raghavachari, K.; Al-Laham, M. A.; Zakrzewski, V. G.; Ortiz, J. V.; Foresman, J. B.; Cioslowski, J.; Stefanov, B.B.; Nanayakkara A.; Challacombe, M.; Peng, C. Y.; Ayala, P. Y.; Chen, W.; Wong, M. W.; Andres, J. L.; Replogle, E. S.; Gomperts, R.; Martin, R. L.; Fox, D. J.; Binkley, J. S.; DeFrees, D. J.; Baker, J.; Stewart, J. P.; Head-Gordon, M.; Gonzalez, C.; Pople, J. A. GAUSSIAN 94, Gaussian Inc.: Pittsburgh, PA, 1995. (b) Frisch, M. J.; Trucks, G. W.; Schlegel, H. B.; Scuseria, G. E.; Robb, M. A.; Cheeseman, J. R.; Zakrzewski, V. G.; Montgomery, J. A.; Stratmann, R. E.; Burant, J. C.; Dapprich, S.; Millam, J. M.; Daniels, A. D.; Kudin, K. N.; Strain, M. C.; Farkas, O.; Tomasi, J.; Barone, V.; Cossi, M.; Cammi, R.; Mennucci, B.; Pomelli, C.; Adamo, C.; Clifford, S.; Ochterski, J.; Petersson, G. A.; Ayala, P. Y.; Cui, Q.; Morokuma, K.; Malick, D. K.; Rabuck, A. D.; Raghavachari, K.; Foresman, J. B.; Cioslowski, J.; Ortiz, J. V.; Stefanov, B. B.; Liu, G.; Liashenko, A.; Piskorz, P.; Komaromi, I.; Gomperts, R.; Martin, R. L.; Fox, D. J.; Keith, T. A.; Al-Laham, M. A.; Peng, C. Y.; Nanayakkara, A.; Gonzalez, C.; Challacombe, M.; Gill, P. M. W.; Johnson, B. G.; Chen, W.; Wong, M. W.; Andres, J. L.; Head-Gordon,

M.; Replogle, E. S.; Pople, J. A. GAUSSIAN 98; Gaussian, Inc.: Pittsburgh, PA, 1998.

42. Onsager, L. *J. Am. Chem. Soc.* **1936**, 58, 1486.

43. (a) Wong, M. W.; Frisch, M. J.; Wiberg, K. B. *J. Am. Chem. Soc.* **1991**, *113*, 4776. (b) Wong, M. W.; Wiberg, K. B.; Frisch, M. J. *J. Am. Chem. Soc.* **1992**, *114*, 523. (c) Wong, M. W.; Wiberg, K. B.; Frisch, M. J. *J. Am. Chem. Soc.* **1992**, *114*, 1645. (d) Wong, M. W.; Wiberg, K. B.; Frisch, M. J. *J. Chem. Phys.* **1991**, *95*, 8991.

44. (a) Miertus, S.; Scrocco, E.; Tomasi, J. *Chem. Phys.* **1981**, *55*, 117. (b) Miertus, S.; Tomasi, J. *Chem. Phys.* **1982**, *65*, 239.

45. Cossi, M.; Borone, V.; Cammi, R.; Tomasi, J. *Chem. Phys. Lett.* **1996**, *255*, 237.

46. (a) Weltner Jr., W. *Magnetic Atoms and Molecules*, Van Nostrand: New York, 1983. (b) Atherton, N. M. *Principles of Electron Spin Resonance*, Ellis Horwood Limited: England, 1993.

47. Engels, B.; Eriksson, L. A.; Lunell, S. *Adv. Quantum Chem.* **1996**, *27*, 297.

48. Chipman, D. M. *Theor. Chim. Acta* **1992**, *82*, 93.

49. Gauld, J. W.; Eriksson, L. A.; Radom, L. *J. Phys. Chem. A* **1997**, *101*, 1352.

50. (a) Wetmore, S. D.; Boyd, R. J.; Eriksson, L. A. *J. Chem. Phys.* **1998**, *109*, 9451. (b) Wetmore, S. D.; Boyd, R. J.; Eriksson, L. A. *J. Chem. Phys.* **1997**, *106*, 7738. (c) Malkin, V. G.; Malkina, O. L.; Eriksson, L. A.; Salahub, D. R. In *Theoretical and Computational Chemistry, Vol. 2; Modern Density Functional Theory: A Tool for Chemistry*, Politzer, P.; Seminario, J. M. Eds.; Elsevier, 1995.

51. (a) St-Amant, A.; Salahub, D. R. *Chem. Phys. Lett.* **1990**, *169*, 387. (b) Salahub, D. R.; Fournier, R.; Mylynarski, P.; Papai, I.; St-Amant, A.; Ushio, J. In *Density Functional Methods in Chemistry*; Labanowski, J., Andzelm, J., Eds.; Springer-Verlag: New York, 1993. (c) St-Amant, A. Ph.D. Thesis, Université de Montréal, 1991.

Radiation Products of Glycine

3.1 Introduction

Recently, there has been a dramatic increase in interest in the functionality of protein radicals.[1] However, elucidating the reaction mechanisms of radical-containing proteins, or understanding radiation damage to a protein, requires a detailed knowledge of the chemistry and properties of amino acid radicals. Glycine, the simplest amino acid, is often used as an experimental model system[2-13] in studies of oxidation and reduction reactions of irradiated amino acids.

In 1964, after some years of controversy, Morton[12] tentatively proposed that the end oxidation and reduction products of glycine were $^+NH_3C^\bullet HCOO^-$ (R1) and $^\bullet CH_2COO^-$ (R2'), respectively. It was later shown[8b] that the species observed was $^\bullet CH_2COOH$ (R2) rather than the radical anion $^\bullet CH_2COO^-$. In 1997, Brustolon et al.[4] assigned three newly observed hyperfine coupling tensors to radical $NH_2C^\bullet H_2$. In 1998, Sanderud et al.[3] showed this to be incorrect, and proposed that the radical was $NH_2C^\bullet HCOOH$ (R3). In addition, they assigned three more observed hyperfine couplings to another conformer of $NH_2C^\bullet HCOOH$. The two experimentally observed

conformers of $NH_2C^\bullet HCOOH$ are denoted hereafter as $R3^\#$ and $R3^\bullet$. In the paper of

Sanderud et al.,[2] they correspond to Radical IV and Radical III, respectively. The H_α

isotropic hyperfine coupling constants (HFCCs) of $R3^\#$ (–30.15 MHz) and $R3^\bullet$ (–24.62

MHz) differ significantly. Based on the McConnell relation[14] and the Gordy-Bernhard[15]

method, the smaller absolute isotropic HFCC in the proposed $R3^\bullet$ was ascribed to non-

planarity of the radical centre in the glycine crystal. Furthermore, experimental data[2] was

used to suggest a twist angle of 24.2° between the OCO and CCN planes in $R3^\bullet$. This is

an example where experimental studies can only provide indirect information about the

distortion of a radical in a specific environment. The assignment of complicated ESR

spectra often requires simulations based on several assumptions. Hence, theoretical

calculations of the HFCCs of amino acid radiation products can provide valuable

assistance. The present study shows that correct identification of some radiation products

of glycine-derived radicals can only be achieved through comparison of experimental and

theoretical results. The glycine-derived radicals observed in irradiated glycine crystals at

280 K are shown in Figure 3.1.

In the gas phase chemistry of amino acids, extensive calculations of

thermochemical properties have been performed on glycine-derived radicals by Yu et

al.[16] The ESR features of the glycine radical, $H_2NC^\bullet HCOOH$, have been studied

previously at various levels of theory.[17,18] However, amino acids exist as zwitterionic

species in the crystalline state and in solution. When irradiated, radicals in a zwitterionic

form (such as R1 in Figure 3.1) can be formed. The zwitterionic structure of amino acids

and their derived radicals has been a challenge for theoretical chemistry. *Ab initio*

calculations on glycine[19] and its radical[20,21] have shown that their zwitterionic structures

do not correspond to energy minima in the gas phase. Thus, environmental effects must

be included for exploring the zwitterionic form of amino acids.
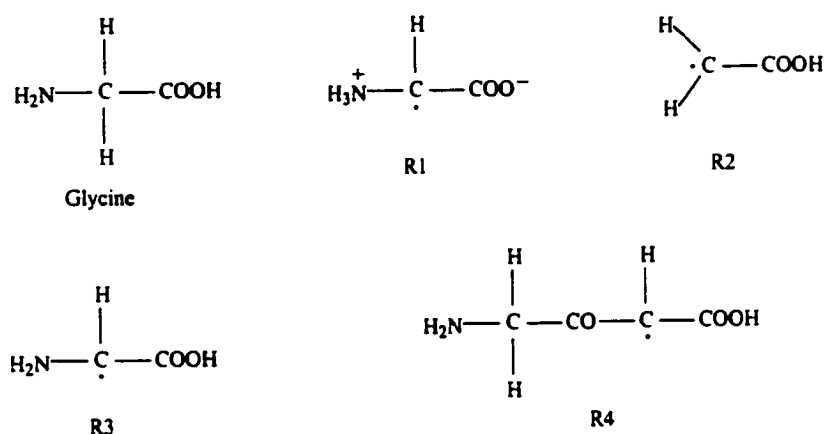
Figure 3.1 Schematic illustration of structure of glycine and related radicals generated upon X-ray irradiation of glycine crystals.

There are two strategies to account for environmental effects. One is to build a

model by adding discrete molecules around the target molecule. The second strategy is

the self-consistent reaction field, the SCRF approach (see Chapter 2). Environmental

effects on the structure of R1 have previously been considered by performing a

constrained geometry optimization[20] or by use of the conductor-like polarizable

continuum model (CPCM).[21] Previously, calculations[21] on the isolated structure of R1

have shown that the isotropic HFCCs are not significantly influenced by the crystalline

environment. In addition, it has been shown[22] that the Onsager model, using the dielectric constant of water, yields the zwitterionic structure of the alanine radical $^+NH_3C^\bullet CH_3COO^-$ and that the resulting HFCCs are in good agreement with experiments.

Density functional theory has been shown to yield very accurate hyperfine coupling constants with great computational advantages.[23,24] Extensive DFT studies on the radicals formed in irradiated DNA bases and the sugar moiety have shown the success of DFT for biological systems.[25] In particular, promising DFT results on the alanine radical system[22,26] have prompted the present systematic study[27] on glycine-derived radical species in order to obtain greater insight into the properties of irradiated amino acids.

3.2 Computational Methods

All geometry optimizations were performed with the B3LYP hybrid density functional (see Chapter 2) in conjunction with the 6-31+G(d,p) basis set using the Gaussian 98 suite of programs.

As noted previously, in solution and in the crystalline state, glycine is in its zwitterionic form, i.e., $^+NH_3CH_2COO^-$. At the above level of theory, it is not computationally feasible to explicitly include the effects of the crystalline environment. However, one is able to obtain zwitterionic structures of glycine radicals using the standard Onsager model with a dielectric constant for water of 78.39. This approach, as

noted in the Introduction, has been successfully used previously for alanine-derived radicals.[22]

All stationary points were confirmed to be local minima by harmonic vibrational frequency calculations at the same level of theory. Relative energies of all conformers of R2, R3 and R4 were obtained by performing single point calculations at the B3LYP level in conjunction with the 6-311G(2df,p) basis set using the above optimized geometries and with inclusion of the appropriate zero-point vibrational energy correction[28] i.e., B3LYP/6-311G(2df,p)//B3LYP/6-31+G(d,p) + ZPVE.

Isotropic and anisotropic hyperfine coupling constant calculations were performed using the deMon program. The PWP86 functional, a combination of Perdew and Wang's exchange functional (PW)[29] and Perdew's nonlocal correlation functional (P86),[30] in conjunction with the 6-311G(2d,p) basis set was employed. The (5,4;5,4) family of auxiliary basis sets was used to fit the charge density and the exchange correlation potential. This functional and basis set combination has been shown to give accurate hyperfine coupling constants in studies of alanine,[22] histidine[31] and model π-radicals.[32]

The assessments of methods for accurate calculation of hyperfine coupling constants have been discussed in Chapter 2. However, it should be noted that satisfactory anisotropic HFCCs can definitely be obtained at the present level of theory provided the structure is qualitatively correct, and that comparison of anisotropic hyperfine tensors can be used as a reliable guide to identify radicals when less satisfactory agreement is obtained for the isotropic coupling constants.

3.3 Results and Discussion

The optimized geometries of R1, R2, R3 and R4 are shown schematically in Figure 3.2, while those of experimentally proposed radicals R4' ($^+$NH$_3$CH$_2$COC$^\bullet$HCOO$^-$) and R2' ($^\bullet$CH$_2$COO$^-$) are shown schematically in Figure 3.3.
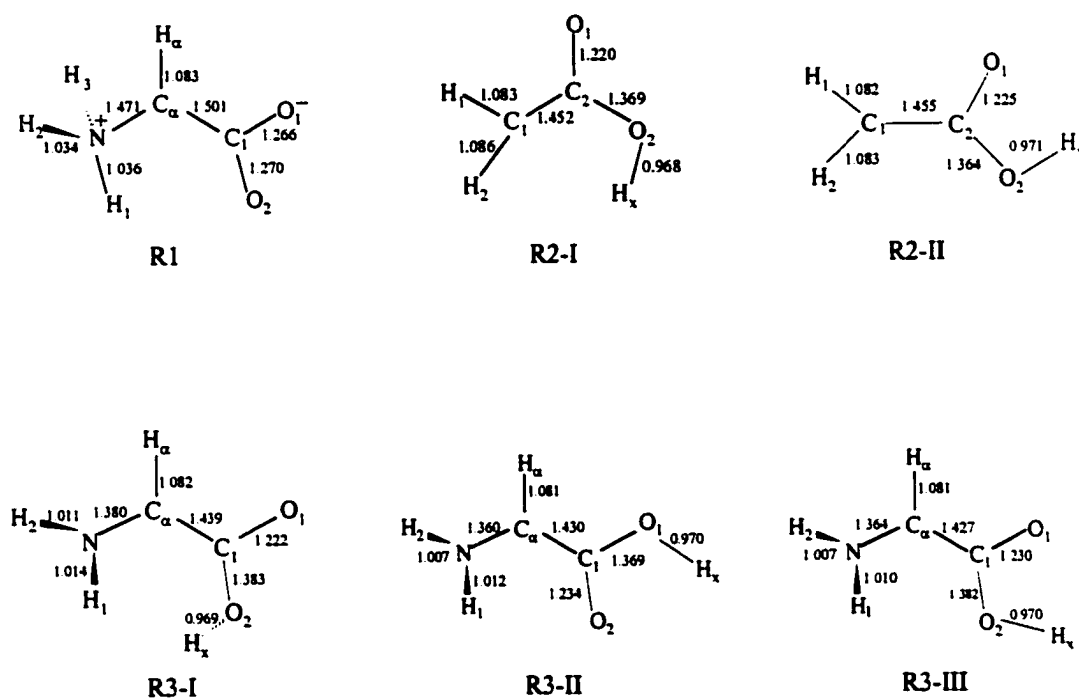
Figure 3.2 Optimized structures of R1, R2, R3, and R4 (continued over page).
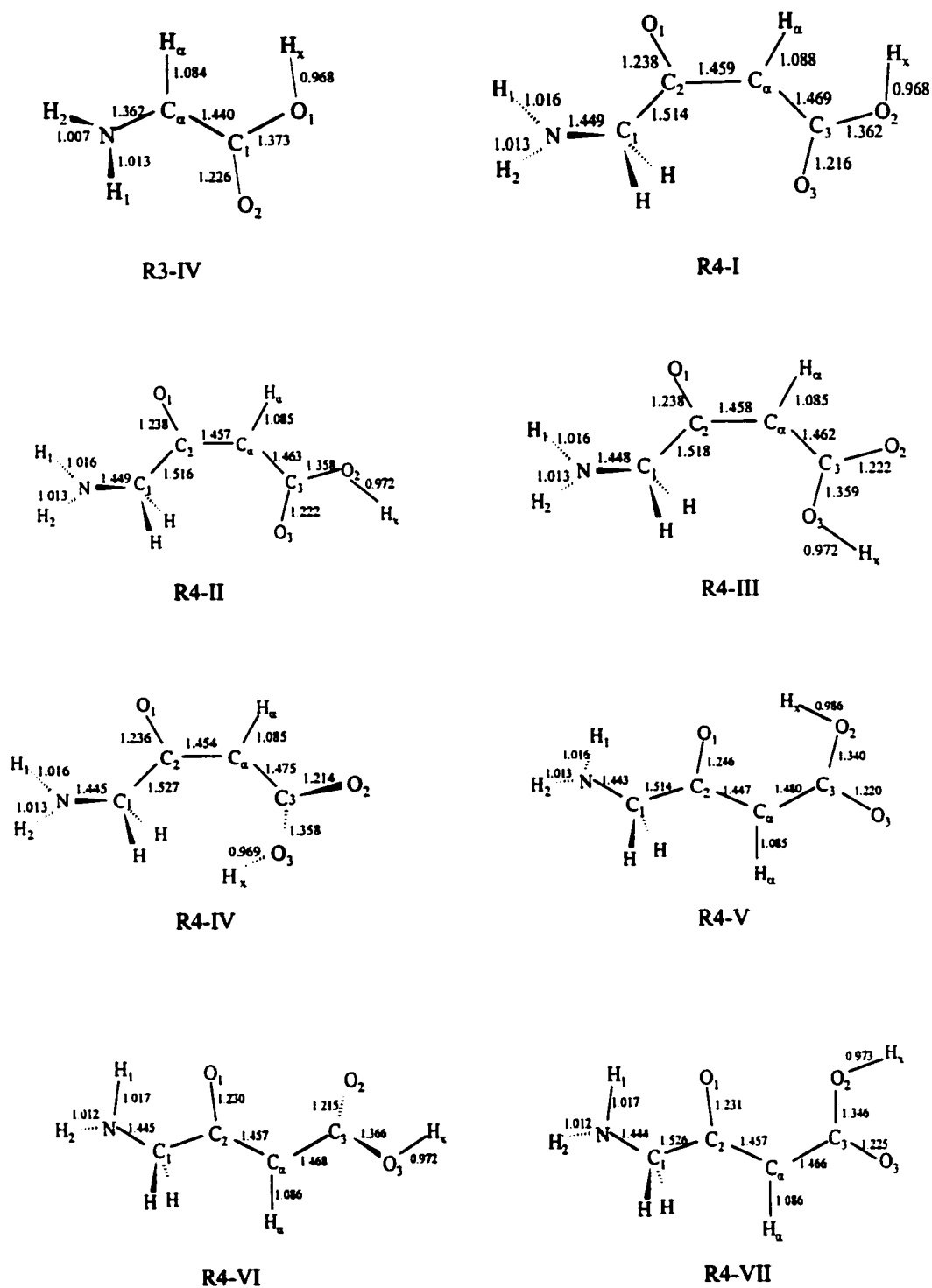
Figure 3.2 Optimized structures of R1, R2, R3, and R4.
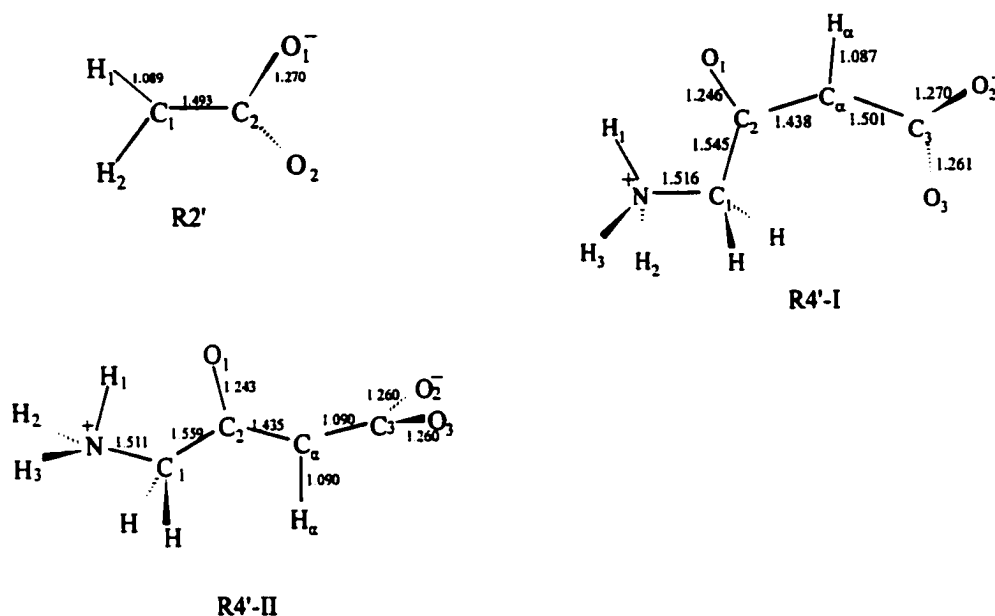
Figure 3.3 Optimized structures of R2' and R4'.

3.3.1 Geometry and Hyperfine Couplings of $^{+}NH_3C^{\bullet}HCOO^{-}$

The optimized zwitterionic structure of R1 (Figure 3.2) was obtained using the Onsager model with an estimated radius of 3.24 Å. It possesses C_s symmetry having a planar radical centre. Thus, R1 is a typical π-radical. The computed full hyperfine tensors of R1, as well as the experimental values and other previously calculated values, are listed in Table 3.1. The H_α isotropic HFCC is in good agreement with the experimental value. Similarly, the anisotropic components agree well with the experimental values, although the sign of T_{yy} differs from T_{yy}^{exp} due to its small value. In addition, comparison of the calculated (-95.0, -60.4, -21.5) and the experimental (-97.5, -61.9, -31.8) principal components shows that only the A_{zz} component is difficult to reproduce.

Table 3.1: PWP86/6-311G(2d,p) calculated and experimental HFCCs (MHz) of R1.

tensor	A_{iso}	T_{xx}	T_{yy}	T_{zz}	A_{iso}^{exp}	T_{xx}^{exp}	T_{yy}^{exp}	T_{zz}^{exp}	A_{iso}^{c}
H_α	-58.96	-36.06	-1.46	37.51	-63.72[a]	-33.80[a]	1.85[a]	31.94[a]	-60.3
H_1	2.33	-5.39	-4.66	10.05	3.3[b]	-7.3[b]	-1.8[b]	9.2[b]	
H_2	77.06	-5.47	-4.52	9.99	62.91[a]	-6.60[a]	-4.07[a]	10.66[a]	
H_3	77.06	-5.47	-4.52	9.99	83.05[a]	-5.86[a]	-4.80[a]	10.65[a]	
H_{ave}	52.15	-5.44	-4.57	10.01	49.07[a]	-2.93[a]	-2.05[a]	4.97[a]	52.1
C_α	98.73	-76.29	-74.57	150.87	126.7[c]	-90.0[c]	-36.7[c]	126.8[c]	95.3
N	-6.96	-0.43	0.20	0.22	-8.72[d]	-0.98[d]	-0.76[d]	1.71[d]	-9.0

[a]Ref 2. [b]Ref 11. [c]Ref 12. [d]Ref 10. [e]Ref 21 (B3LYP/EPR-2 calculated values).

The anisotropic components of the hyperfine tensors of the three amino hydrogens (H_1, H_2 and H_3) are in good agreement with the experimental values. The isotropic HFCCs of H_1, H_2 and H_3 are of similar magnitude as experimental values with the largest differences of 14.15 and 5.99 MHz being observed for H_2 and H_3, respectively. The isotropic HFCC and anisotropic components of the nitrogen are in good agreement with the experimental values. It can be seen that the calculated C_α HFCC at the PWP86/6-311(2d,p) level is in fair agreement with the experimental value and slightly better than a previous B3LYP/EPR-2 calculated value.[21] The B3LYP/EPR-2 study[21] has shown that the deviation of C_α HFCC based on the optimized zwitterionic structure can be significantly corrected by including the effect of vibrational averaging. The HFCCs of H_α and N, however, are not sensitive to vibrational averaging. Experimentally the sign of the N hyperfine coupling has not been determined, however, it has been suggested to be negative.[8a,10,13b] This is supported by previous theoretical studies[20,21] and by the present results. In addition, an investigation[26] for the analogous alanine radical, $^+NH_3C^\bullet CH_3COO^-$, obtained a negative sign for the N HFCC.

The average (52.15 MHz) of the isotropic HFCCs of the three amino protons is in good agreement with the experimentally observed value of 49.07 MHz at 280 K, suggesting that the amino group rotates freely at 280 K. Furthermore, it also suggests that at 100 K the orientation of the amino group in glycine crystals is constrained, giving rise to the three specific HFCC tensors of amino protons. Therefore, a detailed investigation was undertaken on the effects on the isotropic HFCCs of H_1, H_2, H_3, H_α, C_α and N of rotating the amino group about the N—C_α bond of R1. The variation of the isotropic HFCCs as a function of the rotational angle is shown in Figure 3.4. The rotation of the amino group was carried out by incrementally increasing the dihedral angle $\angle H_1NC_\alpha C_1$ by 30°, starting from $\angle H_1NC_\alpha C_1 = 0°$. From Figure 3.4 it can be seen that the isotropic HFCCs of H_1, H_2 and H_3 change dramatically, similar to that observed in the zwitterionic radical of alanine.[22] However, the isotropic couplings of H_α, C_α and N are almost constant. It is noted that the difference in amplitude of the variation of the HFCC of H_1 and those of H_2 and H_3 is due to the fact that the geometrical parameters of the amino group have been constrained during rotation.

When the amino group is rotated by approximately 5°, the isotropic HFCCs of H_2 and H_3 are in good agreement with the experimental values 62.91 and 83.05 MHz at 100 K, while the isotropic HFCC of H_1 is still less than 5 MHz. These results support the fact[2] that only the hyperfine splittings of two of the three constrained amino protons are easily observed; while the third remains too small to be distinguished from the many lines observed in the ENDOR spectra. Thus, from the HFCC calculations for the isolated R1 it

can be concluded that the crystalline environment has little direct effect on the ESR

spectra of R1, similar to the conclusion of a previous study.[21]
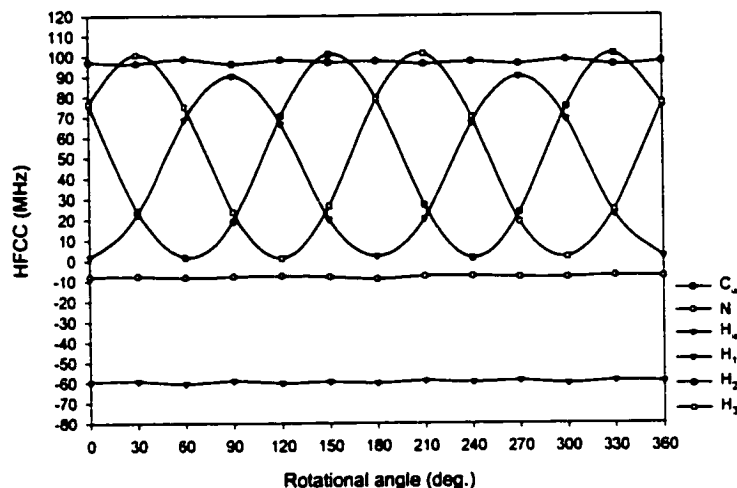
Figure 3.4 Variation of H_α, H_1, H_2, H_3, C_α, and N isotropic HFCCs with rotational angle of the amino group of R1.

3.3.2 Geometry and Hyperfine Couplings of $^\bullet CH_2COOH$

In 1964, Morton[12] concluded that the second radical observed in irradiated glycine

crystals was the radical anion $^\bullet CH_2COO^-$ (R2' in Figure 3.3) with only one H_α hyperfine

coupling due to two equivalent hydrogens. However, Teslenko et al.[8b] reported that two

forms of $^\bullet CH_2COOH$ (R2 in Figure 3.2) were observed; one at 77 K, the other at 140 K.

Three inequivalent hyperfine couplings were observed for the conformer at 77 K, while

two were observed for the conformer at 140 K. Recently, similar hyperfine structures

were observed[2] at 100 K with the ambiguous conclusion that the radical may be either

$^\bullet CH_2COO^-$ or $^\bullet CH_2COOH$. To clarify this ambiguity, calculations were performed on

both species. The optimized structures of R2 and R2' are shown in Figures 3.2 and 3.3,

respectively. Two conformers of $^\bullet CH_2COOH$, R2-I and R2-II (Figure 3.2), were found.

R2-I is almost planar, while R2-II is planar. Due to the existence of intramolecular

hydrogen bonding R2-II lies 23.4 kJ mol^{-1} lower in energy than R2-I (see Table 3.2).

Interestingly, it was found that R2' is not planar, both oxygen atoms lie out of the $H_1C_1H_2$

plane. However, R2' was found to possess C_2 symmetry with a planar radical centre.

Table 3.2: PWP86/6-311G(2d,p) calculated and experimental[a] HFCCs (MHz) of R2-I, R2-II and R2', and calculated[b] relative energies (kJ mol^{-1}) of R2-I and R2-II.

tensor	HFCC	R2-I	R2-II	R2'	exptl 140 K	exptl 77 K
H_1	A_{iso}	-57.23	-57.71	-47.2	-58.9	-59.5
	T_{xx}	-33.30	-33.79	-32.9	-33.1	-34.0
	T_{yy}	-2.06	-2.07	-0.4	0.4	0.4
	T_{zz}	35.36	35.86	33.3	32.7	33.6
H_2	A_{iso}	-55.76	-57.24	-46.6	-55.8	-58.6
	T_{xx}	-34.66	-34.59	-33.0	-33.9	-33.9
	T_{yy}	-1.28	-1.68	-0.4	1.2	1.7
	T_{zz}	35.94	36.28	33.3	32.6	32.2
H_x	A_{iso}	-1.69	-4.09			0.48
	T_{xx}	-3.97	-2.78			-6.48
	T_{yy}	-2.08	-2.41			-3.75
	T_{zz}	6.04	5.19			10.27
ΔE		23.4	0.0			

[a] Ref 8b. [b] B3LYP/6-311G(2df,p)//B3LYP/6-31+G(d,p) + ZPVE.

The calculated and experimental hydrogen HFCC tensors of R2', R2-I and R2-II

are listed in Table 3.2. For R2, the isotropic HFCCs and anisotropic components of H_1

and H_2 in R2-I are closest to the experimental values[8b] of the conformer observed at 140

K, while the isotropic HFCCs and anisotropic components of H_1 and H_2 in R2-II are in

closest agreement with the experimental values[8b] of the conformer observed at 77 K

(Table 3.2). The isotropic coupling and anisotropic components of H_x in both R2-I and R2-II are in reasonable agreement with the experimental values for the conformer observed at 77 K. In the case of R2', the anisotropic components of H_1 and H_2 of R2' are in good agreement with the experimental values of both observed conformations. However, the isotropic HFCCs of H_1 and H_2 of R2' differ significantly from the experimental HFCCs of both conformers at 77 K and 140 K. Thus, it can be concluded that neither of the conformations observed at 77 K and 140 K is R2', but instead are either R2-I or R2-II. However, as the calculated H_1 and H_2 hyperfine tensors of R2-I and R2-II are too close to be definitively assigned, more elaborate theoretical studies incorporating specific crystal and temperature effects, beyond the scope of the present study, will be required in order to make more definitive assignments.

3.3.3 Geometry and Hyperfine Couplings of NH₂C•HCOOH

The four optimized conformers of $NH_2C^\bullet HCOOH$ (denoted as R3-I, R3-II, R3-III and R3-IV) are shown in Figure 3.2. The backbones of R3-II, R3-III and R3-IV are almost planar with all hydrogen atoms close to the $C_1C_\alpha N$ plane. Due to the significant repulsion between H_x and H_1, R3-I is more distorted with the two oxygen atoms being out of the $C_1C_\alpha N$ plane by more than 7.7°, while H_1 is distorted out of the $C_1C_\alpha N$ plane by 36.3°. Accordingly, the radical centres in R3-II, R3-III and R3-IV are less pyramidal than in R3-I. The relative energies in Table 3.3 show that R3-II and R3-III, with intramolecular hydrogen bonding, are more stable than R3-I and R3-IV.

The computed HFCC tensors in R3-I, R3-II, R3-III and R3-IV and the experimental HFCC tensors of R3$^\#$ and R3* are listed in Table 3.3. It is noted that the calculated isotropic HFCCs (-17.01 and -14.27 MHz) of the amino protons of R3-II differ significantly from previously calculated values (10.12 and -4.82 MHz).[18] This difference is most probably due to differences in the DFT optimized geometries used for the HFCC calculations. The optimized geometry obtained as part of this study is in closer agreement with higher-level *ab initio* calculations,[16] suggesting that the presently calculated HFCCs should be more reliable.

Table 3.3: PWP86/6-311G(2d,p) calculated HFCCs (MHz) of R3-I, R3-II, R3-III, R3-IV and the experimental[a] values of R3$^\#$ and R3* and calculated[b] relative energies (kJ mol^{-1}) of R3-I, R3-II, R3-III and R3-IV

tensor	HFCC	R3-I	R3-II	R3-III	R3-IV	exptl (R3$^\#$)	(R3*)
H$_\alpha$	A$_{iso}$	-40.41	-36.10	-38.03	-37.61	-30.15	-24.62
	T$_{xx}$	-24.95	-22.26	-22.36	-23.47	-17.24	-16.22
	T$_{yy}$	-2.04	-2.14	-2.06	-1.38	-0.19	-1.54
	T$_{zz}$	26.99	24.40	24.42	24.85	17.48	17.77
H$_1$	A$_{iso}$	25.04	-17.01	-16.39	-16.02	-18.05	-16.87
	T$_{xx}$	-12.60	-16.08	-15.81	-14.96	-16.00	-17.25
	T$_{yy}$	-5.52	-6.45	-5.04	-5.74	-4.18	-4.37
	T$_{zz}$	18.12	22.53	20.85	20.70	20.28	21.62
H$_2$	A$_{iso}$	-12.78	-14.27	-14.78	-10.70	-16.79	-15.46
	T$_{xx}$	-13.99	-19.26	-17.60	-18.02	-15.39	-16.42
	T$_{yy}$	-4.83	-5.42	-4.54	-4.65	-2.94	-3.99
	T$_{zz}$	18.82	24.67	22.15	22.67	18.34	20.40
ΔE		43.0	0.0	5.8	23.4		

[a] Ref 2. [b] B3LYP/6-311G(2df,p)//B3LYP/6-31+G(d,p) + ZPVE.

From careful comparison of the calculated HFCCs for the four conformers of R3, they can be divided into two groups, with R3-I in one group and the rest in a second group. The isotropic HFCCs of H$_\alpha$ in R3-II, R3-III and R3-IV are all in similar

agreement with the experimental value of R3# differing by 6-8 MHz, however, they differ

significantly from the experimental value of R3* by at least 12 MHz. The anisotropic

components of the H_α HFCC tensor for the above conformers are in similar agreement

with the experimental values of both R3# and R3*. Except for the isotropic HFCC of H_2

in R3-IV, the isotropic HFCCs and anisotropic components of the two amino protons of

R3-II, R3-III and R3-IV are in good agreement with the corresponding experimental

values of both R3# and R3*, which are themselves very similar. Larger deviations were

found between the calculated isotropic and anisotropic HFCCs of H_α and the

experimental values of R3# or R3* in R3-I than in R3-II to R3-IV. It was found that the

computed amino-proton isotropic H_1 HFCCs (25.03 MHz) in R3-I and the experimental

values R3# and R3* (-18.05 and -16.87 MHz, respectively) are of the same magnitude,

however, their signs are opposite. In addition, the anisotropic components of H_1 in R3-I

are in poorer agreement with the experimental values than those of H_1 in the second

group. Thus, R3-I is neither R3# nor R3*. Although the above calculations using gas-

phase optimized structures of R3 could not distinguish between R3# and R3*, R3# is

concluded to be one conformer or a mixture of R3-II, R3-III and R3-IV. This is

supported by the fact that R3-I is at least 20 kJ mol^{-1} higher in energy than the other three

conformers of R3.

The calculated H_α isotropic HFCCs of R3-II, R3-III and R3-IV are in closer

agreement with the experimental isotropic HFCC (33.0 MHz) of R3 in solution[9] than in

the crystal.[2] Hence, the deviation of the calculated H_α isotropic HFCCs of R3-II to R3-

IV from the experimental values of R3# is likely due to crystal-packing effects, which are not taken into account by the above calculation.

An experimentally suggested[2] twist angle of 24.2° between the $NC_\alpha C_1$ and $O_1 C_1 O_2$ planes in R3* implies that the two amino protons and the two carboxylic oxygens are constrained by intermolecular hydrogen bonding. The effect of the two-plane twist on the H_α, H_1 and H_2 HFCCs of R3# was investigated by re-optimizing only H_α related geometrical parameters, i.e., H_α—C_α, $\angle H_\alpha C_\alpha C_1$, and $\angle H_\alpha C_\alpha C_1 N$ in R3-II, R3-III and R3-IV. The twisting of the $NC_\alpha C_1$ plane with respect to the $O_1 C_1 O_2$ plane was carried out by incrementally increasing the absolute value of $\angle O_2 C_1 C_\alpha N$ by 10° from 0°. The variation of the isotropic HFCCs of H_α, H_1 and H_2 with respect to the twist angle is shown in Figure 3.5.

It can be seen that the three plots exhibit the same pattern. The absolute isotropic HFCC of H_α decreases as the twist angle increases in R3-II, R3-III and R3-IV. The isotropic HFCC of one amino proton (H_1) increases as the isotropic HFCC of the other amino proton (H_2) decreases in R3-II, R3-III and R3-IV. As the isotropic HFCCs of H_1 and H_2 become equal (see Figure 3.5), the average ($H_{1,2}^{ave}$) of the isotropic HFCCs of H_1 and H_2 decreases slightly. However, the $H_{1,2}^{ave}$ values are all very close to the average of the experimental H_1 and H_2 isotropic couplings in R3* (16.16 MHz). It should be noted that by varying the twist angle, one is able to produce changes in the calculated H_α and $H_{1,2}^{ave}$ HFCCs similar to the experimentally observed differences between R3# and R3* (see Table 3.3). Thus, although the calculations are unable to determine the conformation

of R3*, it does support the experimental conclusion that R3* is only a twisted

configuration of R3# fixed by intermolecular hydrogen bonding in glycine crystals.
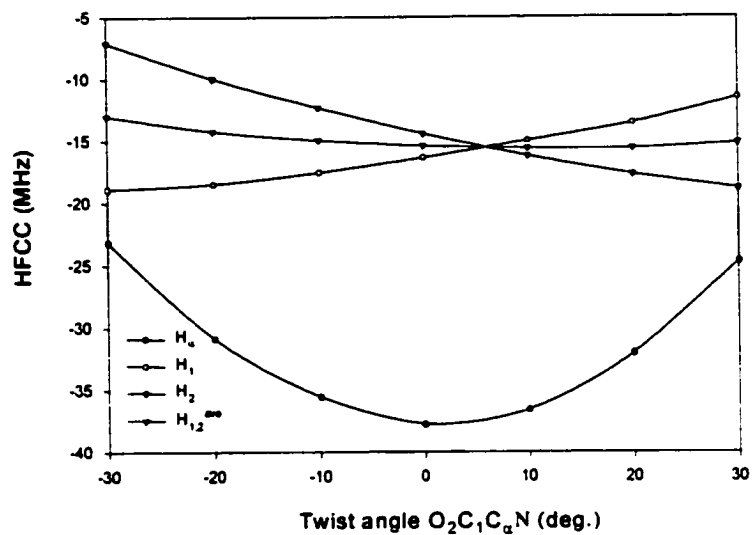
a
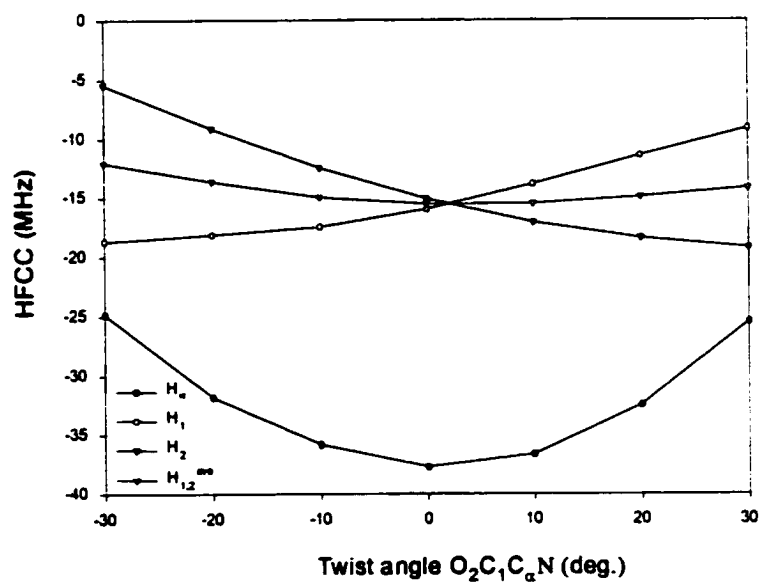
b

Figure 3.5 Variation of H_α, H_1, H_2, and $H_{1,2}{}^{ave}$ isotropic HFCCs in (a) R3-II, (b) R3-III and (c) R3-IV with the twist angle $\angle O_2C_1C_\alpha N$ (continued over page).
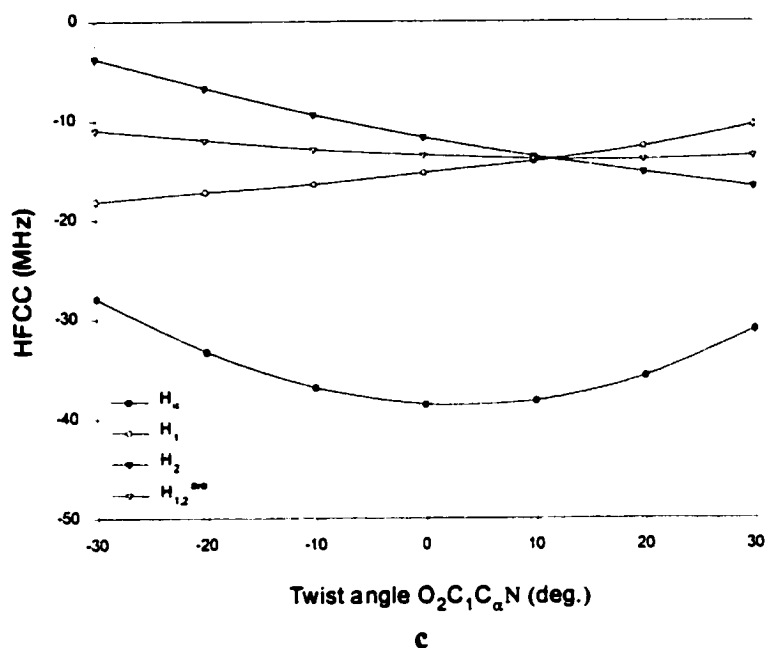
c

Figure 3.5 Variation of H_α, H_1, H_2, and $H_{1,2}^{ave}$ isotropic HFCCs in (a) R3-II, (b) R3-III and (c) R3-IV with the twist angle $\angle O_2C_1C_\alpha N$.

3.3.4 Protonation Effects on the Hyperfine Couplings in NH₂C•HCOOH

To complete the theoretical studies of R3$^\#$ and R3*, the corresponding protonated radical cation $NH_2C^\bullet HC(OH)_2{}^+$ (R3^P) was investigated. Optimized structures for conformers of R3^P are shown in Figure 3.6. In R3^P-I and R3^P-III, the protonated carboxylic group is distorted slightly due to the repulsion between H_1 and H_{x2}, however, the radical centres are almost planar. R3^P-II is planar. In R3^P-IV, while the two oxygen atoms are distorted out of the $C_1C_\alpha N$ plane slightly by 2.7°, the rest including the radical centre C_α remains planar. Comparison of the geometries of R3^P with R3 suggests that protonation of R3 tends to make both the C_α and N centres more planar. However, the

repulsion between H_1 and H_{x2} for a specific orientation can distort the planarity slightly. From the relative energies listed in Table 3.4 it can be seen that $R3^P$-II is the most stable conformer.

The computed hyperfine coupling tensors in $R3^P$-I, $R3^P$-II, $R3^P$-III and $R3^P$-IV are shown in Table 3.4. The isotropic HFCC and anisotropic components of H_α in each conformer are in agreement with the corresponding experimental values of $R3^*$. However, the isotropic HFCCs of the two amino protons in $R3^P$-I, $R3^P$-II, $R3^P$-III and $R3^P$-IV are slightly larger than the experimental isotropic HFCCs. Interestingly, the anisotropic components of the two amino protons in each conformer are in good agreement with the experimental values of $R3^*$. The calculations suggest that to exclude the possibility that $R3^P$ is $R3^*$, experimental studies of the carboxylic proton are required.
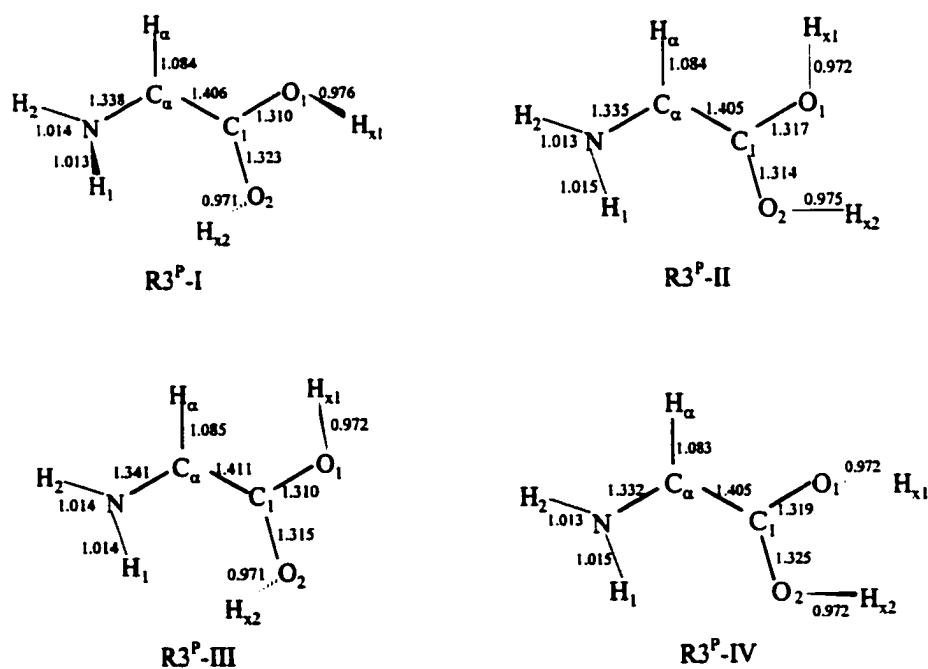
Figure 3.6 Optimized structures of $R3^P$.

Table 3.4: PWP86/6-311G(2d,p) calculated HFCCs (MHz) of R3^P and experimental[a] values of R3* and calculated[b] relative energies (kJ mol^{-1}) of R3^P-I, R3^P-II, R3^P-III and R3^P-IV.

tensor	HFCC	R3^P-I	R3^P-II	R3^P-III	R3^P-IV	exptl R3*
H$_\alpha$	A$_{iso}$	-22.88	-22.89	-23.37	-21.74	-24.62
	T$_{xx}$	-13.55	-13.12	-14.70	-12.32	-16.22
	T$_{yy}$	-4.19	-3.73	-3.84	-4.04	-1.54
	T$_{zz}$	17.73	16.85	18.54	16.36	17.77
H$_1$	A$_{iso}$	-19.68	-24.09	-20.05	-22.87	-15.46
	T$_{xx}$	-17.38	-17.81	-17.50	-16.81	-16.42
	T$_{yy}$	-5.42	-5.91	-5.40	-5.73	-3.99
	T$_{zz}$	22.80	23.71	22.90	22.54	20.40
H$_2$	A$_{iso}$	-23.32	-25.04	-24.58	-24.17	-16.87
	T$_{xx}$	-19.27	-20.93	-19.36	-20.00	-17.25
	T$_{yy}$	-4.850	-5.02	-4.83	-4.74	-4.37
	T$_{zz}$	24.12	25.95	24.19	24.74	21.62
ΔE		22.1	0.0	38.2	10.1	

[a] Ref 2. [b] B3LYP/6-311G(2df,p)//B3LYP/6-31+G(d,p) + ZPVE.

3.3.5 Enhanced Captodative Effects from Protonation

It was postulated that the complementary electron withdrawing (capto) and electron-donating (dative) effect in R3 will enhance its stablization by delocalization of spin density and charge.[33] It can be seen that R3^P also has an electron donating group – NH$_2$ and an electron withdrawing group –C(OH)$_2$$^+$. In order to identify how the spin density delocalizes in captodative type radicals, the spin densities on the C, N and O atoms of R3 and R3^P were compared (see Table 3.5). It can be seen that more than 50% of the total spin is localized on C$_\alpha$ in R3, while the rest is mainly localized on the N and carbonyl O. It can be concluded that this type of spin distribution is due mainly to the effect of the spin polarization of the unpaired electron at C$_\alpha$ on the lone pair electrons of the N and π electrons of the CO double bond of the carboxylic group. In R3^P, more than

80% of the spin density is almost equally shared between the N, C_α and C_1 atoms, while the rest is shared by the two O atoms. Thus, the spin distribution in $R3^P$ is significantly different from that seen in R3. The spin density $\rho(C_\alpha) > \rho(C_1) > \rho(O_i)$, (i = 1, 2), in $R3^P$ can be explained by the spin induction along the chemical bonds by the positive charge of $-C(OH)_2^+$. Furthermore, the strong electron withdrawing capability of $-C(OH)_2^+$ in $R3^P$ significantly enhances the spin polarization of the lone pair electrons of the N atom. Hence, approximately 30% of the spin density resides on the N. Thus, spin induction and spin polarization together explain the spin distribution $\rho(C_\alpha) \sim \rho(N) > \rho(C_\alpha) > \rho(C_1) > \rho(O_1) \sim \rho(O_2)$ in $R3^P$.

Table 3.5: PWP86/6-311G(2d,p) calculated spin density on C, N and O atoms of R3 and $R3^P$.

system	C_α	N	C_1	O_1	O_2	$O_1 + O_2$
R3-I	0.614	0.210	0.018	0.187	0.013	0.200
R3-II	0.507	0.291	0.079	0.033	0.146	0.179
R3-III	0.540	0.267	0.05	0.18	0.021	0.201
R3-IV	0.556	0.277	0.048	0.036	0.141	0.177
$R3^P$-I	0.313	0.315	0.239	0.115	0.067	0.182
$R3^P$-II	0.291	0.345	0.243	0.094	0.081	0.175
$R3^P$-III	0.351	0.322	0.213	0.107	0.063	0.170
$R3^P$-IV	0.268	0.329	0.272	0.103	0.077	0.180

3.3.6 Geometry and Hyperfine Couplings of $NH_2CH_2COC^\bullet HCOOH$

The detection of R4 is a new finding[2] in the radiation chemistry of glycine crystals at room temperature. Experiments[2] confidently showed that there is only one H_α coupling tensor in R4 without any other α- and β-proton couplings. This fact prompted Sanderud et al.[2] to propose a zwitterionic structure (R4') for the dimeric type radical and

to propose a mechanism for the formation of R4' from the reaction of zwitterionic glycine with R2'. However, an assignment of the observed couplings to the correct radiation products is essential for further mechanistic studies. The optimized structures of two possible conformers of R4', obtained using the Onsager model with an estimated radius 4.16 Å, are shown schematically in Figure 3.3.

The carbons and nitrogen in R4'-I form an almost planar skeleton with a nearly planar radical centre. However, O_2 and O_3 lie out of the mean molecular plane by approximately $25°$. In R4'-II, the carbons, N and O_1 are coplanar, while the $O_2C_3O_3$ plane is almost perpendicular to the plane of the molecular skeleton.

The calculated hyperfine coupling tensors of H_α in R4'-I and R4'-II as well as the experimental values are listed in Table 3.6. It can be seen that both the isotropic HFCC and anisotropic components of H_α in R4'-I and R4'-II differ significantly from the corresponding experimental values. Thus, it is unlikely that R4' is the radical experimentally observed. However, it is quite possible that R4' is in fact not in its zwitterionic form. Hence, the neutral radical $NH_2CH_2COC^{\bullet}HCOOH$ (R4) was also investigated. Seven conformers of R4 were located, their optimized structures are shown schematically in Figure 3.2.

There are significant skeletal differences between the structures of R4-I to R4-IV and those of R4-V to R4-VII. The four carbon atoms in R4-I to R4-IV form *cis*-structures while the four carbon atoms in R4-V to R4-VII form *trans*-structures. The main difference between R4-I, R4-II, R4-III and R4-IV is the bonding position and

orientation of H_x, similarly for R4-V, R4-VI and R4-VII. The radical centre in R4-I, R4-II, R4-III, R4-V, R4-VI and R4-VII is almost planar, while the radical centre in R4-IV ($\angle H_\alpha C_\alpha C_3 C_2 = -172.6°$) is distorted by approximately 8° due to repulsion between H_x and the hydrogen on C_1. In addition, O_2 and O_3 in R4-IV lie out of the $C_3 C_\alpha H_\alpha$ plane by 29.4°.

Table 3.6: PWP86/6-311G(2d,p) calculated HFCCs of R4' and R4 with experimental[a] values and calculated[b] relative energies (kJ mol⁻¹).

system	A_{iso}	T_{xx}	T_{yy}	T_{zz}	ΔE
R4'-I	-12.15	-12.89	-4.38	17.27	
R4'-II	-20.34	-12.79	-1.99	14.77	
R4-I	-41.39	-24.82	-2.25	27.08	29.6
R4-II	-42.03	-24.65	-2.47	27.13	7.0
R4-III	-42.31	-23.76	-2.84	26.60	13.4
R4-IV	-41.37	-23.91	-3.26	27.17	42.1
R4-V	-41.72	-24.70	-2.47	27.17	0.0
R4-VI	-42.92	-26.46	-1.86	28.32	21.3
R4-VII	-42.27	-25.28	-2.32	27.60	18.8
exptl	-47.99	-25.03	1.29	23.73	

[a] Ref 2. [b] B3LYP/6-311G(2df,p)//B3LYP/6-31+G(d,p) + ZPVE.

The calculated HFCC tensors of H_α in R4-I to R4-VII are listed in Table 3.6. It can be seen that both the isotropic HFCC and anisotropic components of the H_α tensor in R4-I to R4-VII are in close agreement with the corresponding experimental values. Thus, it can be concluded that the experimentally observed radical must be R4 and not R4'. Correspondingly, R4 should be formed from the reaction of the zwitterionic form of glycine with R2, rather than with R2'. Thus, a deprotonation of the amino group in the zwitterionic form of glycine must be involved. However, in order to determine the conformation of R4 and the mechanism by which it is formed, more experimental and theoretical investigations of the radical are required.

3.4 Conclusions

The geometries and hyperfine couplings of the four observed radicals generated from irradiated glycine crystals have been computed using density functional theory. The calculated HFCCs have been compared with experimental values obtained at 295, 100 and 77 K.

A zwitterionic structure of R1 with C_s symmetry was predicted using the Onsager model. The H_α couplings and the average HFCC of the three amino protons are in good agreement with the experimental values supporting the observation that the amino group in glycine rotates freely at room temperature. A detailed study of the effect of rotating the amino group on the proton HFCCs showed that at 100 K the amino group of R1 is constrained by intermolecular hydrogen bonding to be approximately 5° away from the optimized structure. The small value of the H_1 isotropic HFCC when the rotational angle is 5° supports the fact that the HFCC of one of the three amino protons is too small to be distinguished by the ENDOR technique at 100 K. In addition, the rotation of the amino group was found to have little effect on the HFCCs of H_α, C_α and N in R1.

Two conformers of $^\bullet CH_2COOH$ (R2-I and R2-II) were found which are able to account for the two forms of R2 observed experimentally, one at 77 K and the other at 140 K. The hyperfine coupling constants of the alternatively suggested radical R2' ($^\bullet CH_2COO^-$) differ significantly from those observed experimentally. However, the present calculations are unable to unambiguously assign R2-I or R2-II to either experimentally observed conformer.

The HFCCs of three of the four possible conformations of R3 account for the experimental values of R3$^{\#}$. However, the deviation of the calculated isotropic HFCC of H$_\alpha$ from experiments suggests that the crystal-packing in glycine has a significant effect on the H$_\alpha$ hyperfine coupling constant of R3$^{\#}$. HFCC calculations on the re-optimized structures of R3, with appropriate geometrical constraints support the experimental postulate that the major difference between the two conformations of R3 is the twist between the $O_1C_1O_2$ and $C_1C_\alpha N$ planes.

HFCC calculations on the experimentally proposed zwitterionic structure of R4' obtained with the Onsager model differ significantly from the experimental values, showing that R4' could not be the radical observed. However, the seven conformers of R4 all give HFCCs in good agreement with the experimental values. Hence, it is more likely that the radical observed experimentally is R4 (i.e., non-zwitterionic form). Thus, when it is formed from the reaction of the zwitterionic form of glycine with R2, a deprotonation of the amino group in the zwitterionic form of glycine must be involved.

With respect to the theoretical methods employed, it can be seen that density-functional theory is successful in predicting the magnetic properties of amino acid radicals. Furthermore, the Onsager model is found to work as equally well for the glycine radical in its zwitterionic form as originally found for the alanine radical system (see Chapter 4), resulting in structures capable of reproducing the experimental hyperfine coupling constants.

References

1. (a) Stubbe, J.; Donk, W. A. v. *Chem. Rev.* **1998**, *98*, 705. (b) Stubbe, J. *Annu. Rev. Biochem.* **1989**, *58*, 257. (c) Stubbe, J. *J. Biochemistry* **1988**, *27*, 3893.

2. Sanderud, A.; Sagstuen, E. *J. Phys. Chem.* B **1998**, *102*, 9353.

3. Bonifacic, M.; Stefanic, I.; Hug, G. L.; Armstrong, D. A.; Asmus, K. *J. Am. Chem. Soc.* **1998**, *120*, 9930.

4. Brustolon, M.; Chis, V.; Maniero, A. L.; Brunet L. *J. Phys. Chem.* A **1997**, *101*, 9763.

5. Syutkin, V. M.; Tolkachev, V. A. *Radiat. Phys. Chem.* **1982**, *20*, 281.

6. Box, H. C. *Radiation effects: ESR and ENDOR Analysis*, Academic Press: New York, 1977.

7. (a) Muto, H.; Iwasaki, M. *J. Chem. Phys.* **1977**, *66*, 1943. (b) Nunome, K.; Muto, H.; Toriyama, K.; Iwassaki, M. *J. Chem. Phys.* **1976**, *65*, 3805. (c) Iwassaki, M.; Muto, H. *J. Chem. Phys.* **1974**, *61*, 5315.

8. (a) Deigen, M. F.; Krivenko, V. G.; Pulatova, M. K.; Ruban, M. A.; Teslenko, V. V.; Kayushin, L. P. *Biofisika* **1973**, *18*, 235. (b) Teslenko, V. V.; Gromovoi, Yu. S.; Krivenko V. G. *Mol. Phys.* **1975**, *30*, 425.

9. Neta, P; Fessenden, R. W. *J. Phys. Chem.* **1971**, *75*, 738.

10. Hedberg, A.; Ehrenberg A. *J. Chem. Phys.* **1968**, *48*, 4822.

11. Collins, M. A.; Whiffen, D. H. *Mol. Phys.* **1966**, *10*, 317.

12. Morton, J. R. *J. Am. Chem. Soc.* **1964**, *86*, 2325.

13. (a) Ghosh, D. K.; Whiffen, D. H. *J. Chem. Soc.* **1960**, 1869. (b) Ghosh, D. K.; Whiffen, D, H. *Mol. Phys.* **1959**, *2*, 285.

14. McConnell, H. M. *J. Chem. Phys.* **1956**, *24*, 764.

15. Gordy, W. *Theory and Applications of Electron Spin Resonance*, John Wiley & Sons: New York, 1980.

16. Yu, D.; Rauk, A.; Armstrong, D. A. *J. Am. Chem. Soc.* **1995**, *117*, 1789.

17. Barone, V.; Adamo, C.; Grand, A.; Jolibois, F. Brunel, Y.; Subra, R. *J. Am. Chem. Soc.* **1995**, *117*, 12618.

18. Himo, F.; Eriksson, L. A. *J. Chem. Soc., Perkin Trans. 2* **1998**, 305.

19. Ding, Y.; Krogh-Jespersen, K. *Chem. Phys. Lett.* **1992**, *199*, 261.

20. Barone, V.; Adamo, C.; Grand, A.; Subra, R. *Chem. Phys. Lett.* **1995**, *242*, 351.

21. Rega, N.; Cossi, M.; Barone, V. *J. Am. Chem. Soc.* **1998**, *120*, 5723.

22. Ban, F.; Wetmore, S. D.; Boyd, R. J. *J. Phys. Chem.* A **1999**, *103*, 4303.

23. Malkin, V. G.; Malkina, O. L.; Eriksson, L. A.; Salahub, D. R. In *Modern Density Functional Theory, A Tool for Chemistry*, Politzer P., Seminario, J. M., Eds.; Elsevier: New York, **1995**; p273.

24. Engels, B.; Eriksson, L. A.; Lunell, S. *Adv. Quantum Chem.* **1997**, *27*, 298.

25. (a) Wetmore, S. D.; Boyd, R. J.; Eriksson, L. A. *J. Phys. Chem.* B **1998**, *102*, 5369. (b) Wetmore, S. D.; Himo, F.; Boyd, R. J.; Eriksson, L. A. *J. Phys. Chem.* B **1998**, *102*, 7484. (c) Wetmore, S. D.; Boyd, R. J.; Eriksson, L. A. *J. Phys. Chem.* B **1998**, *102*, 7674. (d) Wetmore, S. D.; Boyd, R. J.; Eriksson, L. A. *J. Phys. Chem.* B **1998**, *102*, 9332. (e) Wetmore, S. D.; Boyd, R. J.; Eriksson, L. A. *J. Phys. Chem.* B **1998**, *102*, 10602.

26. Lahorte, P.; Proft. F. D.; Vanhaelewyn, G.; Masschaele, B.; Cauwels, P.; Callens, F.; Geerlings, P.; Mondelaers, W. *J. Phys. Chem.* A **1999**, *103*, 6650.

27. Ban, F.; Gauld, J. W.; Boyd, R. J. *J. Phys. Chem.* A **2000**, *104*, 5080.

28. Scott, A. P.; Radom L. *J. Phys. Chem.* **1996**, *100*, 16502.

29. Perdew, J. P.; Wang, Y. *Phys. Rev.* B **1986**, *33*, 8800.

30. (a) Perdew, J. P. *Phys. Rev.* B **1986**, *33*, 8822. (b) Perdew, J. P. *Phys. Rev.* B **1986**, *34*, 7406.

31. Lassmann, G.; Eriksson, L. A.; Himo, F.; Lendzian, F.; Lubitz, W. *J. Phys. Chem.* A **1999**, *103*, 1283.

32. Eriksson, L. A. *Mol. Phys.* **1997**, *91*, 827.

33. Easton, C. J. *Chem. Rev.* **1997**, *97*, 53.

Interpreting the Radicals of L-α-alanine

4.1 Introduction

Amino acid radicals are involved in many biological reactions.[1-3] Considerable attention has been focused on the formation, stability and reactions of protein radicals in biological systems.[3] In addition, oxidative damage to amino acids is of importance in pharmacology, pathology and radiation biology.[2b,4] Amino acids were among the first irradiated biomolecules studied by the techniques of electron spin resonance spectroscopy. Fundamental work on X- and γ-irradiated single crystals of amino acids remains an active field.[5,6] Many studies of the radicals generated by irradiation of L-α-alanine have been published.[7-19] Particular interest in L-α-alanine has arisen due to its radiation dosimetric properties. Several spin-trapping studies[20,21] detected only one alanine-derived radical (R1) in polycrystalline samples, and more initial studies assumed that all variations in the ESR spectra of L-α-alanine-derived radicals were given by various properties of the radical R1.[22-24] However, it has been suggested [7,17,22-24,25,26] that the spectra of several radicals could be overlapping. This hypothesis was proven by Sagstuen et al.[6] In their study, two new radicals were clearly detected by a combination of ESR and related techniques. Thus, to date three radicals have been found upon the X-

irradiation of L-α-alanine crystals at 295 K. The radical structures were tentatively

assigned to be those displayed in Figure 4.1.

$$
\underset{\text{L-}\alpha\text{-alanine}}{H_2N\!\!-\!\!\overset{\displaystyle CH_3}{\underset{\displaystyle H}{C}}\!\!-\!\!COOH}
\qquad
\underset{R1}{H_3C\!\!-\!\!\overset{\displaystyle H}{\underset{\displaystyle \bullet}{C}}\!\!-\!\!COOH}
\qquad
\underset{R2}{H_3\overset{+}{N}\!\!-\!\!\overset{\displaystyle CH_3}{\underset{\displaystyle \bullet}{C}}\!\!-\!\!COO^-}
\qquad
\underset{R3}{H_2N\!\!-\!\!\overset{\displaystyle CH_3}{\underset{\displaystyle \bullet}{C}}\!\!-\!\!COOH}
$$
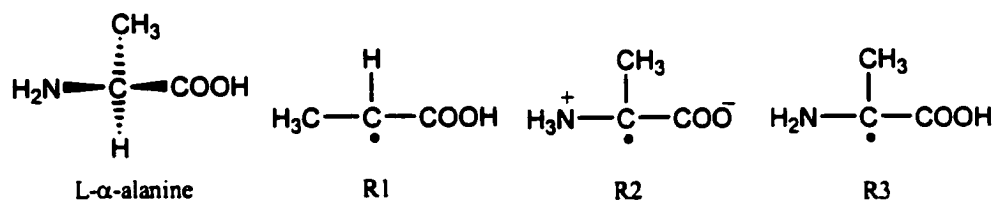
Figure 4.1 Structure of L-α-alanine and the proposed radicals formed upon X-irradiation of L-α-alanine crystals at 295 K.

From a simulated spectrum,[6] it was concluded that radicals R1 and R2 are present

in comparable amounts (with an approximate ratio of 60% to 40%). R3 was recognized

as a minor species. It was estimated that the α-C spin density of the two proposed

conformers of R3 should be on the order of 35-40%. R1 is a deamination product, R2 is

a hydrogen-abstraction product, and R3 is a product of hydrogen-abstraction

accompanied by proton transfers. Alternatively, R3 could be generated from R2 as will

be proposed in a later section. In the radiation chemistry of amino acids, the deamination

product can be formed from a protonated anion through a reductive pathway, while the

oxidation product can be formed from a cation. In L-α-alanine crystals irradiated at 77

K, an unusual cation[14] has been postulated to explain the ESR spectrum of the oxidation

product, but the oxidation product has not been detected. It seems that all radicals

generated in irradiated L-α-alanine crystals at 295 K follow the reductive path. However,

since the oxidation radical is very unstable,[27,28] it can abstract hydrogen from an alanine

molecule to form R2. Thus, the mechanism leading to R2 is unclear.[6]

Great effort[17] has been made to obtain a rough estimate of the coordinates of R1 in a unit cell. Although a few considerations[6] of the geometrical conformation of R2 have been made by considering the Heller-McConnell relation,[29] relatively less information is available for the structures of R2 and R3. However, further insight into the chemical nature of the radicals may be obtained from theoretical prediction of their structures and hyperfine coupling constants.

DFT has been shown to yield very accurate hyperfine coupling constants (HFCCs) for species such as DNA-related radicals.[30] This has prompted a systematic study[31] on L-α-alanine-derived radicals for a better understanding of the properties of irradiated amino acids..

As mentioned in Chapter 3, amino acids exist as zwitterionic species in the crystalline state and in the solution, and radiation may produce amino acid radicals in a zwitterionic form (such as R2 in Figure 4.1). Because the zwitterionic structures of amino acids and their derived radicals do not correspond to energy minima in the gas phase,[32,33] a combined computational scheme of the B3LYP method and the Onsager model has been applied for obtaining the zwitterionic structure of the L-α-alanine-derived radical R2 using the Gaussian 94 program. The other computational details are identical to those in Chapter 3.

4.2 Results and Discussion

4.2.1 Optimized Geometries

The molecular structures of R1, R2 and R3 were fully optimized at the B3LYP/6-31+G(d,p) level. Four different minima for both R1 and R3 were found due to the fact that the proton has two possible positions on each of the oxygen atoms in the carboxylate group. Only one minimum of the zwitterionic form of R2 was found using the standard Onsager model with a dielectric constant (ε) of 78.39 and an estimated radius of 3.76 Å for the spherical cavity. Select geometrical parameters of R1, R2 and R3 are shown in Figure 4.2. The relative energies of the four conformers of R1 and R3 are shown in Table 4.1.

All four structures of R1 and the zwitterionic structure of R2 have a planar skeleton (except for the hydrogen atoms in the methyl and amino groups). Thus, R1 and R2 are typical π-radicals. On the other hand, in all four structures of R3, the nitrogen atom sticks out of the $C_1C_2C_3$ plane by 3.2 to 6.4°. Thus, the structures of R3 are slightly pyramidal.

The main differences in the four structures of R1 caused by the arrangement of the OH_x bond are the reorganization of the atoms in the molecular plane. The largest changes are 0.028Å in bond length (CO bond) and 11.6° in bond angle ($\angle O_1C_1C_2$). From the relative energies, it can be seen that R1-II and R1-IV with intramolecular

hydrogen bonding are more stable than R1-I and R1-III. Also, it can be seen that in R1-III the interaction between H_x and the methyl group causes a staggered arrangement of the two H_β's with respect to the OH_x bond.
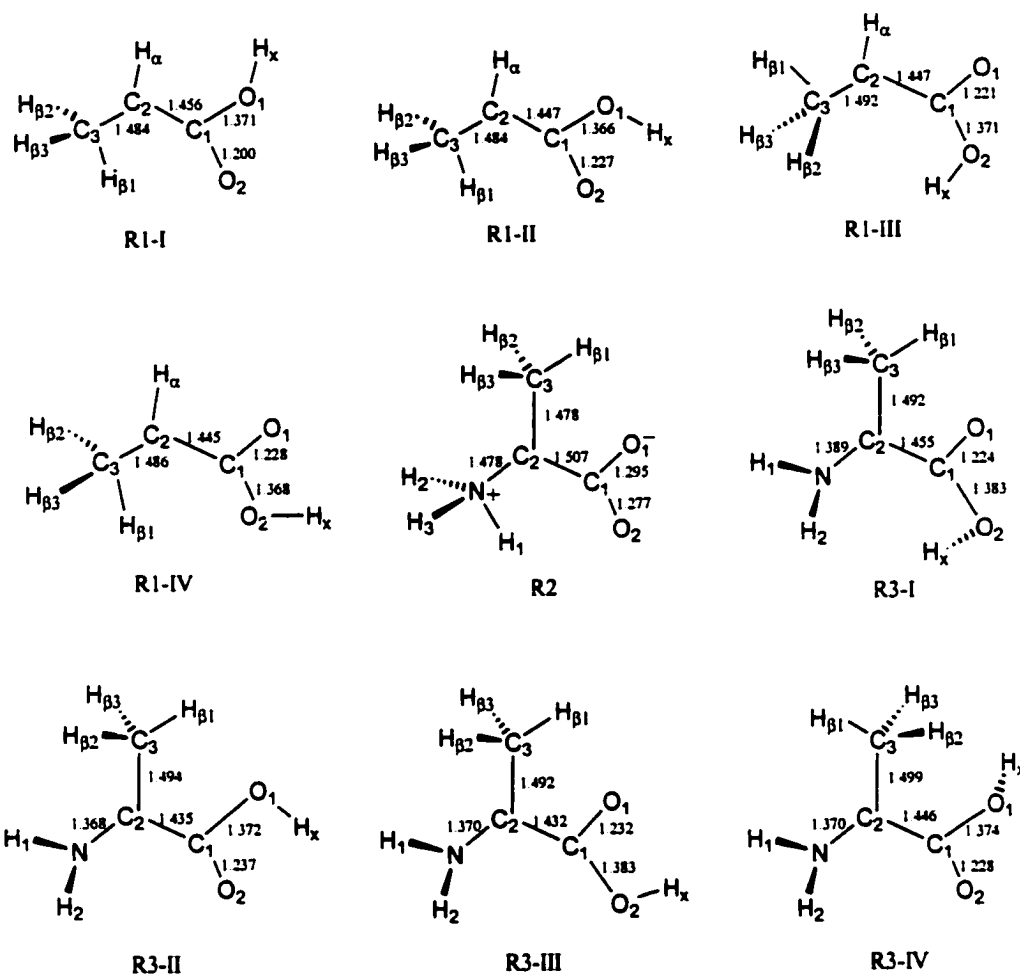
Figure 4.2 Optimized structures for R1, R2 (using the Onsager model) and R3 at the B3LYP/6-31+G(d,p) level (bond lengths in Å)

Besides a similar change in bond length as discussed for R1, there is a larger difference in the out-of-plane distortion between R3-I and the other three conformers (R3-II, R3-III, and R3-IV). The dihedral angles involving the amino hydrogens and the

two carboxylate oxygen atoms in R3-I differ by at least 10° from the corresponding

angles in R3-II, R3-III, and R3-IV. From the relative energies, it can be seen that R3-II

and R3-III are more stable than R3-I and R3-IV, due to the intramolecular hydrogen

bonding.

Table 4.1: The relative energies of the conformers of R1 and R3 (kJ mol⁻¹).

System	I	II	III	IV
R1	22.9	0.0	29.9	3.8
R3	37.7	0.0	1.9	28.0

4.2.2 Hyperfine Couplings of Radical ˙CH(CH₃)COOH

The calculated full hyperfine tensors of radical R1 are listed in Table 4.2, together
with the experimentally determined tensors for comparison. The isotropic coupling
constants of H_α in the four structures of R1 are all close in value, and in good agreement
with experiment. The computed T_{yy} component has a different sign from the
experimental value, and T_{zz} deviates from the experimental value by as much as 6 MHz
for all conformers. These deviations could be caused by crystal-packing effects, which
are not accounted for in the gas phase calculations. However, the principal components
are in reasonable agreement with the experimental tensors. In addition, the computed
average of the methyl proton couplings (the average A_{iso} for H_β's is approximately 65
MHz) in each conformer is in good agreement with the experimental value (69.9 MHz).
The deviations of the calculated average anisotropic components seem larger than
expected, mainly due to their relatively small values. However there is no doubt from the
calculations that all four conformers are candidates for the molecular structure of radical
R1 in the solid state.

Table 4.2: Comparison of calculated and experimental[6] hyperfine couplings (MHz) of R1.

Tensor	HFCC	R1-I	R1-II	R1-III	R1-IV	exptl.
H_α	A_{iso}	-52.0	-54.0	-54.9	-52.9	-56.1
	T_{xx}	-32.5	-32.1	-31.7	-30.9	-31.8
	T_{yy}	-1.4	-1.7	-1.8	-2.1	3.9
	T_{zz}	33.9	33.8	33.5	33.0	27.9
	A_{xx}	-84.5	-84.0	-86.6	-83.5	-87.9
	A_{yy}	-53.4	-52.8	-56.7	-54.7	-52.7
	A_{zz}	-18.1	-17.8	-21.4	-21.4	-28.3
$H_{\beta 1}$	A_{iso}	1.7	1.7	2.0	1.5	
	T_{xx}	-3.9	-4.0	-3.9	-3.6	
	T_{yy}	-2.8	-2.8	-3.4	-3.4	
	T_{zz}	6.7	6.8	7.3	7.1	
$H_{\beta 2}$	A_{iso}	96.3	96.9	93.6	97.0	
	T_{xx}	-4.8	-4.8	-4.7	-4.8	
	T_{yy}	-3.0	-3.0	-3.1	-3.0	
	T_{zz}	7.8	7.8	7.8	7.8	
$H_{\beta 3}$	A_{iso}	97.5	98.3	95.2	98.6	
	T_{xx}	-4.8	-4.8	-4.6	-4.8	
	T_{yy}	-3.0	-3.1	-3.1	-3.1	
	T_{zz}	7.9	7.9	7.7	7.9	
$H_{\beta(ave)}$	A_{iso}	65.2	65.6	63.4	65.7	69.9
	T_{xx}	-4.5	-4.5	-4.5	-4.4	-2.6
	T_{yy}	-2.9	-3.0	-3.2	-3.2	-2.3
	T_{zz}	7.5	7.5	7.5	7.6	4.8

It has been proposed[10] that R1 is generated from a primary carboxylate anion radical (Figure 4.3) through a deamination reaction. Mayagawa et al[12] raised an interesting question of specific proton transfer in irradiated crystalline L-α-alanine at low temperatures, and concluded through an ESR study at 80 K that the transferred proton specifically binds to the O_2 atom in the COO plane in a position directed towards O_1. Later, Muto et al.[15] re-examined this problem at 77 K using EPR and ENDOR techniques and obtained the opposite conclusion that the transferred proton stereospecifically attaches to O_1 along a direction perpendicular to the COO plane and is trapped outside

the COO plane. This arrangement was supported by a large positive isotropic coupling assigned to the transferred proton at 77 K. If R1 is formed by a deamination reaction from the stereospecifically proton transferred carboxylate anion radical, there will be only one conformer corresponding to R1. However, the calculated HFCCs suggest that the four conformers of R1 could exist simultaneously. In addition, since no evidence exists to exclude a possible proton transfer to O_1 and O_2 at 295 K, there could be an equilibrium between the four conformations. Also, it can be seen from the calculations that this problem cannot be solved by a proton ESR study, because the proton couplings of all conformers are very close to each other.
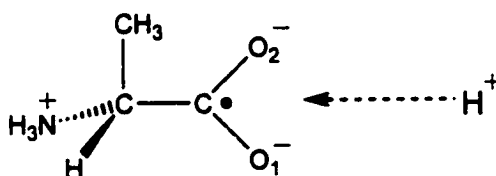
Figure 4.3 Proton transfer to the carboxylate anion radical.

4.2.3 Hyperfine Couplings of Radical $H_3N^+C^\bullet(CH_3)COO^-$

In Table 4.3, the computed full coupling tensor from the optimized structure of R2 is listed, along with the experimental hyperfine coupling values for comparison. For all of the protons of the amino group, great discrepancies between the computed isotropic HFCCs and the experimental values were found. However, the average of the three calculated amino proton isotropic HFCCs (47.4 MHz) is quite close to the average of the three experimental couplings (42.2 MHz) and the averages of the anisotropic couplings are also in good agreement. In spite of the above deviations, all the calculated

anisotropic components of the amino protons are in good agreement with the corresponding experimental values. The average of the calculated isotropic coupling constants for the three methyl protons (64.5 MHz) is very close to the experimental average (70.8 MHz). In addition, good agreement for the anisotropic components of the methyl protons is found. These observations confidently show that the optimized structure of radical R2 accounts for the hyperfine couplings in the crystalline environment except for the isotropic couplings of the three amino-group protons. This prompts a careful study of the effects of the rotation about the N—C_2 bond on the amino proton HFCCs.

Table 4.3: Comparison of calculated and experimental[6] hyperfine couplings (MHz) of R2.

Tensor	A_{iso}^{cal}	T_{xx}^{cal}	T_{yy}^{cal}	T_{zz}^{cal}	A_{iso}^{exp}	T_{xx}^{exp}	T_{yy}^{exp}	T_{zz}^{exp}
H_1	2.4	-5.6	-4.9	10.6	86.3	-6.9	-2.7	9.5
H_2	69.9	-4.9	-4.5	9.4	30.2	-6.1	-4.7	10.7
H_3	69.9	-4.8	-4.5	9.3	10.2	-4.9	4.8	9.7
$H_{amino(ave)}$	47.4	-5.1	-4.6	9.8	42.2	-6.0	-4.1	10.0
$H_{\beta 1}$	2.2	-4.1	-3.9	8.0				
$H_{\beta 2}$	95.5	-4.6	-3.4	8.0				
$H_{\beta 3}$	95.7	-4.6	-3.4	8.0				
$H_{\beta(ave)}$	64.5	-4.3	-3.6	8.0	70.8	-2.9	-2.7	5.6

The difference between experiment and theory is suggested to arise from the relative orientation of the three amino protons in the L-α-alanine crystals. A detailed investigation of the rotational effects of the amino group about the N—C_2 bond on the isotropic HFCCs of the amino protons supports this idea. Figure 4.6 shows the variation in the three amino proton HFCCs as a function of the rotation angle. The rotation of the amino group was carried out by increasing the dihedral angle $H_1NC_2C_1$ by 30° starting from $H_1NC_2C_1 = 0.0$°.
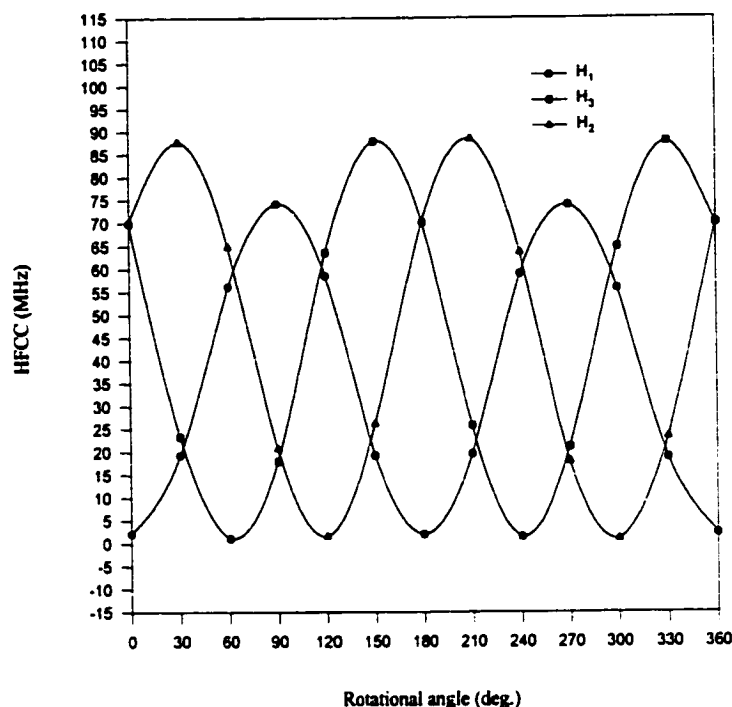
Figure 4.3 The amino proton HFCCs versus the rotation angle about the N—C_2 bond for R2

From the curve, it can be seen that the isotropic HFCCs of the three amino

protons change dramatically, but the anisotropic components fluctuate very little (not

shown). This is not surprising since the isotropic component of the HFCC is calculated

by summing the contributions only at one particular point in space, while the anisotropic

components are computed by integrating over all space. Interestingly, at $H_1NC_2C_1\approx40°$,

there is an excellent fit of the calculated isotropic couplings [H_1 (30 MHz), H_2 (12 MHz)

and H_3 (86 MHz)] to the experimental values (30.2, 10.2, 86.3 MHz). Thus, it can be

concluded that the configuration at $H_1NC_2C_1\approx40°$ corresponds to the structure of R2 in

the L-α-alanine crystal at 295 K, in which the amino protons are fixed by intermolecular hydrogen bonds.

The Onsager model satisfactorily describes the zwitterionic structures of the amino acid radicals, which is required to accurately calculate the HFCCs. Since the experimental results can be explained through a rotation study with this solvation model, more computationally demanding models do not need to be investigated.

4.2.4 Hyperfine Couplings of $H_2NC^\bullet(CH_3)COOH$

The computed full hyperfine coupling tensors of R3 and the experimentally determined tensors are listed in Table 4.4. Experimentally two coupling tensors were elucidated and assigned to a rapidly rotating methyl group. Investigation of the average of the calculated methyl proton isotropic HFCCs in the four conformers of R3 isolates the conformers into two groups. One group contains only R3-I with an averaged methyl proton isotropic HFCC equal to 41.3 MHz, which is in excellent agreement with one of the experimental values (39.5 MHz). The second group includes R3-II, R3-III, and R3-IV with an averaged methyl proton isotropic HFCC of approximately 35 MHz, which is in excellent agreement with the second experimental value (33.1 MHz). The largest deviation is less than 1.6 MHz. In addition, all of the anisotropic components for both group one and group two are in nearly perfect agreement with the corresponding experimental values. This leads to the conclusion that at least two conformers of R3 exist in the irradiated L-α-alanine crystals at 295 K. R3-I could be one conformer and the

second conformer could be either R3-II, R3-III or R3-IV. Another possibility is that the

observed spectra arise from a mixture of all four conformations.

Table 4.4: Comparison of calculated and experimental[6] hyperfine couplings (MHz) of R3.

tensor	HFCC	R3-I	R3-II	R3-III	R3- IV	exptl	
$H_{\beta 1}$	A_{iso}	1.5	2.0	46.9	19.0		
	T_{xx}	-3.9	-3.4	-3.7	-3.5		
	T_{yy}	-2.7	-3.2	-2.7	-3.2		
	T_{zz}	6.6	6.6	6.4	6.6		
$H_{\beta 2}$	A_{iso}	61.1	61.2	56.0	71.7		
	T_{xx}	-3.5	-3.3	-3.5	-3.5		
	T_{yy}	-3.2	-3.0	-2.8	-2.9		
	T_{zz}	6.7	6.4	6.3	6.4		
$H_{\beta 3}$	A_{iso}	60.5	43.7	1.4	15.7		
	T_{xx}	-3.6	-3.5	-3.5	-3.3		
	T_{yy}	-2.9	-2.8	-2.7	-2.8		
	T_{zz}	6.6	6.3	6.2	6.1		
$H_{\beta(avc)}$	A_{iso}	41.3	35.6	34.8	35.4	39.5	33.1
	T_{xx}	-3.7	-3.4	-3.6	-3.4	-2.7	-2.3
	T_{yy}	-3.2	-3.0	-2.7	-3.0	-2.2	-2.3
	T_{zz}	6.6	6.3	6.3	6.4	5.0	4.6

Comparison of the molecular structure of R2 with that of R3-I leads to a possible

mechanism for the formation of R3-I. In particular, R3-I can be formed from radical R2

through an intramolecular proton transfer. Alternatively, R2 could be formed from R3-I

through an intramolecular proton transfer. However, the other three conformers appear to

be products of intermolecular proton transfer.

A more interesting correlation of the radical structure to the HFCCs is found

when the coplanarity of H_1, H_2, N and C_2 is examined. Table 4.5 lists the sum of the

three bond angles of the amino group and the N—C_2 bond length in R3-I, R3-II, R3-III,

and R3-IV.

Table 4.5: The sum of the three bond angles (degrees) of the amino group and the N—C_2 bond length in R3 (Å).

structure	$\angle H_1NC_2$	$\angle H_2NC_2$	$\angle H_1NH_2$	sum	R(N—C_2)
R3-I	116.1	117.4	112.4	345.9	1.389
R3-II	120.1	116.8	117.8	354.7	1.368
R3-III	119.6	117.1	117.1	355.4	1.370
R3-IV	119.9	117.3	117.3	352.7	1.370

From the results, it can be seen that the amino group of the four conformers tends to be planar, but the sums of the three bond angles fall into two groups. Only R3-I is in the first group, while R3-II, R3-III, and R3-IV are in the second group. The sum of the three bond angles in R3-I is at least 6.8° less than that of the second group. This indicates a larger π-conjugation in the second group. This statement is supported by comparison of the N—C_2 bond lengths of the four conformers. All the N—C_2 bond lengths in the second group are approximately 0.02 Å shorter than that of R3-I. Thus, the difference in the isotropic HFCCs of the two groups can be interpreted by the spin polarization of the unpaired α spin electron at the C_2 atom. More specifically, the more planar the amino group, the more easily the spin polarization from the lone pair electrons of the N atom can occur. Consequently, the more planar the amino group in R3, the lower the α (positive) spin density on the C_2 atom, and the more α spin density on the N atom. Hence, the methyl proton isotropic HFCC will be smaller in the more planar radicals.

Table 4.6 lists the spin density of the N, C_2, and O atoms in R3, together with the semiempirical molecular orbital values[6] for comparison.

Table 4.6: Spin density from DFT(PWP86) and semiempirical[6] calculations on the C_2, N and O atoms in R3.

atom	R3-I	R3-II	R3-III	R3-IV	semiempirical
C_2	0.597	0.519	0.521	0.537	0.45
N	0.162	0.232	0.222	0.235	0.20
O_1+O_2	0.203	0.185	0.206	0.181	
$O^{carbonyl}$	0.188	0.146	0.183	0.150	0.25

It can be seen that R3-I has a larger spin density on the C_2 atom than the members of the second group. Thus R3-I possesses a larger methyl proton isotropic HFCC than R3-II, R3-III, and R3-IV due to a greater distortion at the amino group and therefore less spin polarization can occur. Also it can be seen that density functional theory calculations give a much better resolution of the spin density distribution compared with the semiempirical methods. The DFT calculations presented herein predict that the spin density residing on C_2 in the four conformers is greater than 51%. The total spin density on O_1 and O_2 is between 18.1% and 20.6%, and the spin density on the single carbonyl carbon is less than 18.8%. The N spin density is between 16.2% and 23.5%. These predictions are numerically different from the semiempirical molecular orbital values (about 45%, 25% and 20% for C_2, carbonyl oxygen and N atom, respectively).

4.4 Conclusions

The geometries and hyperfine coupling constants of the radiation products of L-α-alanine have been computed using density functional theory. The calculated results have been compared with the experimental values obtained from X-irradiated crystals of L-α-alanine. The three main radiation products (R1, R2, and R3) have been discussed.

Four conformations of R1 were optimized and their hyperfine couplings support the experimental assignment to this radical. Unusual discrepancies between the calculated and the experimental values of the T_{yy} and T_{zz} anisotropic components for H_α were observed. These differences could be caused by crystal-packing effects that are not accounted for in the calculations.

The standard Onsager model with a dielectric constant of 78.39 predicts a planar zwitterionic structure for R2. A careful study of the rotational effects of the amino group on the amino proton hyperfine couplings shows that the conformation with $\angle H_1 N C_2 C_1 \approx 40^\circ$ corresponds to the R2 structure in the L-α-alanine crystals, in which the amino protons are fixed by the intermolecular hydrogen bonds. Thus, the geometry obtained from the Onsager model is adequate to describe the HFCCs in this radical and more complex solvation models are not required to explain experimental results. The calculated hyperfine couplings of R2 show that the crystal environment has little effect on the alanine radical in its zwitterionic form, consistent with a previous investigation of the glycine radical.[35]

Four conformers were investigated for radical R3 providing much more information about the structure of this radical. The conformers fall into two groups. The averages of the calculated methyl proton hyperfine couplings of each group match the experimental couplings perfectly. These results give solid support to the experimental assignment of the detected tensors. A very good correlation of the structure of the amino group to the spin polarization of the unpaired electron on the C_2 atom was found. This correlation accounts for the fact that the methyl proton hyperfine couplings of the four

conformations of R3 fall into two groups and reproduce the two experimentally distinguishable coupling tensors.

Methodologically, it can be seen again that density functional theory is very successful in predicting the magnetic properties of amino acid radicals, and that the Onsager model can predict structures for amino acid radicals in their zwitterionic form which are accurate enough to reproduce experimental hyperfine coupling constants.

References

1. (a) Stubbe, J.; van der Donk, W. A. *Chem. Rev.* **1998**, *98*, 705. (b) Stubbe, J. *Annu. Rev. Biochem.* **1989**, *58*, 257. (c) Stubbe, J. *Biochemistry* **1988**, *27*, 3593.

2. (a) Davies, M. J.; Fu, S.; Dean, R. T. *Biochem. J.* **1995**, *305*, 643. (b) Dean, R. T.; Fu, S.; Stocker, R.; Davies, M. J. *Biochem. J.* **1997**, *324*, 1.

3. Van der Zee, J. *Biochem. J.* **1997**, *322*, 633.

4. (a) Rauk, A.; Armstrong, D. A. *J. Am. Chem. Soc.* **2000**, *122*, 4185. (b) Rauk, A.; Armstrong, D. A.; Fairlie, D. P. *J. Am. Chem. Soc.* **2000**, *122*, 9761. (c) Stadtman, E. R. *Annu. Rev. Biochem.* **1993**, *62*, 797. (d) von Sonntag, C. *The Chemical Basis of Radiation Biology*, Taylor & Francis: London, 1987.

5. Brustolon, M.; Chis, V.; Maniero, A. L.; Brunel. L. *J. Phys. Chem.* A **1997**, *101*, 4887.

6. Sagstuen, E.; Hole, E. O.; Haugedal, S. R.; Nelson, W. H. *J. Phys. Chem.* A **1997**, *101*, 9763.

7. Miyagawa, I.; Gordy, W. *J. Chem. Phys.* **1960**, *32*, 255.

8. (a) Morton, J. R.; Horsfield, A. _J. Chem. Phys._ **1961**, _35_, 1143. (b) Horsfield, A.; Morton, J. R.; Whiffen, D. H. _Mol. Phys._ **1962**, _4_, 425. (c) Horsfield, A.; Morton, J. R.; Whiffen, D. H. _Mol. Phys._ **1962**, _5_, 115.

9. Miyagawa, I.; Itoh, K. _J. Chem. Phys._ **1962**, _36_, 2157.

10. (a) Sinclair, J. W.; Hanna, M. W. _J. Phys. Chem._**1967**, _71_, 84. (b) Sinclair, J. W.; Hanna, M. W. _J. Chem. Phys._ **1969**, _50_, 2152.

11. Minegishi, A.; Shinozaki, Y.; Meshitsuka, G. _J. Chem. Soc. Jpn._ **1967**, _40_, 1549.

12. Miyagawa, I.; Tamura, N.; Cook, J. W. _J. Chem. Phys._ **1969**, _51_, 3520.

13. Davidson, R.; Miyagawa, I. _J. Chem. Phys._ **1970**, _52_, 1727.

14. Friday, E. A.; Miyagawa, I. _J. Chem. Phys._ **1971**, _55_, 3589.

15. Muto, H.; Iwasaki, I. _J. Chem. Phys._**1973**, _59_, 4821.

16. Muto, H.; Iwasaki, I.; Ohkuma, J. _J. Magn. Reson._ **1977**, _25_, 327.

17. Kuroda, S.; Miyagawa, I. _J. Chem. Phys._ **1982**, _76_, 3933.

18. Matsuki, K.; Miyagawa, I. _J. Chem. Phys._**1982**, _76_, 3945.

19. Brudstolon, W.; Segre, U. _Appl. Magn. Reson._ **1994**, _7_, 405.

20. Minegishi, A.; Bergene, R.; Riesz, P. _Int. J. Radiat. Biol._ **1980**, _38_, 627.

21. Lion, Y.; Denis, G.; Mossoba, M. M.; Riesz, P. _Int. J. Radiat. Biol._ **1983**, _43_, 71.

22. Simmons, J. A. _J. Chem. Phys._ **1962**, _36_, 469.

23. Arber, J. M.; Sharpe, P. H. G.; Joly, H. A.; Morton, J. R.; Preston, K. F. _Appl. Radiat. Isotop._ **1991**, _42_, 665.

24. Ciesielski, B.; Wielopolski, L. _Radiat. Res._ **1994**, _140_, 105.

25. Sevilla, M. D. _J. Phys. Chem._ **1970**, _74_, 2096.

26. Sevilla, M. D.; Brook, V. L. _J. Phys. Chem._ **1973**, _77_, 2954.

27. Sinclair, J. _J. Chem. Phys._ **1971**, _55_, 245.

28. Box, H. C. *Radiation Effects, ESR and ENDOR Analysis*, Academic Press: New York, 1977; p120.

29. Heller, C.; McConnell, H. M. *J. Chem. Phys.* **1960**, *32*, 1535.

30. (a) Wetmore, S. D.; Boyd, R. J.; Eriksson, L. A. *J. Phys. Chem.* B **1998**, *102*, 5369. (b) Wetmore, S. D.; Himo, F,; Boyd, R. J.; Eriksson, L. A. *J. Phys. Chem.* B **1998**, *102*, 7484. (c) Wetmore, S. D.; Boyd, R. J.; Eriksson, L. A. *J. Phys. Chem.* B **1998**, *102*, 7674. (d) Wetmore, S. D.; Boyd, R. J.; Eriksson, L. A. *J. Phys. Chem.* B **1998**, *102*, 9332. (e) Wetmore, S. D.; Boyd, R. J.; Eriksson, L. A. *J. Phys. Chem.* B **1998**, *102*, 10602.

31. Ban, F.; Wetmore, S. D.; Boyd, R. J. *J. Phys. Chem.* A **1999**, *103*, 4303.

32. Ding, Y.; Krogh-Jespersen, K. *Chem. Phys. Lett.* **1992**, *199*, 261.

33. Barone, V.; Adamo, C.; Grand, A.; Subra, R. *Chem. Phys. Lett.* **1995**, *242*, 351.

Elucidating the Radiation Products of

Hydroxyproline

5.1 Introduction

Since the 1950's, electron spin resonance (ESR) techniques have been used to study the radiation chemistry of amino acids.[1] Upon irradiation, an amino acid may form either its primary radical cation or anion by ejection or capture of an electron. These primary radicals may then undergo further reactions, generally by decarboxylation or deamination of the primary radical cation or anion, respectively, to give various secondary radicals. Characterization and identification of the resulting radicals by ESR is often difficult, however, as found in the case of proline and related systems.[2-6]

Of all the essential amino acids, proline is unique in having a five-membered ring with a secondary amino group. In the 1980's, a number of studies were performed on X-ray irradiated L-proline monohydrate,[5] DL-proline•HCl,[3] hydroxyproline•HCl[6] and hydroxyproline[2,4] single crystals. Two conformations were proposed for the hydroxyproline primary radical anion (R1^A). A number of other hydroxyproline derived radicals were also proposed, including a secondary radical cation (R2^C) resulting from

decarboxylation, three conformations of secondary radicals resulting from deamination, and radicals resulting from H-abstraction at the C_2 and C_3 positions. In addition, several possible zwitterionic radicals resulting from irradiation of hydroxyproline[2,4] were also proposed. Due to complex and overlapping ESR spectra, however, the exact identification and characterization of many radicals and reaction intermediates was not possible. The experimentally proposed hydroxyproline-derived radicals are shown in Figure 5.1.
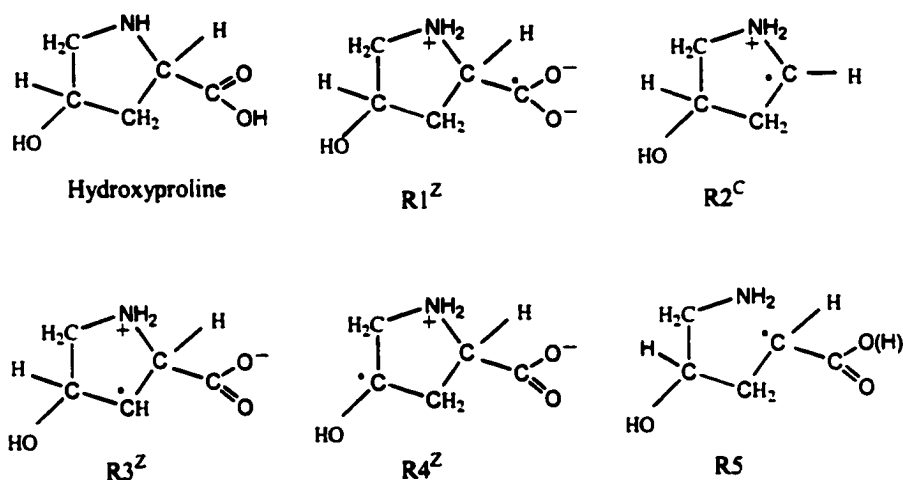
Figure 5.1 Schematic illustration of the structures of hydroxyproline and related radicals generated upon X-radiation.

Theoretical chemistry offers a complementary approach to experiment which can be used to gain greater insight into the radicals, and their reactions, produced upon irradiation of amino acids. Indeed, numerous studies have investigated the reliability of various computational schemes for the calculation of the hyperfine couplings of bioradicals.[7] In particular, density functional theory methods have been shown to give reliable structures and hyperfine coupling constants for a range of biological radicals

derived from amino acids,[8-14] quinones[15,16] and nucleic acid bases.[17] For the zwitterionic isomers, however, a slightly modified approach has been found to be necessary. This is due to the fact that the zwitterionic isomers of amino acids and their radicals often do not correspond to energy minima in the gas-phase, as exemplified by glycine[18] and its radical.[19,8] Thus, in order to obtain such structures the electrostatic effects of the crystalline environment must be taken into account. One approach is to treat electrostatic interactions of neighbouring molecules as a uniform dielectric continuum (Chapter 2). Previous calculations using the Onsager and related models for the zwitterions of glycine[8,9] and alanine[10] radicals, have been found to yield hyperfine coupling constants in good agreement with experiment.

In the present study, identical computational techniques as those previously used for glycine (in Chapter 3) have been employed to investigate possible radicals formed upon irradiation of hydroxyproline.[20]

5.2 Results and Discussion

5.2.1 The Radical Anion and Its Protonated Neutral Radical

Experimentally, upon irradiation of hydroxyproline no carboxylate hydrogen interactions were detected.[2,4] Thus, the observed H_β hyperfine tensors (see Table 5.1) were assigned to two different conformations of the zwitterionic radical $R1^{Z}$.[2,4] The optimized structures of possible conformers of $R1^{Z}$ using the Onsager model with a

radius of 4.35 Å are shown schematically in Figure 5.2, while the corresponding

calculated isotropic and anisotropic HFCCs are given in Table 5.1.

Table 5.1: Calculated, PWP86/6-311G(2d,p), H_β HFCCs (MHz) of $R1^Z$, $R1^A$ and $R1^P$ and experimental values. Relative energies (kJ mol^{-1}) of the conformers of $R1^A$ and $R1^P$.

system	A_{iso}	T_{xx}	T_{yy}	T_{zz}	ΔE^c
$R1^Z$-I	2.0	-5.0	-0.9	5.8	
$R1^Z$-II	4.9	-4.8	-0.5	5.3	
$R1^A$-I	32.3	-4.4	-3.5	7.9	0.0
$R1^A$-II	17.9	-4.3	-3.7	8.0	10.3
$R1^A$-III	18.5	-4.5	-3.8	8.3	12.5
$R1^A$-IV	6.2	-3.7	-2.4	6.0	35.9
$R1^P$-I	59.9	-5.1	-3.8	8.9	0.0
$R1^P$-II	58.8	-5.1	-3.8	8.9	1.4
$R1^P$-III	55.9	-5.3	-3.5	8.8	22.0
$R1^P$-IV	56.2	-5.3	-3.6	8.9	22.4
exptl I[a]	23.9	-6.2	-5.2	11.4	
exptl II[b]	61.0	-4.7	-2.1	6.9	

[a]Ref 2. [b]Ref 4. [c]B3LYP/6-311G(2df,p)//B3LYP/6-31+G(d,p) + ZPVE.
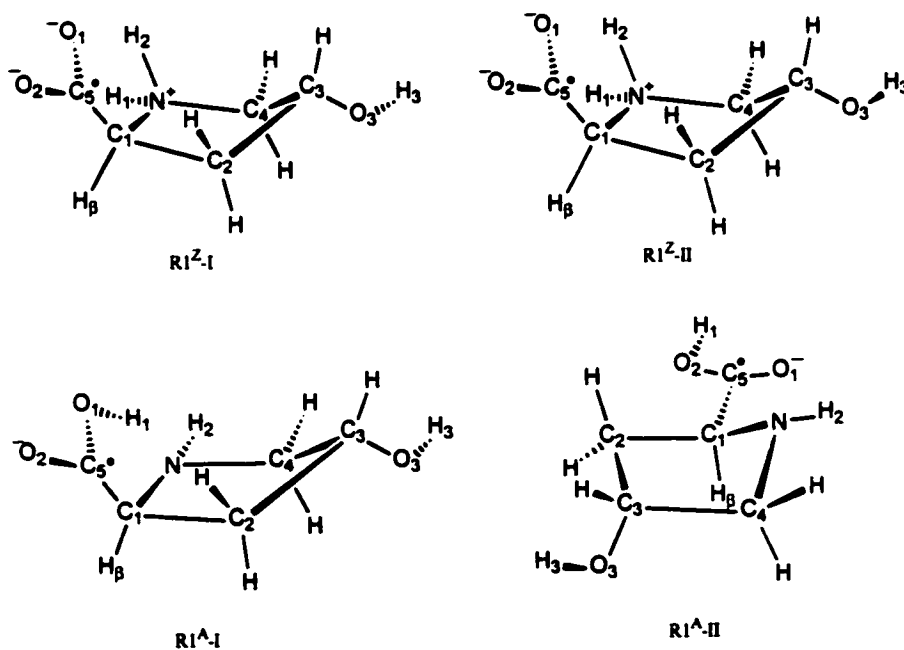
Figure 5.2 Optimized structures of $R1^Z$, $R1^A$ and $R1^P$ (continued over page).
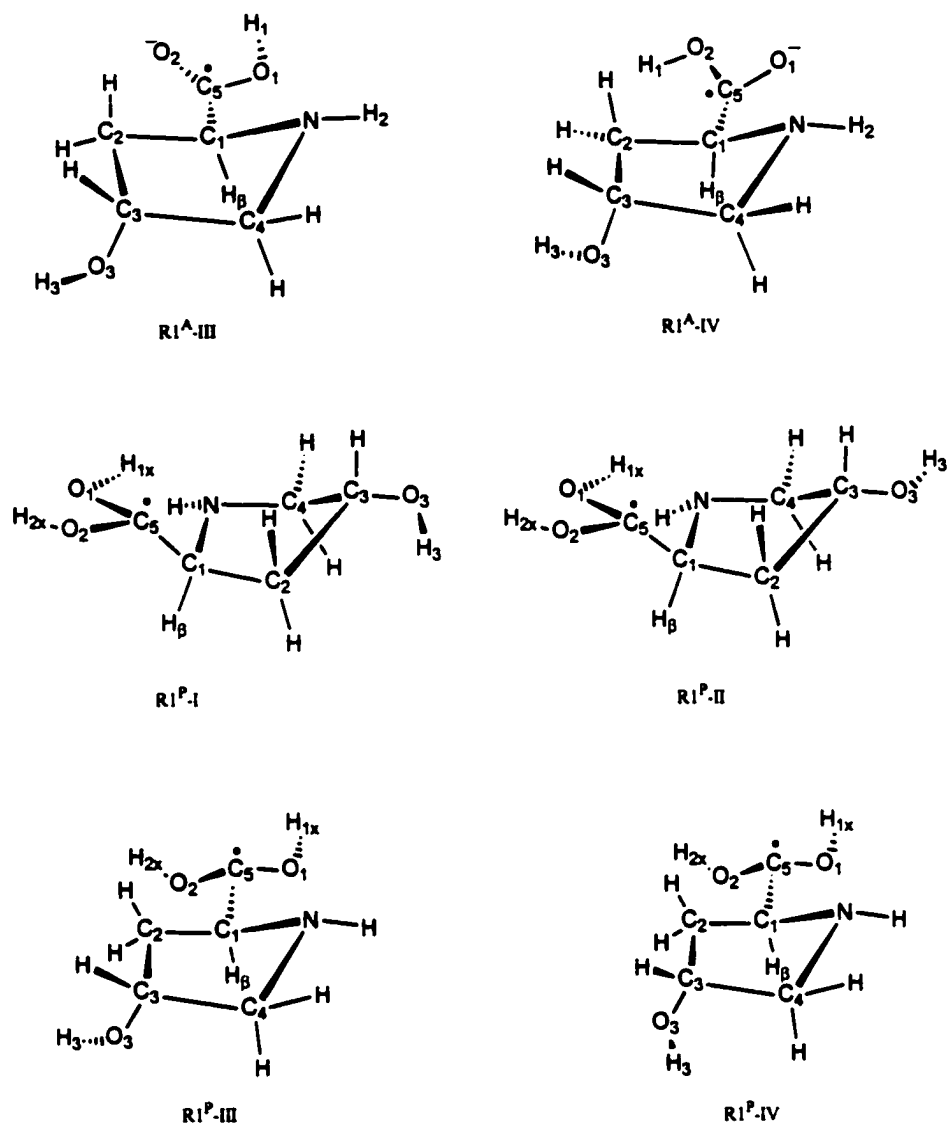
Figure 5.2 Optimized structures of $R1^Z$, $R1^A$ and $R1^P$.

Two possible conformers, $R1^Z$-I and $R1^Z$-II, of the zwitterionic radical anion $R1^Z$ were obtained. The main difference between $R1^Z$-I and $R1^Z$-II is the orientation of O_3–H_3. However, both conformers possess a half-chair conformation with the $-C_3HOH-$ moiety forming the apex, see Figure 5.2. The two structures both contain a reasonably

strong intramolecular $O_1\cdots H_2-N$ hydrogen bond ($r_{O\cdots H}<1.811$ Å) between the

positively-charged ring $-NH_2^+-$ group and the almost planar (see Table 5.2) anionic

carboxylate group. As can be seen from Table 5.1, the calculated H_β HFCCs of $R1^Z$

differ considerably from the experimentally observed values. Hence, it would appear

unlikely that either of the experimentally observed conformers is $R1^Z$.

Table 5.2: Optimized values of the angle $\angle O_1C_5O_2C_1{}^a$ in $R1^Z$, $R1^A$ and $R1^P$.

Radical	$R1^Z$-I	$R1^Z$-II	$R1^A$-I	$R1^A$-II	$R1^A$-III	$R1^A$-IV	$R1^P$-I	$R1^P$-II	$R1^P$-III	$R1^P$-IV
$\angle O_1C_5O_2C_1$	178.9	-179.8	175.8	160.5	159.5	167.4	133.7	133.8	130.4	130.3

^{a}Angles in degrees.

For the non-zwitterionic isomer ($R1^A$) of $R1^Z$, four possible conformers were

found; $R1^A$-I to $R1^A$-IV (see Figure 5.2). The main difference between the four

conformers is the orientation of O_1 or O_2-H_1 in the carboxyl group. All are found to have

a half-chair conformation with the $-NH-$ moiety forming the apex except for $R1^A$-I for

which the $-C_3HOH-$ moiety forms the apex. Since $R1^A$-I possesses a strong

intramolecular $O_1-H_1\cdots N$ hydrogen bond ($r_{N\cdots H_1}=1.818$ Å) while the other conformers

all possess a weak $O_1\cdots H_2-N$ hydrogen bond ($r_{O_1\cdots H_2}>2.692$ Å), it can be concluded

that the apexes of the $R1^A$ half-chair structures are dependent on the strength of the

hydrogen bond. Interestingly, for $R1^A$-II and $R1^A$-III the bases of the half-chairs are

almost perfectly planar while their carboxylic groups are more pyramidal than those of

$R1^A$-I and $R1^A$-IV (see Table 5.2).

The calculated isotropic and anisotropic H_β HFCCs for all $R1^A$ conformers are given in Table 5.1. The coupling constants for $R1^A$-II and $R1^A$-III are very similar, reflecting the close similarities in structure, and are in close agreement with one of the experimentally observed values (exptl I), see Table 5.1. The isotropic coupling constants for $R1^A$-I (32.3 MHz) and $R1^A$-IV (6.2 MHz), however, differ considerably from either of the experimentally observed values of 23.9 and 61.0 MHz. Furthermore, they also differ significantly from the calculated coupling constants of $R1^A$-II and $R1^A$-III. These results suggest that the experimentally observed conformer denoted as exptl I in this present study, is most probably $R1^A$-II or $R1^A$-III, or even possibly a mixture of the two (they are calculated to lie close in energy, see Table 5.1).

The large difference between the two experimentally observed H_β HFCCs suggests that there may in fact be a net change in the charge between the two conformers exptl I and exptl II, i.e., exptl II may in fact be a protonated form of exptl I. Thus, possible protonated conformers of $R1^A$ were investigated, the resulting radicals now being neutral radicals. Four possible conformers were obtained and can be divided into two groups with respect to the five-membered ring skeletal structures; $R1^P$-I, $R1^P$-II (group I) and $R1^P$-III, $R1^P$-IV (group II), see Figure 5.2. The main difference between the two conformers in each group is the O_3–H_3 orientations. Group I possesses relatively stronger intramolecular O_1–$H_{1x}\cdots N$ hydrogen bonds ($r_{N\cdots H_{1x}} \approx 2.044$ Å), with the – C_3HOH– moiety forming the apex of the five-membered ring. In contrast, group II possesses weaker intramolecular $O_1\cdots H$–N hydrogen bonds ($r_{O_1\cdots H} \approx 2.655$ Å), and the –

NH– moiety forms the apex. In both groups, however, the carbon of the protonated carboxylic group has become more pyramidal, as shown in Table 5.2.

The calculated H_β HFCCs of $R1^P$-I to $R1^P$-IV are given in Table 5.1. Groups I and II give similar H_β HFCCs. Importantly, however, they differ considerably from those calculated for $R1^A$. The calculated coupling constants of $R1^P$ are in good agreement with those previously assigned to a conformer of the zwitterion $R1^Z$ and denoted as exptl II in Table 5.1. This suggests that the experimentally observed couplings of exptl II in fact arise from a protonated derivative of the radical anion of hydroxyproline. The calculated relative energies (see Table 5.1) suggest that exptl II is most likely a conformer, or a mixture of both conformers, of group I.

5.2.2 Secondary Radical Cation Formed upon Decarboxylation

Four conformations of $R2^C$ were found and are illustrated schematically in Figure 5.3. As seen in Table 5.3, the two lowest energy conformers are $R2^C$-I and $R2^C$-II. In both radicals, the $-C_4(H_2)-$ moiety forms the apex of the five-membered ring due to the formation of the intramolecular $N-H_4\cdots O_1$ hydrogen bond. In $R2^C$-III and $R2^C$-IV, the – $C_3(HO_1H)-$ moiety is in the apical position of the five-membered ring, and both radicals lack intramolecular hydrogen bonds.
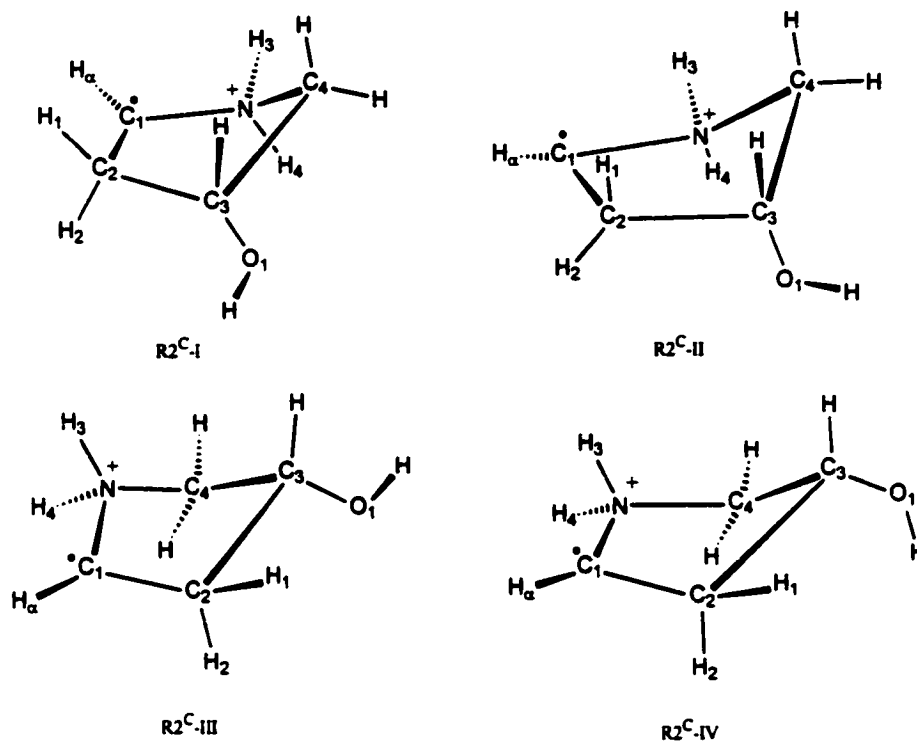
Figure 5.3 Optimized structures of R2^C.

For R2^C-I through R2^C-IV, the calculated and experimentally observed HFCCs of H$_\alpha$, H$_1$, H$_2$, H$_3$ and H$_4$ are listed in Table 5.3. On the basis of their calculated coupling constants, the four conformers can be divided into two groups. One group consists of R2^C-I and R2^C-II while the other consists of R2^C-III and R2^C-IV. The coupling constants of the two groups differ significantly, in particular for H$_1$, H$_3$ and, to a lesser extent, H$_4$ (see Table 5.3). The calculated coupling constants of H$_\alpha$ and H$_2$ appear to be less sensitive to the conformation. The calculated HFCCs of H$_1$ in R2^C-I and R2^C-II are in closest agreement with experiment, while R2^C-III and R2^C-IV give HFCCs for H$_3$ and, to a lesser degree, H$_4$ in closer agreement with experiment. For all four conformers, the calculated anisotropic HFCCs of each of the five hydrogens listed in Table 5.3 are in

close agreement with the corresponding experimental values. These results suggest that the experimentally observed radical is indeed the decarboxylated secondary radical cation. However, a more precise determination of the conformation is not possible. Explicit consideration of hydrogen bonding and other interactions between the radical cation and the crystalline environment are necessary for a more precise assignment. This is, however, beyond the scope of the methods employed in this study.

Table 5.3: Calculated, PWP86/6-311G(2d,p), HFCCs (MHz) of H_α, H_1, H_2, H_3 and H_4 in $R2^C$-I to $R2^C$-IV and the experimental values, and relative energies (kJ mol^{-1}).

tensor	HFCC	$R2^C$-I	$R2^C$-II	$R2^C$-III	$R2^C$-IV	exptl[a]
H_α	A_{iso}	-62.2	-61.2	-66.0	-66.7	-46.3
	T_{xx}	-39.0	-38.8	-39.2	-39.3	-35.0
	T_{yy}	-1.6	-1.6	-1.3	-1.4	0.2
	T_{zz}	40.6	40.4	40.5	40.7	34.8
H_1	A_{iso}	137.2	138.8	163.9	153.9	133.3
	T_{xx}	-6.0	-6.0	-6.1	-5.9	-6.3
	T_{yy}	-4.0	-4.1	-2.9	-3.4	-3.9
	T_{zz}	10.0	10.1	9.0	9.3	9.7
H_2	A_{iso}	78.7	84.1	77.4	77.4	45.9
	T_{xx}	-5.3	-5.5	-5.3	-5.4	-5.1
	T_{yy}	-2.9	-2.7	-3.8	-3.4	-2.6
	T_{zz}	8.2	8.3	9.1	8.7	7.7
H_3	A_{iso}	42.5	41.8	61.7	59.0	58.9
	T_{xx}	-5.8	-5.7	-5.8	-5.8	-5.4
	T_{yy}	-5.1	-5.1	-4.5	-4.7	-5.0
	T_{zz}	10.8	10.8	10.3	10.6	10.3
H_4	A_{iso}	94.1	94.3	82.9	85.9	72.6
	T_{xx}	-6.3	-6.2	-6.6	-6.5	-7.7
	T_{yy}	-4.3	-4.3	-4.8	-4.5	-4.5
	T_{zz}	10.5	10.5	11.3	11.0	12.3
ΔE^b		0.0	1.5	14.5	25.4	

[a]Ref 2. [b]B3LYP/6-311G(2df,p)//B3LYP/6-31+G(d,p) + ZPVE.

5.2.3 Radicals Formed upon Hydrogen Abstraction

The experimental observation of a single hydrogen HFCC of -54.1 MHz was assigned to the zwitterion of the radical formed upon hydrogen abstraction from the C_2 position: $R3^{Z}$.[2] In this present study, the optimized structure of $R3^{Z}$ was obtained using the Onsager model, with an estimated radius of 4.19 Å, and is illustrated schematically in Figure 5.4. $R3^{Z}$ contains a strong intramolecular $O_1 \cdots H_4-N$ hydrogen bond $(r_{O_1 \cdots H_4} = 1.762$ Å$)$. The $-C_3HOH-$ moiety forms the out-of-plane apex of the ring, causing the radical centre situated at the adjacent $-C_2-$ position to become quite pyramidal by approximately $16°$.

The calculated and experimentally observed HFCCs of H_α, H_1 and H_2 in $R3^{Z}$ are given in Table 5.4. For H_α the calculated and experimentally observed coupling constants are in close agreement. The calculated isotropic hyperfine couplings of the beta hydrogens H_1 and H_2 are 106.9 and 13.8 MHz, respectively. Experimentally, only one beta hydrogen coupling of approximately 98 MHz was observed and was suggested to arise from H_2, which is in fact close to the HFCC calculated for H_1. It is feasible that the second, considerably smaller, beta hydrogen coupling was too small to be observed. These results appear to support the assignment of the zwitterionic radical $R3^{Z}$ as the radical observed, however, a reversal of the assignment of the beta hydrogen HFFCs is suggested.

In addition, the neutral non-zwitterionic isomer of $R3^{Z}$, hereafter denoted as $R3^{N}$, was also investigated. Eight conformers of $R3^{N}$ were obtained and are shown

schematically in Figure 5.4. The major difference between each of the conformers is in

the orientation of the carboxylic group and the hydroxyl group at the C_3 position.
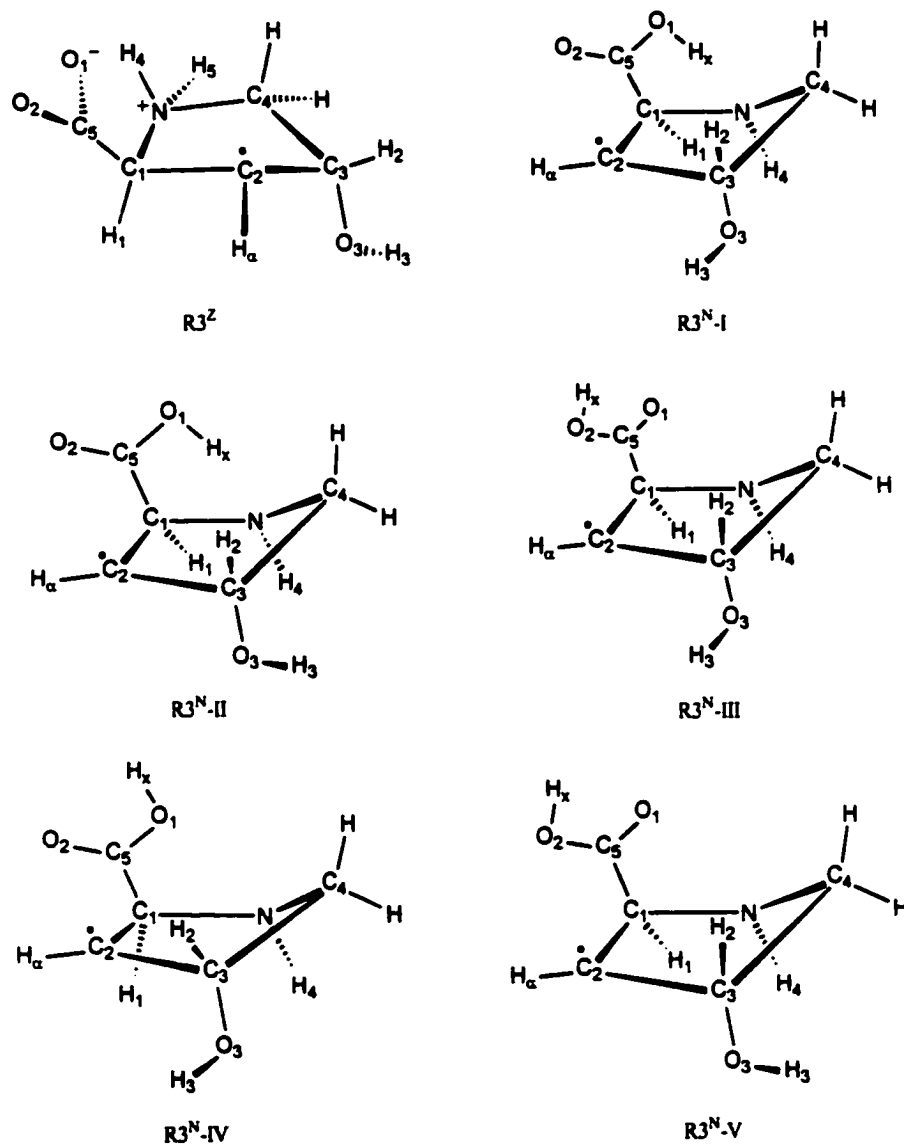
Figure 5.4 Optimized structures of $R3^Z$, and $R3^N$ (continued over page).
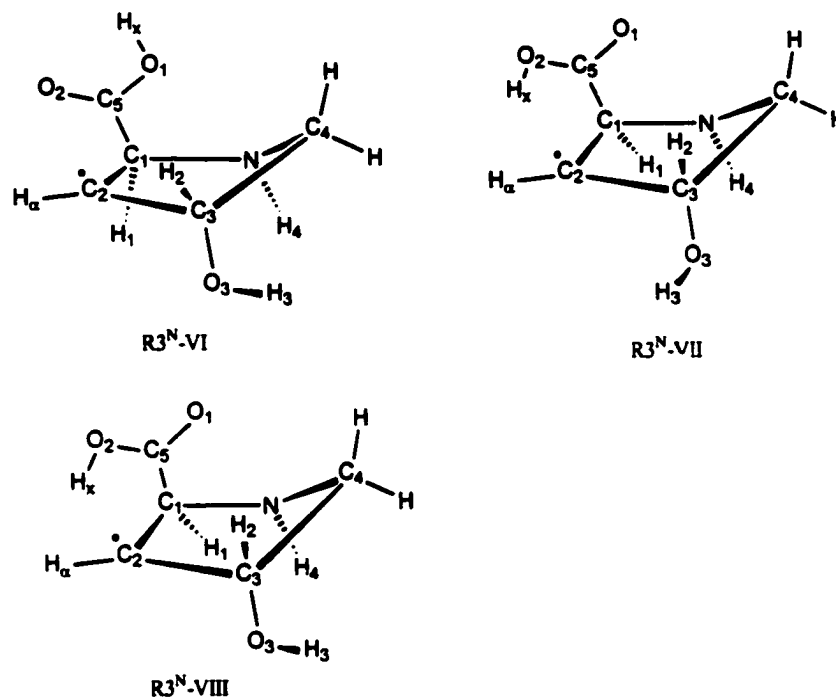
Figure 5.4 Optimized structures of $R3^Z$, and $R3^N$.

The calculated HFCCs of the eight conformers of $R3^N$ are shown in Table 5.4. The value of H_α is similar for all eight conformers. It can be clearly seen that the calculated H_1 and H_2 HFCCs of $R3^N$-III to $R3^N$-VIII differ significantly from the experimentally observed values. While the H_1 HFCC of $R3^N$-II is close to the experimentally observed value of 98.8 MHz, the H_2 HFCC of 30.2 MHz is too large to suggest that it may not have been experimentally observed. For $R3^N$-I, however, the H_1 HFCC is in close agreement with the beta coupling observed experimentally, while the H_2 HFCC is quite small. Indeed, the calculated isotropic HFCCs of $R3^N$-I are in closer agreement with the experimentally observed values than those of $R3^Z$. Thus, it is not possible to exclude $R3^N$-I as the observed radical, although the H_α anisotropic

components of R3^Z are in closer agreement with the experimental values than those of R3^N-I.

Table 5.4: Calculated, PWP86/6-311G(2d,p), and experimental HFCCs (MHz) of H$_\alpha$, H$_1$ H$_2$ in R3^Z and R3^N and relative energies (kJ mol^{-1}) of the conformers of R3^N.

Tensor	H$_\alpha$				H$_1$				H$_2$				ΔE[b]
	A$_{iso}$	T$_{xx}$	T$_{yy}$	T$_{zz}$	A$_{iso}$	T$_{xx}$	T$_{yy}$	T$_{zz}$	A$_{iso}$	T$_{xx}$	T$_{yy}$	T$_{zz}$	
R3^Z	-48.7	-32.3	-1.1	33.5	106.9	-3.9	-3.1	6.9	13.8	-5.4	-3.2	8.6	
R3^N-I	-57.6	-35.9	-0.2	36.0	98.8	-4.7	-3.4	8.1	12.6	-5.5	-3.1	8.6	0.0
R3^N-II	-58.0	-36.3	-0.7	37.1	100.6	-4.8	-3.4	8.2	30.2	-5.5	-3.5	9.0	8.8
R3^N-III	-58.0	-36.3	-0.2	36.5	82.8	-4.6	-3.3	7.9	19.9	-5.5	-2.9	8.4	14.7
R3^N-IV	-58.5	-36.7	-0.6	37.3	81.1	-4.5	-3.5	8.1	18.6	-5.6	-2.9	8.6	15.9
R3^N-V	-58.3	-36.7	-0.6	37.4	82.2	-4.7	-3.3	8.0	40.4	-5.5	-3.3	8.9	19.2
R3^N-VI	-59.5	-37.2	-1.1	38.3	80.5	-4.7	-3.5	8.2	39.4	-5.6	-3.4	9.0	21.1
R3^N-VII	-57.3	-36.1	-0.3	36.4	80.6	-4.3	-3.6	7.9	18.4	-5.4	-2.9	8.3	38.7
R3^N-VIII	-57.9	-36.6	-0.6	37.2	80.4	-4.4	-3.5	8.0	39.4	-5.4	-3.3	8.7	42.2
exptl[a]	-54.1	-31.6	0.4	31.4					98				

[a]Ref 2. [b]B3LYP/6-311G(2df,p)//B3LYP/6-31+G(d,p) + ZPVE.

Experimentally,[2] a radical was observed which possessed four beta hydrogen couplings. These were proposed as arising from a radical in which hydrogen abstraction from the C$_4$ position had occurred. In this present study, four possible conformers of the zwitterionic isomer of such a radical were found (R4^Z-I to R4^Z-IV) and are shown schematically in Figure 5.5. The structures were obtained using the Onsager model with an estimated radius of 4.30 Å. All four conformers contain a strong intramolecular O$_1$···H$_1$-N hydrogen bond (r$_{O···H}$<1.686 Å) and a radical centre that is pyramidal by approximately 18°. However, in R4^Z-I the -C$_4$- atom forms the apex of the five-membered ring, while in all other conformers the -C$_3$- radical centre forms the apex. In R4^Z-II the -C$_3$- radical centre can be considered as *trans* to the carboxyl group while it can be considered to be *cis* in R4^Z-III and R4^Z-IV.
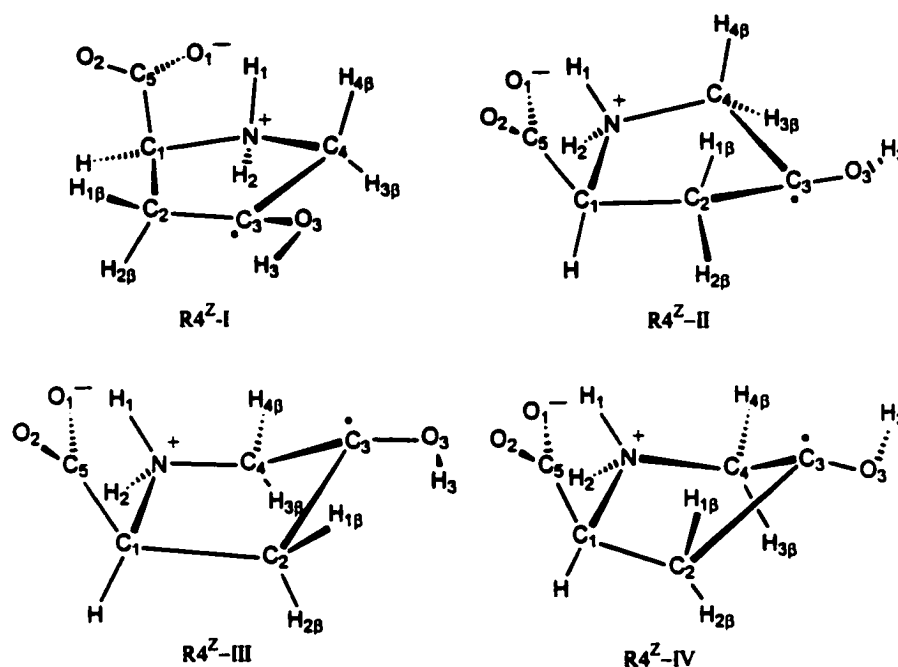
Figure 5.5 Optimized structures of R4^Z.

The calculated HFCCs of the four beta-hydrogens of the four conformers of R4^Z are listed in Table 5.5. The HFCCs for the four conformers differ significantly with ranges of 48.3, 44.4, 37.7 and 48.3 MHz for $H_{1\beta}$, $H_{2\beta}$, $H_{3\beta}$ and $H_{4\beta}$, respectively. This is due to the quite different orientations of the $-C_3{}^\bullet OH-$ moiety. The calculated HFCCs of R4^Z-I are in reasonable agreement with experiment, although the HFCC of $H_{2\beta}$ is still considerably lower than that observed experimentally. This difference is most likely due to the effects of the crystalline environment on the structure of the radical. A more detailed and explicit consideration of the effects of the environment, however, is beyond the scope of the methods employed in this present study.

Table 5.5: Calculated, PWP86/6-311G(2d,p), and experimental HFCCs (MHz) of R4^Z.

tensor	HFCC	R4^Z-I	R4^Z-II	R4^Z-III	R4^Z-IV	exptl[a]
H$_{1\beta}$	A$_{iso}$	89.0	98.1	49.8	54.3	89.8
	T$_{xx}$	-5.0	-4.2	-5.2	-5.0	-4.1
	T$_{yy}$	-2.1	-2.6	-4.1	-4.2	-2.5
	T$_{zz}$	7.0	6.8	9.2	9.3	6.5
H$_{2\beta}$	A$_{iso}$	62.4	49.9	94.3	92.8	85.6
	T$_{xx}$	-5.6	-4.9	-4.2	-4.2	-5.1
	T$_{yy}$	-4.4	-4.2	-3.1	-2.9	-4.6
	T$_{zz}$	10.1	9.2	7.4	7.1	9.9
H$_{3\beta}$	A$_{iso}$	53.2	51.7	84.1	89.4	62.5
	T$_{xx}$	-5.1	-5.5	-4.2	-4.4	-4.4
	T$_{yy}$	-4.0	-4.0	-3.5	-3.4	-3.2
	T$_{zz}$	9.1	9.5	7.7	7.8	11.3
H$_{4\beta}$	A$_{iso}$	95.3	87.7	53.3	47.0	101.4
	T$_{xx}$	-4.2	-4.6	-5.1	-5.4	-4.6
	T$_{yy}$	-2.9	-3.0	-4.0	-3.8	-1.6
	T$_{zz}$	7.2	7.6	9.1	9.2	

[a]Ref 2.

5.2.4 Secondary Radicals Formed upon Deamination

Hyperfine couplings of two radicals have been observed experimentally which have been assigned to different conformations of the radical formed upon deamination, R5. One conformation was observed at 77 K,[4] denoted as exptl I, while the second conformer was observed at 125 K,[4] denoted as exptl II. For temperatures intermediate between 77 and 125 K, a mixture of conformations was observed.[2] It was proposed that the conformational difference between exptl I and exptl II may simply be due to protonation of the carboxyl group -COO$^-$. However, no couplings of a carboxylic proton for the two conformations were observed. Thus, it was unclear whether R5 was in its anionic (R5^A) or neutral protonated (R5^N) form.

Two conformers, R5^A-I and R5^A-II, of the anionic form of R5 were obtained and are shown schematically in Figure 5.6. Both contain an intramolecular $O_1\cdots H_3$–N hydrogen bond ($r_{O\cdots H}$ = 2.151 and 2.240 Å, respectively). The corresponding calculated HFCCs are listed in Table 5.6. The considerable differences between the calculated and experimentally observed HFCCs, particularly for H_1, clearly indicate that the observed radicals are not different conformers of the anionic form of R5.
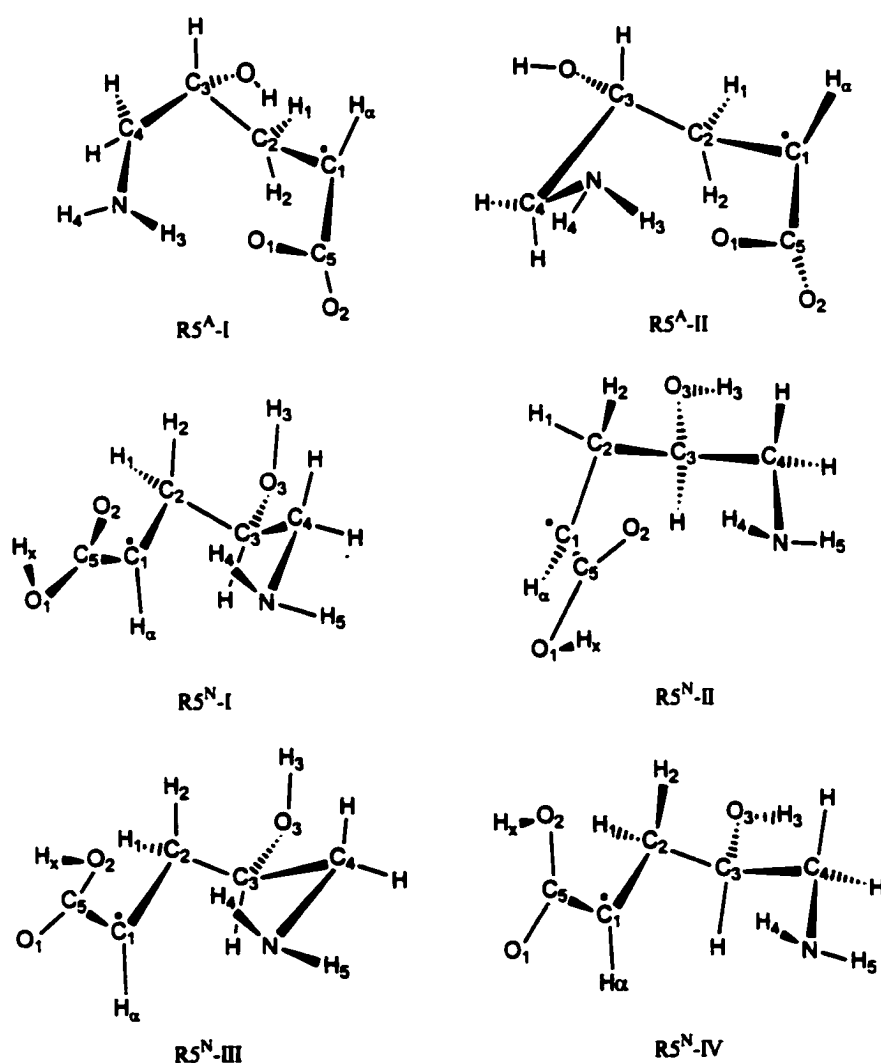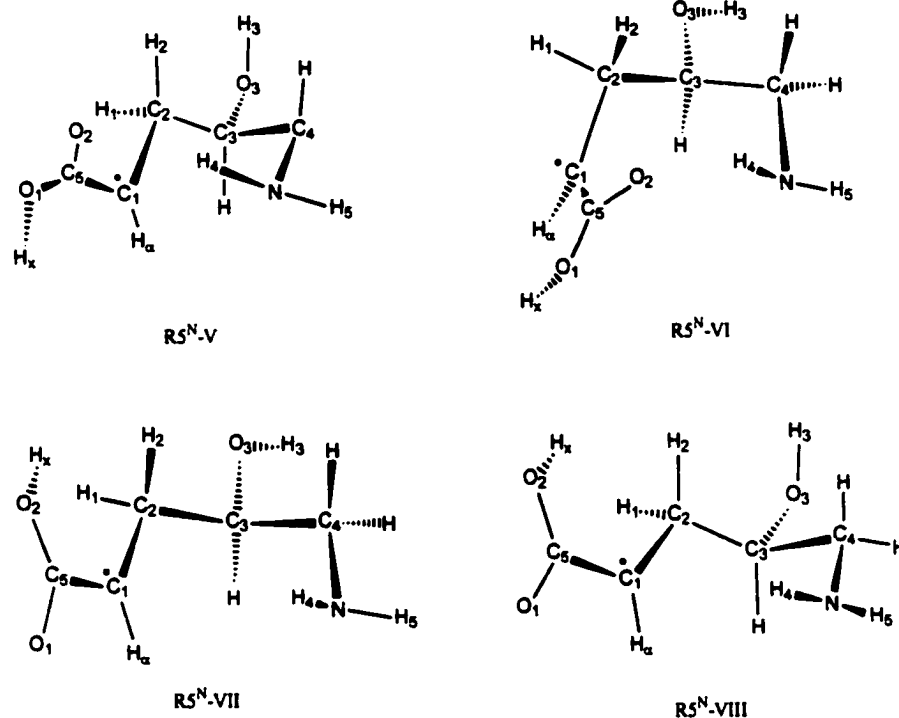

Figure 5.6 Optimized structures of R5^A and R5^N (continued over page).

Figure 5.6 Optimized structures of RS^A and RS^N.

Table 5.6: Calculated, PWP86/6-311G(2d,p), and experimental HFCCs (MHz) of RS^A and RS^N, and relative energies (kJ mol^{-1}) of the conformers of RS^N.

system	H$_\alpha$				H$_1$				H$_2$				ΔE^b
	A$_{iso}$	T$_{xx}$	T$_{yy}$	T$_{zz}$	A$_{iso}$	T$_{xx}$	T$_{yy}$	T$_{zz}$	A$_{iso}$	T$_{xx}$	T$_{yy}$	T$_{zz}$	
RS^A-I	-44.2	-32.5	-1.3	33.8	57.8	-4.2	-4.0	8.2	9.1	-4.4	-4.0	8.5	0.0
RS^A-II	-40.9	-32.2	-1.3	33.5	60.1	-4.2	-4.0	8.2	8.8	-4.3	-3.8	8.1	7.4
RS^N-I	-47.5	-29.8	-1.9	31.6	72.4	-4.4	-3.2	7.6	3.7	-3.7	-2.8	6.5	0.0
RS^N-II	-49.0	-30.6	-1.9	32.6	79.1	-4.6	-3.2	7.8	3.3	-4.0	-2.8	6.8	2.1
RS^N-III	-47.0	-28.9	-2.3	31.2	78.3	-4.4	-3.2	7.6	2.5	-3.4	-3.3	6.7	7.2
RS^N-IV	-50.9	-30.5	-2.2	32.7	139.5	-5.4	-2.5	7.9	22.2	-3.9	-3.2	7.1	10.7
RS^N-V	-46.3	-29.8	-1.5	31.3	71.6	-4.4	-3.1	7.5	3.5	-3.7	-2.7	6.4	19.6
RS^N-VI	-47.5	-30.6	-1.6	32.2	80.2	-4.6	-3.1	7.7	2.9	-3.8	-2.8	6.7	22.2
RS^N-VII	-52.8	-30.8	-1.9	32.7	136.8	-5.2	-2.5	7.7	34.1	-3.9	-3.3	7.3	34.8
RS^N-VIII	-50.5	-30.4	-2.5	32.9	130.6	-5.1	-2.6	7.7	21.4	-3.7	-3.3	7.1	37.7
exptl I^a	-57.2	-32.4	1.9	30.6	78.0	-4.8	-3.4	8.3					
exptl II^a	-56.5	-32.4	1.3	31.1	123.1	-5.1	-2.2	7.4	21.4	-4.3	-3.2	7.6	

^{a}Ref 4. ^{b}B3LYP/6-311G(2df,p)//B3LYP/6-31+G(d,p) + ZPVE

For the neutral protonated form of R5, eight possible conformers ($R5^N$-I to $R5^N$-VIII) were obtained and are shown schematically in Figure 5.6. The conformers may be divided into two groups depending on whether or not they contain an intramolecular hydrogen bond between the carboxylic group and the $-NH_2$ moiety. The conformers $R5^N$-I, $R5^N$-II, $R5^N$-III, $R5^N$-V and $R5^N$-VI, hereafter referred to as group I, contain a slightly shortened hydrogen bond between O_2 of the carboxylic group and H_4 of the $-NH_2$ moiety (2.316 Å< $r_{O\cdots H}$ <2.431 Å). The conformers $R5^N$-IV, $R5^N$-VII and $R5^N$-VIII, hereafter referred to as group II, contain no such hydrogen bond ($r_{O\cdots H}$ >3.661 Å). Consequently, the structures of group II conformers are more open than those of group I.

As can be seen in Table 5.6, these differences in the structures are also reflected in the calculated HFCCs. For the conformers in group I, the calculated H_α, H_1 and H_2 HFCCs are all grouped in the approximate ranges of -46 to -49, 70 to 80 and 2 to 4 MHz, respectively. These coupling constants are in close agreement with those experimentally observed at 77 K, i.e., exptl I. The small calculated coupling constants of H_2 support the experimental postulation that the second beta-hydrogen coupling may have been too small to have been observed. The calculated HFCCs of the group I conformers are very similar to each other. Thus, it is not possible to determine if exptl I is due to one conformer or a mixture of the group I conformers. For conformers in group II, the H_α, H_1 and H_2 HFCCs are all grouped in the approximate ranges of -50 to -53, 130 to 140 and 21 to 34 MHz, respectively. These coupling constants are in good agreement with the conformer observed at 125 K, i.e., exptl II, with those of $R5^N$-VIII in closest agreement. These results suggest that the major difference between the two

experimentally observed conformers is the presence of intramolecular hydrogen bonding at lower temperatures.

5.3 Conclusions

The structures and HFCCs of possible experimentally observed hydroxyproline-derived radicals have been investigated using density functional theory. The calculated HFCCs have been compared with experimental values.

For the radical anion of hydroxyproline ($R1^A$), the zwitterionic isomer ($R1^Z$) was obtained using the Onsager model. The calculated isotropic H_β HFCC of $R1^Z$ differs significantly from the two experimentally observed values and previously assigned to different conformations of $R1^Z$. Thus, it is unlikely that either of the conformations observed is the zwitterion $R1^Z$. Four possible conformations of the non-zwitterionic form of the radical were also found. Of these, the isotropic and anisotropic H_β HFCCs of two possible conformations, $R1^A$-II and $R1^A$-III, are found to be in good agreement with one of the experimentally observed radicals. The second H_β HFCC observed experimentally is found to agree closely with the H_β HFCCs calculated for four possible conformations of the protonated derivative of the radical anion, $R1^P$, in which the carboxylic group has been protonated. On the basis of these results, the two radicals observed, and previously assigned as different conformations of the zwitterion of the primary radical anion, are concluded to be a non-zwitterionic conformer of the primary radical anion and a derivative in which the carboxylic group has been protonated.

Four possible conformers of the secondary radical cation ($R2^C$) formed by decarboxylation of hydroxyproline were obtained. The calculated HFCCs of the four conformers support the experimental assignment, however, none completely accounts for the experimentally observed values. This is most likely due to interactions between the radical and the crystalline environment, i.e., intermolecular hydrogen bond formation and crystal packing effects, affecting the experimental values. The exact effect on the HFCCs is unclear. Thus, a precise determination of the conformation of the observed radical is not possible without including specific interactions between the radical and the crystalline environment. This is not feasible for the methods employed in this present study.

Several possible conformers for radical zwitterions formed by hydrogen abstraction from the C_2 or C_3 position of the five-membered ring were obtained. The calculated HFCCs for the zwitterionic radical formed by hydrogen abstraction from the C_2 position, $R3^Z$, are in good agreement with the experimental values. However, a neutral non-zwitterionic conformer, $R4^N$-I, also gives HFCCs in close agreement with the experimental values. Thus, it is impossible to determine whether or not the radical observed is the zwitterion. Four conformers, $R4^Z$-I, $R4^Z$-II and $R4^Z$-III, $R4^Z$-IV, for the radical zwitterion formed by hydrogen abstraction from the C_3 position were obtained. The HFCCs of all conformers are found to be dependent on the orientation of the − $C_3{}^\bullet OH−$ moiety. The calculated HFCCs of $R4^Z$-I are in closest agreement with experiment. Thus, it is concluded that the radical observed is $R4^Z$, as previously assigned, and that it possesses a conformation similar to that of $R4^Z$-I.

Two possible conformations of the radical anion formed on deamination were obtained. The calculated HFCCs of both conformers are quite similar, however, they differ significantly from the experimentally observed values. Eight possible conformations of the neutral radical, $R5^N$, formed on protonation of the carboxyl group of the radical anion, were obtained. The conformers can be divided into two groups; those that contain an intramolecular hydrogen bond between the carboxylic group and the amino group, and those that do not. The calculated HFCCs of those conformers containing such an intramolecular hydrogen bond ($R5^N$-I, $R5^N$-II, $R5^N$-III, $R5^N$-V and $R5^N$-VI) are in reasonable agreement with each other and are in good agreement with the experimental values observed at 77 K. The calculated HFCCs of those conformers not containing such an intramolecular hydrogen bond ($R5^N$-IV, $R5^N$-VII and $R5^N$-VIII) are also similar to each other, but differ significantly from those which do contain such a bond. However, they are in close agreement with the experimental values observed at 125 K, with those of conformer $R5^N$-VIII in closest agreement. On the basis of these assignments, the change in HFCCs observed on going from 77 K to 125 K is due to the breaking of the intramolecular carboxyl-amino hydrogen bond resulting in a more open structure.

References

1. Box, H. C. *Radiation Effects, ESR and ENDOR Analysis*, Academic Press: New York, 1977.

2. Nelson, W. H. *J. Phys. Chem.* **1988**, *92*, 554.

3. Nelson, W. H.; Carpenter, P. K. _J. Chem. Phys._ **1985**, _83_, 2153.

4. Nelson, W. H.; Nave, C. R. _J. Chem. Phys._ **1981**, _74_, 2710.

5. Nelson, W. H.; Talor, D. R. _J. Chem. Phys._ **1980**, _72_, 524.

6. Ko, C. -L.; Box, H. C. _J. Chem. Phys._ **1978**, _68_, 5357.

7. Eriksson, L. A. _Mol. Phys._ **1997**, _91_, 827.

8. Rega, N.; Cossi, M.; Barone, V. _J. Am. Chem. Soc._ **1998**, _120_, 5723.

9. Ban, F.; Gauld, J. W.; Boyd, R. J. _J. Phys. Chem._ A **2000**, _104_, 5080.

10. Ban, F.; Wetmore, S. D.; Boyd, R. J. _J. Phys. Chem._ A **1999**, _103_, 4303.

11. Lahorte, P.; Proft, F. D.; Vanhaelewyn, G.; Masschaele, B.; Cauwels, P.; Callens, F.; Geerings, P.; Mondelaers, W. _J. Phys. Chem._ A **1999**, _33_, 6650.

12. Himo, F.; Gräslund, A.; Eriksson, L. A. _Biophys. J._ **1997**, _72_, 1556.

13. Himo, F.; Eriksson, L. A. _J. Phys. Chem._ B **1997**, _101_, 9811.

14. Lassmann, G.; Eriksson, L. A.; Himo, F.; Lendzian, F.; Lubitz, W. _J. Phys. Chem._ A **1999**, _103_, 3745.

15. Himo, F.; Tabcock, G. T.; Eriksson, L. A. _J. Phys. Chem._ A **1999**, _103_, 3745.

16. O'Malley, P. J. _J. Phys. Chem._ A **1998**, _102_, 248.

17. (a) Wetmore, S. D.; Boyd, R. J.; Eriksson, L. A. _J. Phys. Chem._ B **1998**, _102_, 5369. (b) Wetmore, S. D.; Himo, F.; Boyd, R. J.; Eriksson, L. A. _J. Phys. Chem._ B **1998**, _102_, 7484. (c) Wetmore, S. D.; Boyd, R. J.; Eriksson, L. A. _J. Phys. Chem._ B **1998**, _102_, 7674. (d) Wetmore, S. D.; Boyd, R. J.; Eriksson, L. A. _J. Phys. Chem._ B **1998**, _102_, 9332. (e) Wetmore, S. D.; Boyd, R. J.; Eriksson, L. A. _J. Phys. Chem._ B **1998**, _102_, 10602.

18. Ding, Y.; Krogh-Jespersen, K. _Chem. Phys. Lett._ **1992**, _199_, 261.

19. Barone, V.; Adamo, C.; Grand, A.; Subra, R. *Chem. Phys. Lett.* **1995**, *242*, 351.

20. Ban, F.; Gauld, J. W.; Boyd, R. J. *J. Phys. Chem.* A **2000**, *104*, 8358.

The Cross-linking Mechanisms between Cytosine and Tyrosine

6.1 Introduction

Reactive-oxygen-species (ROS) mediated oxidative stress,[1] which is a disturbance in the oxidant-antioxidant balance in favour of the former, contributes to numerous pathological conditions among which cancer,[2-6] Alzheimer's[7,8] and Parkinson's[9] diseases are major problems. Common ROS include singlet oxygen $^1O_2$, hydrogen peroxide H_2O_2, superoxide anion $O_2^{\bullet -}$, hydroxyl radical $^\bullet OH$ and hydroperoxyl radical $HOO^\bullet$. Of these, $^\bullet OH$ is thought to be the most damaging.[10,11] Abstraction of hydrogen atoms by $^\bullet OH$ from, or addition of $^\bullet OH$ to DNA bases, sugars and amino acid residues of proteins produces huge numbers of secondary radicals. There can be up to 10^3 oxidative damaging events upon the DNA of each cell in the human body everyday.[12] Extensive experimental studies discovered that the interaction of the $^\bullet OH$ radicals with DNA bases results in a diversity of adducts of purines and pyrimidines.[13-15] Tandem base lesions within isolated DNA are also mediated by $^\bullet OH$.[16,17]
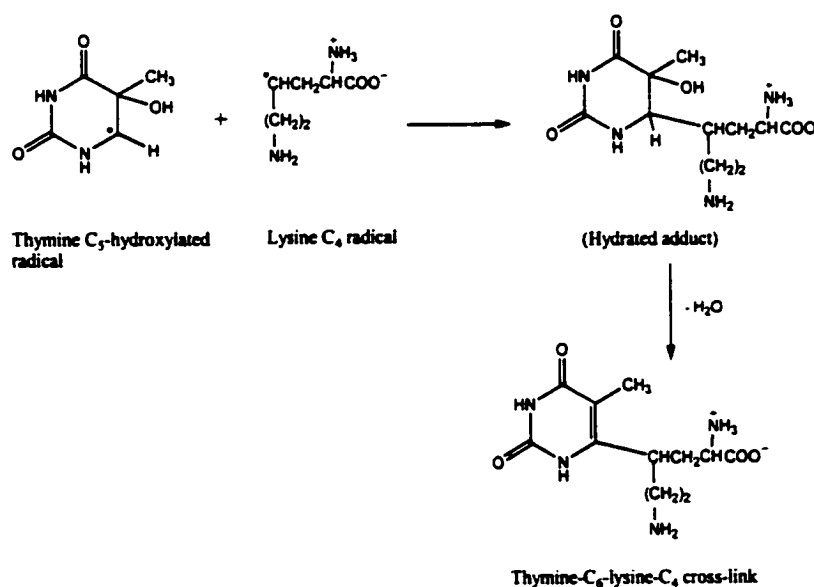
The biological importance of oxidative damage to proteins has been considerably less studied.[1] One reason for this, is that the research on protein radicals primarily has focused on their formation and functionality in enzymatic catalysis.[18] For instance, it is commonly known that the tyrosyl radicals play important roles as reactive storage sites or metastable intermediates in a number of enzymes including ribonucleotide reductase,[19] photosystem II,[20,21] while little is known about its damaging effect. However, recent research on proteins[22-27] has revealed that the actions of ROS on protein may lead to significant damage via hydrogen abstraction.

In particular, the formation of tyrosyl radicals has been recognized as one typical feature of oxidative stress.[22,23] Further tyrosyl radical mediated damage includes the formation of protein cross-links[28] via dityrosine and trityrosine, which possibly can serve as a marker for tyrosyl radical-mediated oxidative damage in atherosclerosis and other inflammatory conditions.

As DNA bases and proteins inside the nucleus are attacked by reactive oxygen species, the resulting protein radicals and DNA radicals may give rise to DNA-protein cross-links. In this aspect, radiation biology[13] is well established to probe the oxidative effect of hydroxyl radicals. Ionizing radiation is known to be both mutagenetic and carcinogenic.[1] Much of the cell damage caused by ionizing radiation involves the formation of $^{\bullet}OH$ radicals. It has been shown that ionizing radiation produces DNA-protein cross-links in living cells and isolated chromatin,[29-31] which may cause serious problems in DNA replication. Even though great effort has been devoted to elucidating

the mechanisms of DNA lesions and protein damage, the coupled reactions involving biological radical intermediates are poorly understood.

The cross-link structures[32-38] of pyrimidine bases and various amino acids in aqueous model systems have been characterized via GC-MS techniques. In particlar, hydroxyl radical induced cross-linking of cytosine with tyrosine,[34] thymine with tyrosine[36] and thymine with lysine[32] have been studied in detail. For the thymine + lysine system, the direct radical recombination reaction (Scheme 6.1) has been characterized as the major reaction mechanism that leads to the cross-link.[32,35] For the cytosine + tyrosine or the thymine + tyrosine system, however, the molecular steps by which the *OH radical induces the DNA-protein cross-links are still unclear. Several possible mechanisms based on the identified final products have been hypothesized.[34,36,38]

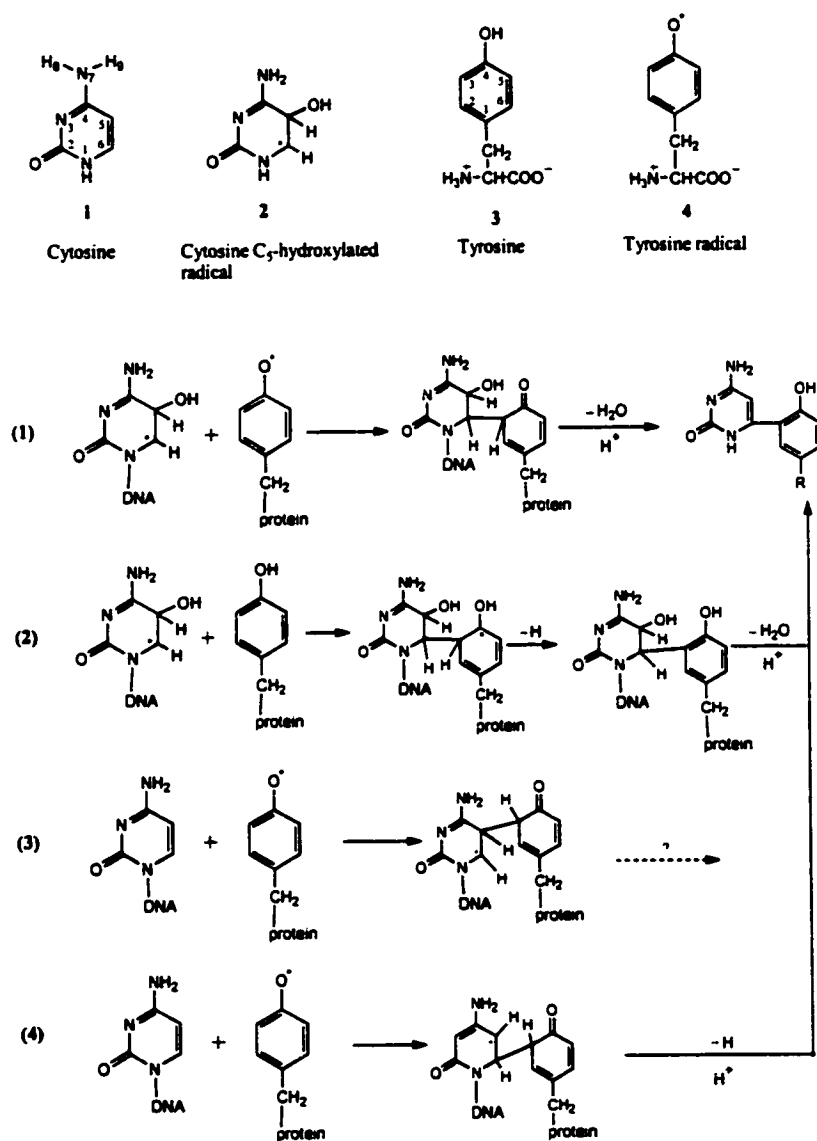

Thymine C5-hydroxylated radical   Lysine C4 radical   (Hydrated adduct)

Thymine-C6-lysine-C4 cross-link

Scheme 6.1 Schematic illustration of the radical combination mechanism for the cross-link of thymine and lysine.[36]

In this chapter, theoretical investigation is focused on the reaction mechanisms of cytosine and tyrosine upon irradiation. Gajewski and Dizdaroglu[34] reported that a DNA-protein cross-link of cytosine (Cyt) and tyrosine (Tyr) moieties forms in a nucleohistone when exposed to γ-irradiation. The cross-link was proposed to involve formation of a covalent bond between C_6 of cytosine and C_3 of tyrosine (the numbering of the atoms of cytosine and tyrosine is shown in Scheme 6.2). Moreover, it has been shown[38] that the Cyt-Tyr cross-link in the nucleohistone is identical to the cross-link observed in the model experiments of the γ-irradiated aqueous solution of cytosine and tyrosine. Thus, free cytosine and tyrosine (phenol) have been used to investigate the mechanisms for the relevant cross-link in these systems.

It has been found[39] that the $^{\bullet}OH$ adds to the $C_5=C_6$ of cytosine with a preference at C_5 (see 2 in scheme 6.2) to the extent of 87%. In addition, tyrosyl radical[40,41] (4 in Scheme 6.2) has been found to be the major radical resulting from the reaction of tyrosine with the hydroxyl radical. Thus, the neutral cytosine, tyrosine, cytosine C_5-hydroxylated radical and tyrosyl radical moieties are most likely the reactants that generate the Cyt-Tyr cross-link in the nucleohistone. Hence, the cross-linking mechanisms were proposed[34] as schematically shown in Scheme 6.2: (1) the combination of cytosine C_5-hydroxylated radical and tyrosyl radical; (2) the addition of cytosine C_5-hydroxylated radical to tyrosine; (3) the addition of the tyrosyl radical to C_5 of cytosine and (4) the addition of the tyrosyl radical to C_6 of cytosine. The last two mechanisms were suggested to be the addition of tyrosyl radical 4 to the $C_5=C_6$ double bond of cytosine 1.[34] Although only the radical combination mechanism was suggested to account for the formation of the cross-

link in the aqueous vitro system, the radical addition mechanisms have not been eliminated. In each of the above mechanisms, the final cross-link is formed through several steps of reaction. As such it is very important to examine the feasibility of every step of the reaction in each mechanism.

Scheme 6.2 Schematic illustration of the four investigated cross-linking mechanisms of cytosine, tyrosine, cytosine C$_5$-hydroxylated radical and tyrosyl radical in a nucleohistone.

Computationally, density functional theory (DFT) methods have been tested extensively against other accurate correlated methods for prediction of reliable geometries[42] and reaction barriers.[43] The reliability and efficiency of DFT methods offers an attractive theoretical approach to gaining insight into large biological systems.[44,45] In particular, the paramagnetic properties of numerous biological radicals derived from the DNA bases,[46a-d] sugars[46e,47] and amino acids[48a-h] have been extensively studied using density functional theory, and the reaction mechanisms of hydroxyl radical with imidazole, tyrosine, pyrimidine and purine bases have been investigated using B3LYP methods, Hartree-Fock (HF) and MP2 methods.[49a-c] The unrestricted Hartree-Fock (UHF) and MP2 methods were suggested to suffer from severe spin contamination for radicals, whereas the B3LYP method was shown to be able to suitably describe the potential energy surfaces although it may have problems in locating transition structures in cases where the reaction barrier is very small.[49c]

Since it has been reported that calculated structures and spin density distributions of phenoxyl radical and tyrosine side chain phenoxyl radical are essentially the same,[50] the tyrosine and tyrosyl radical are modelled by phenol, 5, and phenoxyl radical, 6, (see Figure 6.1a) in the present study[51] in order to reduce computational requirements.

6.2 Computational Methods

All geometry optimizations were performed with the B3LYP hybrid density functional (Chapter 2) in conjunction with the 6-31G(d,p) basis set using the GAUSSIAN 98 suite of programs. Harmonic vibrational frequencies and zero-point

vibrational energies (ZPVEs) were obtained at the same level of theory. Relative

energies were obtained by performing single point calculations at the B3LYP level in

conjunction with the 6-311G(2df,p) basis set using the above optimized geometries and

by including the zero-point vibrational energy i.e., B3LYP/6-311G(2df,p)//B3LYP/6-

31G(d,p) + ZPVE.

The solvent effect on the cross-linking mechanisms was investigated by single

point calculations at the B3LYP/6-311G(2df,p) level on the optimized gas phase

structures using the polarizable continuum model (PCM)[52a-c] with a dielectric constant

78.39 for H_2O. For all open- and closed-shell systems, the unrestricted (UB3LYP) and

restricted (RB3LYP) B3LYP procedures have been used, respectively. The symbols U

and R have been neglected for simplicity. All energies are in kJ mol^{-1} and bond lengths in

angstroms (Å), unless otherwise specified. For the dimeric systems, a prime (') has been

used to denote atoms originally on the tyrosine (phenol) moiety.

6.3 Results and Discussion

6.3.1 The Reactivity of the Reactants

The optimized structures of cytosine 1, Cyt-C$_5$OH$^\bullet$ radical 2, phenol 5 and

phenoxyl radical 6 are schematically shown in Figure 6.1a. Mulliken charges on the

heavy atoms of 1, 2, 5 and 6 and the atomic spin densities larger than 0.10 of the radicals

2 and 6, as calculated at the B3LYP/6-311G(2df,p)//B3LYP/6-31G(d,p) level of theory,

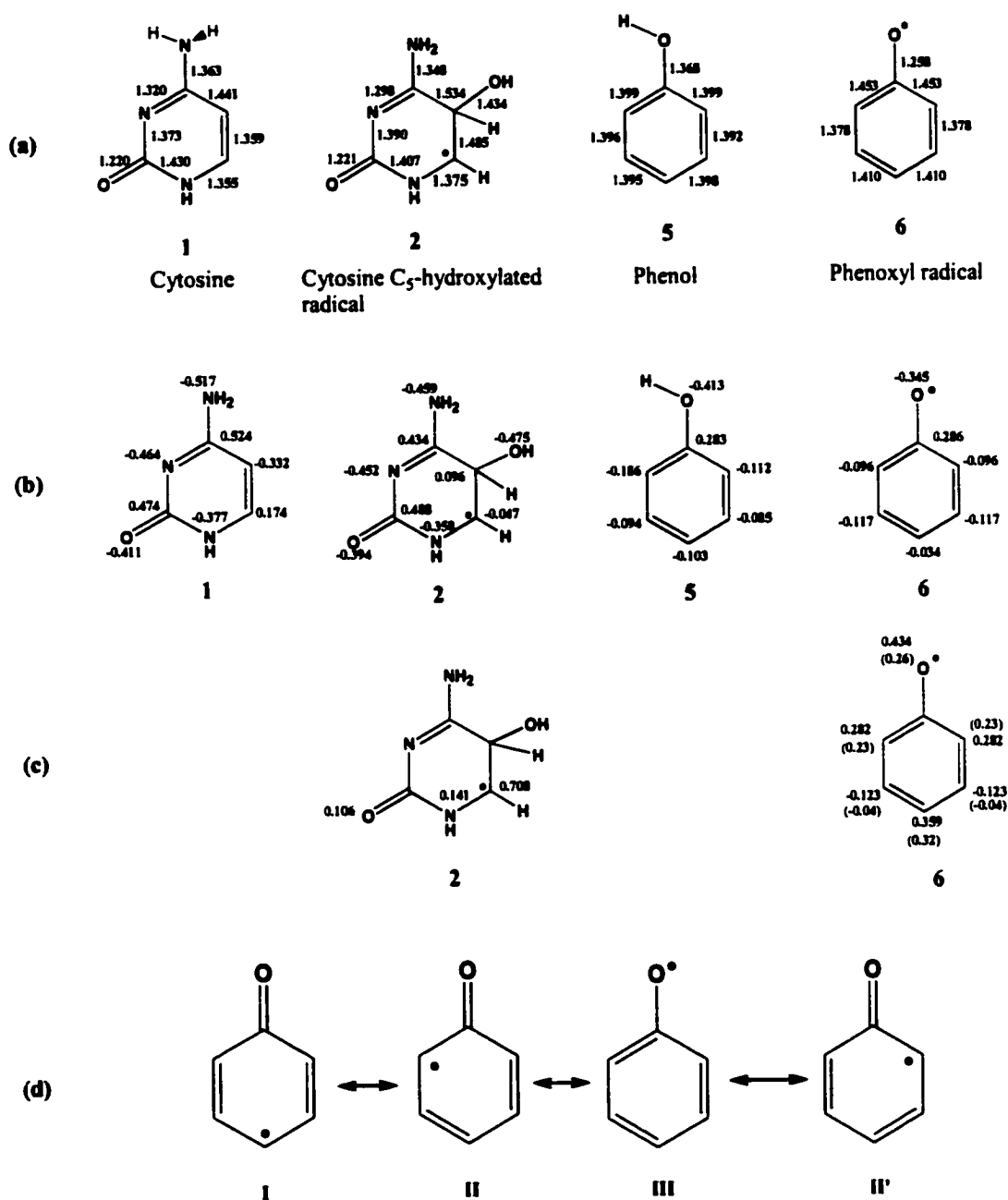are shown in Figures 6.1b and 6.1c, respectively.

Figure 6.1 (a) Optimized structures (bond lengths) of cytosine 1, C₅-hydroxylated radical 2, phenol 5 and

phenoxyl radical 6. (b) Mulliken charges on the heavy atoms of cytosine, C₅-hydroxylated radical, phenol

and phenxoyl radical. (c) Spin density distribution (only absolute values at the atoms larger than 0.10 are

shown) of C₅-hydroxylated radical and phenxoyl radical. Values in parentheses: experimental estimates,

ref 59. (d) Possible resonance structures of the phenoxyl radical.

The skeletal structure of cytosine is approximately planar. However, the amino group of cytosine is pyramidal by approximately $25°$ ($\angle H_8N_7C_4H_9=154.7°$). Even if the cytosine-ring shows a normal π-conjugated pattern, the C_5—C_6 bond (1.359 Å) has a localized double bond character, being much shorter than C—C bond of benzene (1.396 Å).[53] Furthermore, it is noted that the charge at C_5 is negative (-0.332), while at C_6 it is positive (+0.174). This particular charge distribution is associated with the position of the heteroatoms within the cytosine molecule. Since the addition of $^•$OH to a polarizable double bond has remarkable selectivity towards an electron rich center,[54ab] the difference of the charge at C_5 and C_6 explains why the $^•$OH addition to the cytosine C_5 dominates the reaction.[39]

The Cyt-C_5OH$^•$ radical 2 has a half-chair conformation on the six-membered ring with C_5 being the chair-back. The formation of the tetrahedral C_5 centre in 2 weakens the N_1—C_6 and C_2—N_3 double bond character by lengthening these bonds, but enhances the N_1—C_2 and N_3—C_4 double bond content by shortening the bonds. As a consequence, C_6 is pyramidal by $23°$ and becomes a localized radical centre with spin density of approximately 0.708.

The phenol 5 is a planar molecule. The C—C bond distances suggest that the benzene moiety is π-conjugated. It is interesting to note that the *ortho-* C_3 and C_5 have larger negative Mulliken charges than the other carbons of the ring. Hence, the electrophilic addition of Cyt-C_5OH$^•$ radical 2 to phenol is suggested to occur on the *ortho*-carbon sites as proposed in mechanism 2 (see Scheme 6.2). The preference for

addition to C_3/C_5 has also been noted in the case of direct $^\bullet OH$ radical attack on tyrosine.[40,49a,55]

The structure of phenoxyl radical **6** resembles that obtained by Chipman et al.[56] at the CASSCF/6-311G(2d,p) level of theory. The main geometrical changes from phenol **5** to phenoxyl radical **6** are the shortening of the C_4—O, C_2—C_3 and C_5—C_6 bonds and the elongation of the C_1—C_2, C_3—C_4, C_4—C_5 and C_1—C_6 bonds. The C_4—O bond length of 1.258 Å is much closer to the $C{=}O$ double bond of 1.225 Å observed for p-benzoquinone[57] than the calculated phenol C—O single bond length of 1.368 Å or the reported value of 1.381 Å from an electron diffraction measurement.[58]

The calculated spin densities are in fair agreement with the experimental values, shown in parentheses in Figure 6.1c. The calculated spin density at the oxygen is approximately 0.434, while the experimental estimate is 0.26.[59] The large discrepancy between the values has also been noted earlier,[49d] and shown to arise primarily from an erroneous empirical value employed in the McConnell relation used to convert measured hyperfine parameters into spin densities. From either the calculated spin density distribution or the experimental data, it is however clear that most of the unpaired electron is delocalized on the benzene ring. This agrees with the resonance structures of the radical, displayed in Figure 6.1d. Since the C_1 site is blocked in the tyrosyl radical (see **4** in Scheme 6.2), the equivalent C_3 or C_5 positions are the most likely reactive sites. This conclusion supports the proposal[38] that the cross-linking site is predominantly on the C_3 (C_5) carbon.

## 6.3.2 The Initial Step of the Cross-linking Mechanisms

The four mechanisms shown in Scheme 6.2 are considered as competitive reaction paths in the present study. The feasibility of the initial step of each reaction mechanism may determine its fate. Thus, the potential energy surfaces for the initial step of each reaction mechanism are investigated.

The energy profile for the direct combination of Cyt-C$_5$OH$^\bullet$ radical **2** and phenoxyl radical **6** is schematically shown in Figure 6.2a. All attempts to locate a transition structure (TS) for the formation of **1a**, including scans of the singlet and triplet energy surfaces, were unsuccessful. The radical combination forming the product **1a** is found to be energetically favourable by 157.0 kJ mol^{-1}.

The energy profile for the addition of the Cyt-C$_5$OH$^\bullet$ radical, **2**, to the phenol, **5**, is schematically shown in Figure 6.2b. The Cyt-C$_5$OH$^\bullet$ radical initially interacts with the phenol forming a hydrogen-bonded complex **2a**, lying 10.1 kJ mol^{-1} lower in energy. The hydrogen-bonding distance between the —OH group of Cyt-C$_5$OH$^\bullet$ radical and the oxygen of phenol is approximately 1.913 Å. The cross-linked product **2c** is formed via TS **2b** with an activation barrier of 74.6 kJ mol^{-1}. In **2b**, the distance between the C$_6$ of Cyt-C$_5$OH$^\bullet$ radical and the C$_3'$ of phenol is approximately 2.096 Å and the —OH group of the cytosine moiety interacts with the oxygen of phenol at a shorter distance of 1.882 Å. Interestingly, despite the even stronger hydrogen-bond (1.822 Å) in the product **2c**, this lies more than 27 kJ mol^{-1} higher in energy than the isolated reactants.
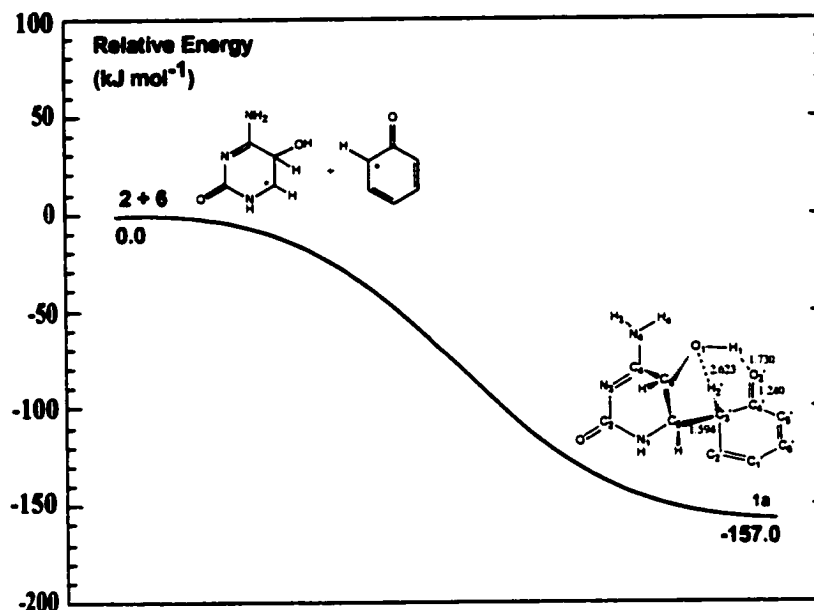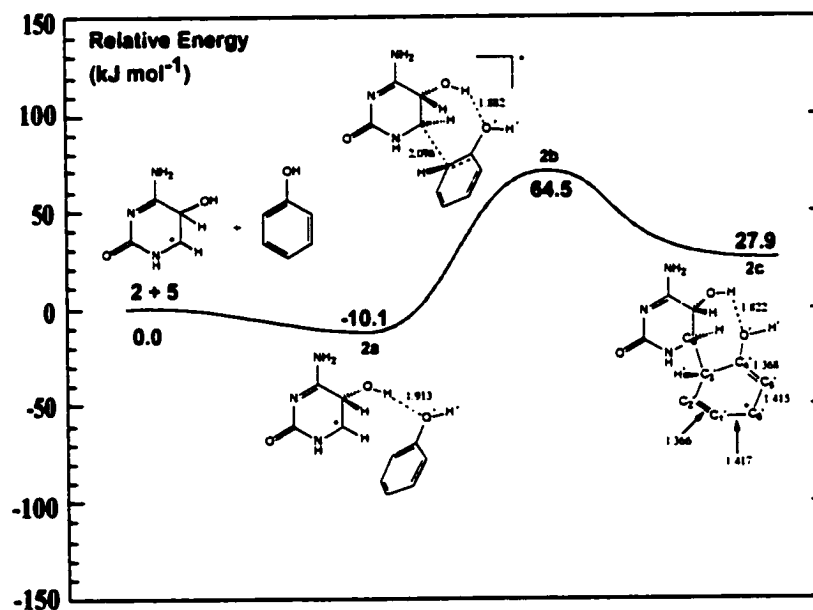
Figure 6.2 Schematic energy profiles for the initial reaction step (a) mechanism 1 (2 + 6), (b) mechanism 2 (2 + 5), (c) mechanism 3 (1 + 6) addition to C₅ of cytosine, (d) mechanism 4 (1 + 6) addition to C₆ of cytosine, (e) summary of mechanisms 1, 2, 3 and 4 in the gas phase, (f) summary of mechanisms 1, 2, 3 and 4 showing the effects of solvent, by inclusion of the PCM model. (continued over page)
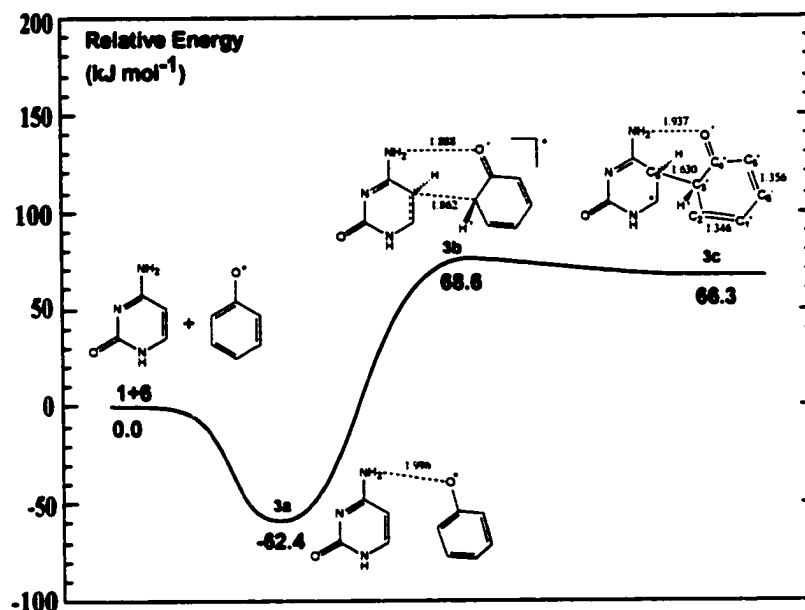
c

d

Figure 6.2 Schematic energy profiles for the initial reaction step (a) mechanism 1 (2 + 6), (b) mechanism 2 (2 + 5), (c) mechanism 3 (1 + 6) addition to C_5 of cytosine, (d) mechanism 4 (1 + 6) addition to C_6 of cytosine, (e) summary of mechanisms 1, 2, 3 and 4 in the gas phase, (f) summary of mechanisms 1, 2, 3 and 4 showing the effects of solvent, by inclusion of the PCM model. (continued over page)
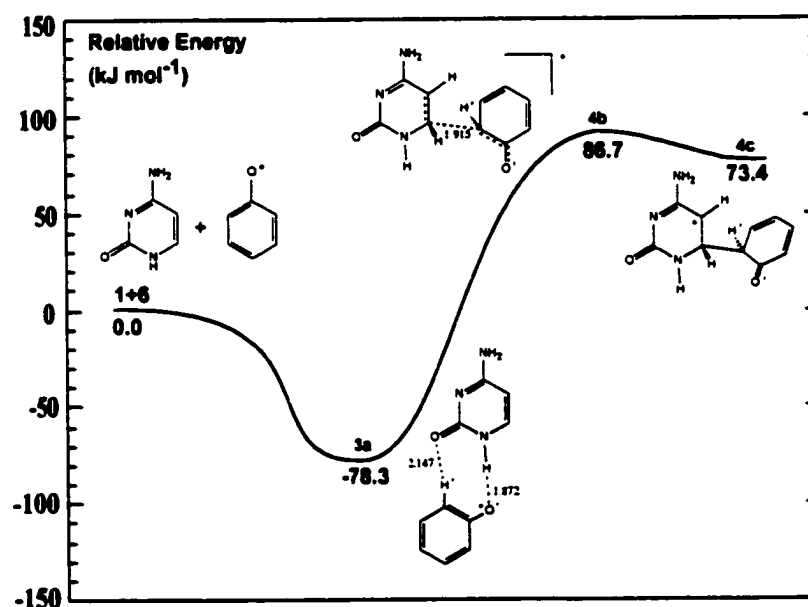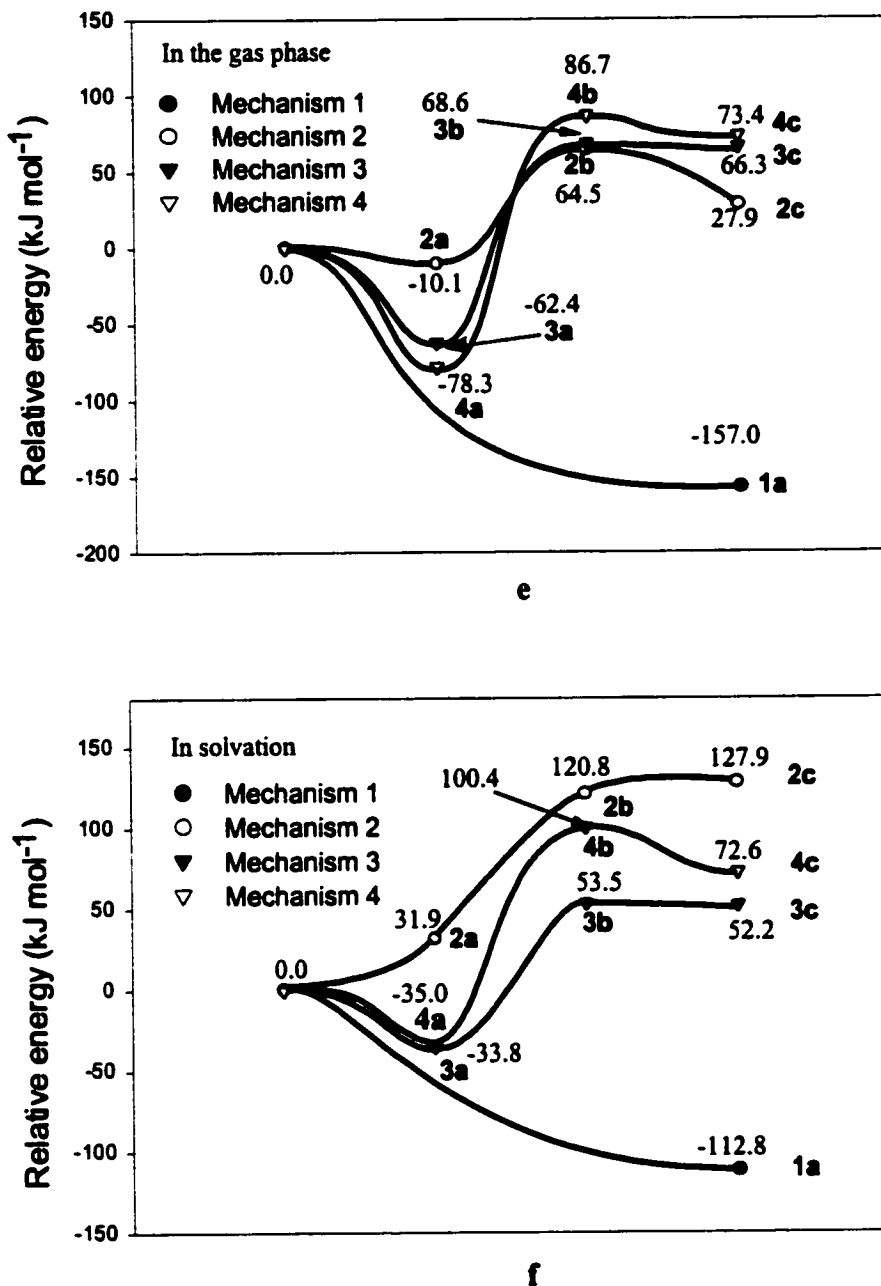
Figure 6.2 Schematic energy profiles for the initial reaction step (a) mechanism 1 (2 + 6), (b) mechanism 2 (2 + 5), (c) mechanism 3 (1 + 6) addition to C_5 of cytosine, (d) mechanism 4 (1 + 6) addition to C_6 of cytosine, (e) summary of mechanisms 1, 2, 3 and 4 in the gas phase, (f) summary of mechanisms 1, 2, 3 and 4 showing the effects of solvent, by inclusion of the PCM model.

The changes of the spin density between the cytosine and the phenol moieties from **2a**, **2b** to **2c** are shown in Table 6.1. Essentially, the interaction between the two moieties is purely electrostatic in **2a** and the spin is entirely on the cytosine moiety. In **2b**, approximately 0.428 of the spin is shifted onto the phenol. In **2c**, approximately 0.926 of the unpaired electron is localized on the phenol ring. In particular, the *meta*-carbons C_2' and C_6' of the phenol possess approximately 0.886 of the total spin density, of which C_6' has the largest spin density of 0.498. Overall, the addition of the Cyt-$C_5OH^\bullet$ radical to phenol shifts the unpaired electron from the cytosine moiety to the *meta*-carbon sites of the phenol ring. The substantially localized double character of the $C_1'=C_2'$ (1.366 Å) and $C_4'=C_5'$ (1.368 Å) bonds suggests that the formation of the C_6—C_3' bond in **2c** deforms the π-conjugation of the phenol ring. As a consequence, the cross-linked product **2c** is higher in energy than the reactant system.

Table 6.1: The spin density partitioning between cytosine and phenol moieties in **2a**, **2b**, **2c**, **3a**, **3b**, **3c**, **4b** and **4c**.

Spin population	2a	2b	2c	3a	3b	3c	4a	4b	4c
Cytosine moiety	0.999	0.512	0.074	-0.002	0.639	0.889	-0.003	0.628	0.950
Phenol moiety	0.001	0.428	0.926	1.002	0.361	0.111	1.003	0.372	0.050

The energy profile for the addition of phenoxyl radical to the C_5 cytosine position is schematically shown in Figure 6.2c. Initially, the phenoxyl oxygen forms a hydrogen bond with the cytosine N_1H (1.996 Å). The resulting reactant complex **3a** lies 62.4 kJ mol^{-1} lower in energy than the isolated reactant system. The formation of the cross-linked product **3c** involves an activation barrier of 131.0 kJ mol^{-1} via TS **3b**. In **3b**, the cytosine C_5 approaches the C_3' of the phenoxyl radical at a distance of 1.862 Å. Product

3c lies 66.3 kJ mol^{-1} higher in energy than the reactant system, and has a weak hydrogen bond (1.937 Å) stabilizing the conformation.

The spin density partitioning between the cytosine and the phenol moieties of **3a**, **3b** and **3c** is shown in Table 1. The spin is essentially localized on the phenoxyl moiety in the reaction complex **3a**, while more than half (0.639) of the unpaired electronic spin is delocalized onto the cytosine ring in the TS **3b**. The formation of the C_5-C_3' bond in product **3c** results in the cytosine ring having a spin density of approximately 0.889, of which 0.698 spin is localized at C_6 of cytosine moiety. The localized double bond character of C_1'= C_2' (1.346 Å) and C_5'=C_6' (1.356 Å) indicates the loss of a delocalized unpaired electron on the phenol ring. Due to the formation of a localized cytosine C_6 radical centre, **3c** is higher in energy than the reactant system.

The energy profile for the addition of the phenoxyl radical to C_6 of cytosine is schematically shown in Figure 6.2d. Phenoxyl radical and cytosine form the intermolecular hydrogen bonded complex **4a** lying 78.3 kJ mol^{-1} lower in energy (Figure 6.2c). The product **4c** is formed via TS **4b** with a barrier of 165.0 kJ mol^{-1}. In **4b**, the C_6 - C_3' distance is 1.915 Å. **4c** lies approximately 73.4 kJ mol^{-1} higher in energy than the reactants. It should be noted, however, that the N_1 position of cytosine is not available in biological systems. Hence, any addition complex will have a different conformation and lie higher on the energy surface than the optimized complex **4a**. The activation energy for passing via TS **4b** will consequently be lower than the present 165.0 kJ mol^{-1} in the full DNA-protein system. Similar changes (Table 6.1) of the spin density between the

cytosine and phenoxyl moieties have been observed from **4a, 4b** to **4c** as from **3a, 3b** to **3c**. However, the spin density of **4c** is now predominantly localized at the C_5 of cytosine.

The product **4c** is approximately 7.1 kJ mol^{-1} higher in energy than the product **3c** (see Figure 6.2c) and, more importantly, TS **4b** is approximately 18.1 kJ mol^{-1} higher in energy than TS **3b**. Thus, the computed energy surfaces suggest that the addition of the tyrosyl radical to cytosine prefers the C_5 site over C_6. Hence, it can be concluded that the addition is electrophilic in nature.

For comparison, the gas phase potential energy surfaces of the initial steps are summarized in Figure 6.2e. As the original experiments were performed in aqueous solution, the solvent effects on the potential energy surface are investigated by B3LYP/6-311G(2df,p) single point calculations using the polarizable continuum model (PCM) with a dielectric constant 78.39 of water. The resulting energy profiles of the four mechanisms in solvation are shown in Figure 6.2f. Solvation reduces the barriers of mechanisms 3 and 4 from 131.0 and 165.0 kJ mol^{-1} to 87.3 and 135.4 kJ mol^{-1}, respectively. In the case of mechanism 2, however, the energy cost required for the formation of **2c** increases from 74.6 kJ mol^{-1} in the gas phase to 127.9 kJ mol^{-1} upon inclusion of solvent. All the solvated products **1a, 2c, 3c** and **4c** have a significantly higher relative energy (-112.8, 127.9, 52.2, and 72.6 kJ mol^{-1}) than in the gas phase (-157.0, 27.9, 66.3 and 73.4 kJ mol^{-1}).

From the calculated energy profiles in both gas phase and in solution, the initial steps of mechanisms 2, 3 and 4 have significant barriers and are thermodynamically unfavourable. The energetically most favourable of these three is mechanism 3 which in

aqueous phase has a TS ca 53 kJ mol^{-1} above the reactants, and where the steric

chemistry of the real system will lift the addition complex significantly above the

computed minimum. However, of the four mechanisms proposed, the preferred

mechanism for producing the cross-link between cytosine and tyrosine is the radical-

radical addition. This is found to proceed without barrier, and is the only mechanism to

provide an exothermic adduct. Thus, for the remainder of this chapter, only possible

reaction steps that may lead to the final product from intermediate product **1a** are

considered.

6.3.3 Mechanisms of the Hydrogen Transfer

After the initial step of the radical-radical combination, three possible

mechanisms of an internal hydrogen transfer from C_3' to O_2' within **1a** (Figure 6.2a) are

considered. Mechanism A: direct hydrogen transfer from C_3' to the O_2'. Mechanism B:

hydrogen transfer from C_3' to O_2' using a water molecule as a bridge. Mechanism C:

concerted hydrogen transfers from C_3' to O_1 and O_1 to O_2' using a water molecule and the

—O_1H_1 group of **1a** as bridges. The computed energy profiles of the three possible

mechanisms are schematically shown in Figures 6.3a-c.

The calculated energy profile of mechanism A is schematically shown in Figure

6.3a. The hydrogen-transferred product **1c** can form via TS **1b** with an activation barrier

of 227.3 kJ mol^{-1}. **1c** is 66.3 kJ mol^{-1} lower in energy than **1a**. This pathway is unlikely

to happen because the barrier is too high.
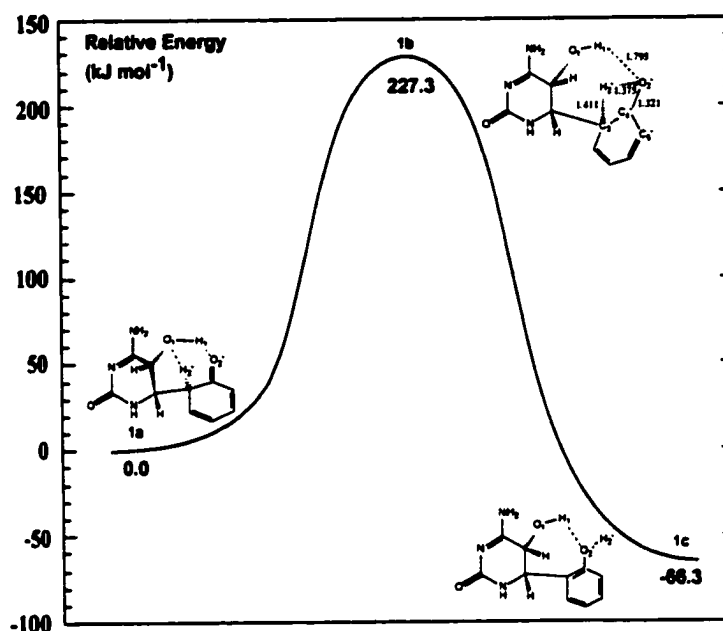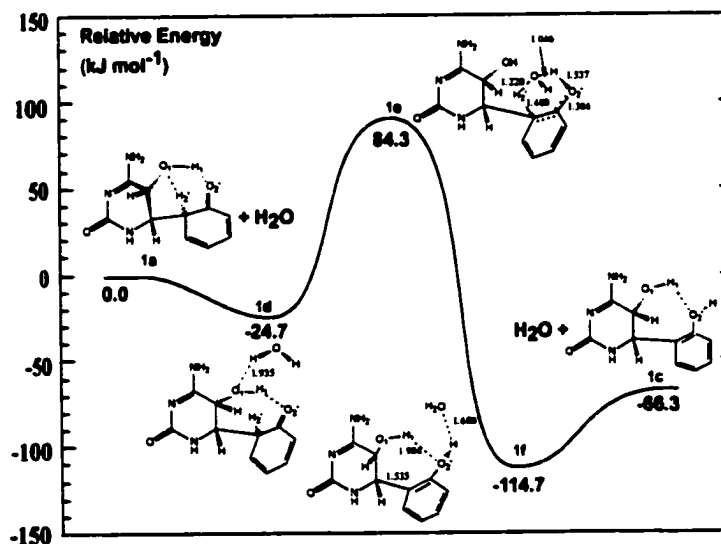
Figure 6.3 Schematic energy profiles of the hydrogen transfer from C_3' to O_2' (a) for mechanism A, (b) for mechanism B and (c) for mechanism C in the gas phase (—) and in the presence of H_2O using PCM solvation (—). (d) Optimized structures of **1g** and **1g'**. (continued over page)
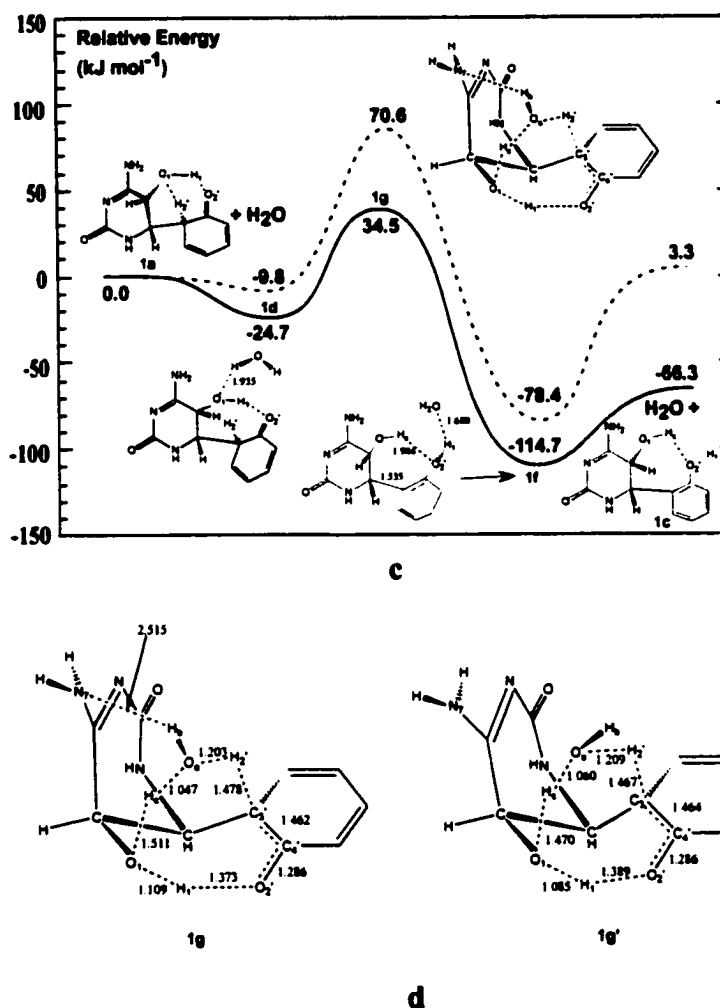
Figure 6.3 Schematic energy profiles of the hydrogen transfer from C₃' to O₂' (a) for mechanism A, (b) for mechanism B and (c) for mechanism C in the gas phase (—) and in the presence of H₂O using PCM solvation (—). (d) Optimized structures of 1g and 1g'.

The structure of TS **1b** suggests that the high barrier is mainly caused by the tension of a four-membered ring C₃'-H₂'-O₂'-C₄'. As the reaction was carried out in aqueous solution, water molecules may be specifically involved in the hydrogen transfer reaction. Thus, mechanism B is proposed in order to investigate the role of a water molecule for the hydrogen transfer.

The computed energy profile of mechanism B is schematically shown in Figure 6.3b. Initially, 1a interacts with a water molecule forming a hydrogen bonded complex 1d lying 24.7 kJ mol^{-1} lower in energy than the isolated reactants. The product complex 1f is formed via a six-membered ring TS 1e. The activation barrier is approximately 109.0 kJ mol^{-1}. As expected it is much lower than the barrier 227.4 kJ mol^{-1} of mechanism A. 1f lies 114.7 kJ mol^{-1} lower in energy. Isolation of the 1c + H_2O from 1f costs 48.4 kJ mol^{-1}. In this particular situation the water molecule clearly acts as a catalyst for the hydrogen transfer. Thus, mechanism B is preferred over mechanism A.

There is a strong hydrogen bonding interaction, with a distance of 1.730 Å, between O_1—H_1 and O_2' of 1a (see Figure 6.2a). For this particular conformation, transfer of H_2' from C_3' to O_1 may induce a simultaneous transfer of H_1 from O_1 to O_2'. This possible mechanism is equivalent to a net hydrogen transfer from C_3' to O_2'. Because the distance between H_2' and O_1 is approximately 2.623 Å, it would be difficult for the direct transfer of H_2' from C_3' to O_1 to take place over such a distance. However, a water molecule may catalyze the transfer of H_2' from C_3' to O_1, similar to what has been found in mechanism B. Thus, the feasibility of the concerted hydrogen transfers along the chain C_3' - O_{water} - O_1 - O_2' of mechanism C is investigated.

The computed energy profile of mechanism C is shown in Figure 6.3c. As mentioned in mechanism B, 1a and a water form the reactant complex 1d lying 24.7 kJ mol^{-1} lower in energy. The formation of the product complex 1f may proceed via TS 1g with a barrier of 59.2 kJ mol^{-1}. The participation of a water molecule and the —$O_1H_1$$\cdots$

O_2' hydrogen bond in the reaction leads to an eight-membered ring structure —C_3'---H_2'---O_a---H_c---O_1---H_1---O_2'---C_4'--- of **1g**. Because TS **1g** is 49.8 kJ mol^{-1} lower in energy than TS **1e**, mechanism C is preferred over mechanism B.

Interestingly, another transition structure **1g'** has also been found for mechanism C. For comparison, the structures of both **1g** and **1g'** are shown in Figure 6.3d. It can be seen that **1g** distinguishes itself from **1g'** by possessing a hydrogen bond between H_b of the water and the N_7 of the cytosine moiety, with a distance of 2.515 Å. **1g** lies 4.2 kJ mol^{-1} lower in energy than **1g'** due to the hydrogen bond between H_b and N_7. Thus, the $H_b\cdots N_7$ hydrogen-bond assists the concerted hydrogen transfers.

Mechanism C is concluded to be the overall preferred mechanism for the hydrogen transfer. In particular, the eight-membered ring structure of **1g** provides new insights for mechanisms of hydrogen transfer in biological systems.

As the original experiments were performed in aqueous solution, the solvent effects on each mechanism have been investigated by performing B3LYP/6-311G(2df,p) single point calculations using the PCM model. The barriers for mechanism A, B and C in solution are 279.1, 114.2 and 80.4 kJ mol^{-1}, which are higher than they are in the gas phase (227.3, 109.0 and 59.2 kJ mol^{-1}). However, mechanism C is the preferred pathway in both the gas phase and in solution. For simplicity, only the energy profile in solution of mechanism C is shown in Figure 6.3c.

6.3.4 Acid-catalyzed Dehydration

Dehydration of **1c** leads to the final cross-linked product. Experimentally, 6 M HCl was added for the dehydration step. It was presumed that dehydration of **1c** is acid-catalyzed. However, the feasibility of acid catalysis for the dehydration depends on the proton affinity of the O_1 of the $—O_1H_c$ group of **1c** in Figure 6.3c. The optimized structure of **1h**, the protonated form of **1c**, is shown in Figure 6.4a.
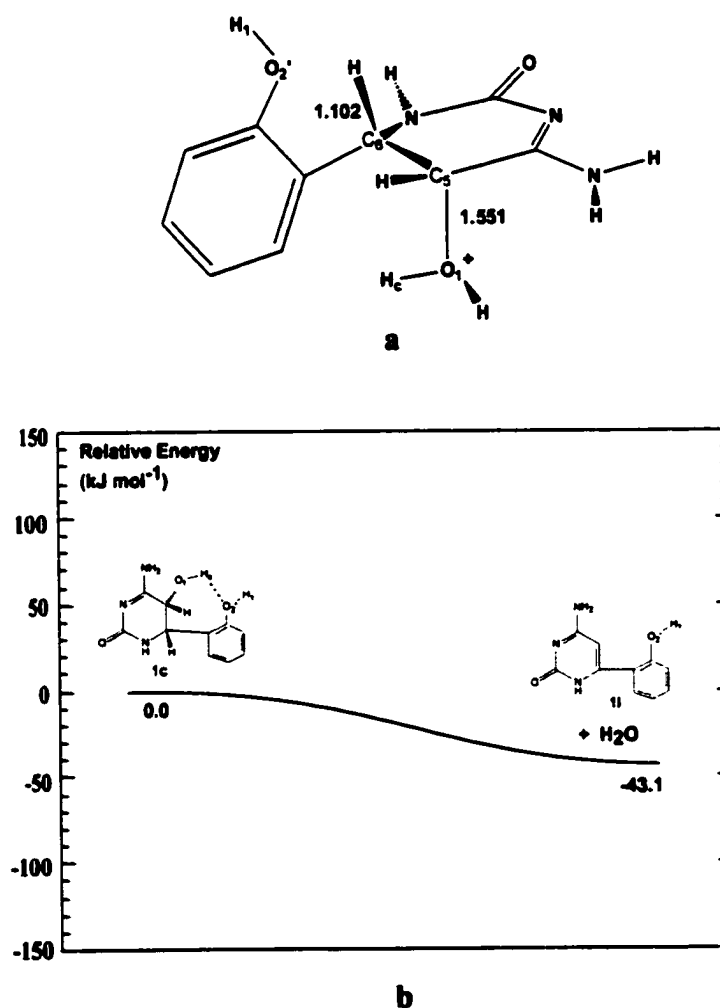

a

b

Figure 6.4 (a) Schematic drawing of **1h**. (b) Schematic energy profile of the dehydration reaction.

The proton affinity of the O_1 site of **1c** is calculated to be 783.0 kJ mol^{-1}; significantly larger than the proton affinity 705.2 kJ mol^{-1} of H_2O at the same level of theory. The magnitude of the computed proton affinity of the O_1 site suggests that the O_1 site is easily protonated under acidic conditions. Thus, the dehydration of **1h** should follow the standard reaction mechanism, involving protonation at O_1, loss of water (H_cO_1H), and deprotonation at C_6. The formation of the final product **1i** via dehydration of **1c** is energetically favoured by 43.1 kJ mol^{-1} as shown in Figure 6.4b.

6.4 Conclusions

The cross-linking reaction mechanisms of the DNA cytosine moiety and the tyrosine residue of protein have been investigated by use of the B3LYP density functional theory method. The reactions are modelled by a smaller reaction system of cytosine and phenol and their derived radicals.

The direct combination of the Cyt-$C_5OH^\bullet$ radical and phenoxyl radical is suggested to be the preferred mechanism with a small or effectively no barrier, while all the radical addition mechanisms examined are suggested to be thermodynamically unfavourable. The cross-linking mechanism identified for the cytosine and tyrosine system in the present study is similar to the experimental findings[9] that the hydroxyl radical-induced cross-linking of the thymine and lysine is dominated by a radical recombination mechanism.

Of the three possible mechanisms considered for the subsequent hydrogen transfer, mechanism C, by which a net hydrogen transfer from C_3' to O_2' of **1a** proceeds by a water assisted chain of concerted hydrogen transfers in transition structure **1g**, is suggested to be the most favoured.

Using the PCM model, it has been found that water has significant solvent effects on the cross-linking mechanisms of cytosine and tyrosine. However, the preferred mechanism is suggested to be the same in both the gas phase and in solution.

References

1. Halliwell, B.; Gutteridge, J. M. C. *Free Radicals in Biology and Medicine*, Oxford University Press Inc.: New York, 1999.

2. Malins, D. C.; Polissar, N. L.; Gunselman, S. J. *Proc. Natl. Acad. Sci.* USA **1996**, *93*, 2557.

3. Ames, B. N.; Shigenaga, M. K.; Hagen, T. M. *Proc. Natl. Acad. Sci.* USA **1993**, *90*, 7915.

4. Loft, S; Poulsen, H. E. *J. Mol. Med.* **1996**, *74*, 297.

5. Totter, T. R. *Proc. Natl. Acad. Sci.* USA **1980**, *77*, 1763.

6. Ohshima, H.; Bartsch, H. *Mut. Res.* **1994**, *305*, 253.

7. Hsiao, K.; Chapman, P.; Nilsen, S.; Eckman, C.; Harigaya, Y.; Younkin, S.; Yang, F. S; Cole, G. *Science* **1996**, *274*, 99.

8. Selkoe, D. J. *Annu. Rev. Cell. Biol.* **1994**, *10*, 373.

9. Youdim, M. B. H.; Riederer, P. *Sci. Am.* **1997**, *276*, 52.

10. Chapman, J. D.; Reuvers, R. P.; Borsa, J.; Greenstock, C. L. *Radiat. Res.* **1973**, *56*, 291.

11. de Lara, C. M.; Jenner, T. J.; Townsend, K. M. S.; Marsden, S. J.; O'Neill, P. *Radiat. Res.* **1995**, *144*, 43.

12. Helbock, H. J.; Beckman, K. B.; Shigenaga, M. K.; Walter, P. B.; Woodall, A. A.; Yeo, H. C.; Ames, B. N. *Proc. Natl. Acad. Sci. USA* **1998**, *95*, 288.

13. von Sonntag, C. *The Chemical Basis of Radiation Biology*, Taylor & Francis: London, 1987.

14. Dizdaroglu, M. *Mutat. Res.* **1992**, *275*, 331.

15. Breen, A. P.; Murphy, J. A. *Free Radic Biol. Med.* **1995**, *18*, 1033.

16. Bourdat, A. G.; Douki, T.; Frelon, S.; Gasparutto, D.; Cadet, J. *J. Am. Chem. Soc.* **2000**, *122*, 4549.

17. Reid, T. M.; Loeb, L. A. *Proc. Natl. Acad. Sci. USA* **1993**, *90*, 3904.

18. (a) Stubbe, J.; van der Donk, W. A. *Chem. Rev.* **1998**, *98*, 705. (b) Stubbe, J. *Annu. Rev. Biochem.* **1989**, *58*, 257. (c) Stubbe, J. *Biochemistry* **1988**, *27*, 3593.

19. Hoganson, C. W.; Sahlin, M.; Sjöberg, B.-M.; Babcock, G.T. *J. Am. Chem. Soc.* **1996**, *118*, 4672.

20. Farrar, C. T.; Gerfen, G. J.; Griffin, R. G.; Force, D. A.; Britt, R. D. *J. Phys. Chem.* B **1997**, *101*, 6634.

21. Dorlet, P.; Boussac, A.; Rutherford, A. W.; Un, S. *J. Phys. Chem.* B **1999**, *103*, 10945.

22. Diner, B. A.; Force, D. A.; Randall, D. W.; Britt, R. D. *Biochemistry* **1998**, *37*, 17931.

23. Xiao, G. S.; Tsai, A. L.; Palmer, G.; Boyar, W. C.; Marshall, P. J.; Kulmacz, R. J. *Biochemistry* **1997**, *36*, 1836.

24. Rauk, A.; Armstrong, D. A. *J. Am. Chem. Soc.* **2000**, *122*, 4185.

25. Shamovsky, I. L.; Riopelle, R. J.; Ross, G. M. *J. Phys. Chem.* A **2001**, *105*, 1061.

26. Dean, R. T.; Fu, S. L.; Stocker, R.; Davies, M. J. *Biochem. J.* **1997**, *324*, 1.

27. Liaw, S. H.; Villafranca, J. J.; Eisenberg, D. *Biochemistry* **1993**, *32*, 7999.

28. Jacob, J. S.; Cistola, D. P.; Hsu, F. F.; Muzaffar, S.; Mueller, D. M.; Hazen, S. L.; Heinecke, J. W. *J. Biol. Chem.* **1996**, *271*, 19950.

29. Oleinick, N. L.; Chiu, S.; Ramakrishnan, N.; Xue, L. *Br. J. Cancer* **1987**, *55*, 135.

30. Mee, L. K; Adelstein, S. J. *Int. J. Radiat. Biol.* **1979**, *36*, 359.

31. Yamamoto, O. in *Aging, Carcinogenesis, and Radiation Biology*, Smith, K.C., Ed.; p165, Plenum: New York, **1976**.

32. Morimoto, S.; Hatta, H.; Fujita, S.; Matsuyama, T.; Ueno, T.; Nishimoto, S. *Bioorg. Med. Chem. Lett.* **1998**, *8*, 865.

33. Nackerdien, Z; Rao, G.; Cacciuttolo, M. A.; Gajewski, E.; Dizdaroglu, M. *Biochemistry* **1991**, *30*, 4873.

34. Gajewski, E.; Dizdaroglu, M. *Biochemistry* **1990**, *29*, 977.

35. Dizdaroglu, M.; Gajewski, E. *Cancer Res.* **1989**, *49*, 3463.

36. Dizdaroglu, M.; Gajewski, E.; Reddy, P.; Margolis, S. A. *Biochemistry* **1989**, *28*, 3625; Margolis, S. A.; Coxon, B.; Gajewski, E.; Dizdaroglu, M. *Biochemistry* **1988**, *27*, 6353.

37. Gajewski, E.; Fuciarelli, A. F.; Dizdaroglu, M. *Int. J. Radiat. Biol.* **1988**, *54*, 445.

38. Charlton, T. S.; Ingelse, B. A.; Black, D. StC.; Craig, D. C.; Mason, K. E.; Duncan, M. W. *Free Rad. Biol. Med.* **1999**, *27*, 254.

39. Hazra, D. K.; Steenken, S. *J. Am. Chem. Soc.* **1983**, *105*, 4380.

40. Solar, S.; Solar, W.; Getoff, N. *J. Phys. Chem.* **1984**, *88*, 2091.

41. Land, E. J.; Ebert, M. *Trans. Faraday Soc.* **1967**, *63*, 1181.

42. Curtiss, L. A.; Redfern, P. C.; Raghavachari, K.; Pople, J. A. *J. Chem. Phys.* **2001**, *114*, 108.

43. Lynch, B. J.; Truhlar, D. G. *J. Phys. Chem.* A **2001**, *105*, 2936.

44. Himo, F.; Siegbahn, P. E. M. *J. Phys. Chem.* B. **2000**, *104*, 7502.

45. Ban, F.; Gauld, J. W.; Boyd, R. J. *J. Am. Chem. Soc.* **2001**, *123*, 7320.

46. (a) Wetmore, S. D.; Boyd, R. J.; Eriksson, L. A. *J. Phys. Chem.* B **1998**, *102*, 5369. (b) Wetmore, S. D.; Himo, F.; Boyd, R. J.; Eriksson, L. A *J. Phys. Chem.* B **1998**, *102*, 7484. (c) Wetmore, S. D.; Boyd, R. J.; Eriksson, L. A *J. Phys. Chem.* B **1998**, *102*, 9332. (d) Wetmore, S. D.; Boyd, R. J.; Eriksson, L. A *J. Phys. Chem.* B **1998**,

102, 10602. (e) Wetmore, S. D.; Boyd, R. J.; Eriksson, L. A. *J. Phys. Chem.* B **1998**, *102*, 7674.

47. Chatgilialoglu, C.; Ferreri, C.; Bazzanini, R.; Guerra, M.; Choi, S.Y.; Emanuel, C. J.; Horner, J. H.; Newcomb, M. *J. Am. Chem. Soc.* **2000**, *122*, 9525.

48. (a) Ban, F.; Gauld, J. W.; Boyd, R. J. *J. Phys. Chem.* A **2000**, *104*, 5080. (b) Ban, F.; Gauld J. W.; Boyd, R. J. *J. Phys. Chem.* A **2000**, *104*, 8583. (c) Ban, F.;Wetmore, S. D.; Boyd, R. J. *J. Phys. Chem.* A **1999**, *103*, 4303. (d) Himo, F.; Gräslund, A.; Eriksson, L. A. *Biophys. J.* **1997**, *72*,1556. (e) Himo, F.; Eriksson, L. A. *J. Phys. Chem.* B **1997**, *101*, 9811. (f) Himo, F.; Babcock, G. T.; Eriksson, L. A. *Chem. Phys. Lett.* **1999**, *313*, 374. (g) Himo, F.; Eriksson, L. A.; Blomberg, M. R. A.; Siegbahn, P. E. M. *Int. J. Quantum. Chem.* **2000**, *76*, 714. (h) Himo, F. *Chem. Phys. Lett.* **2000**, *328*, 270.

49. (a) Lundqvist, M. J.; Eriksson, L. A. *J. Phys. Chem.* B **2000**, *104*, 848. (b) Llano, J.; Eriksson, L. A. *J. Phys. Chem.* B. **1999**, *103*, 5598. (c) Wetmore, S. D.; Boyd, R. J.; Llano, J.; Lundqvist, M. J.; Eriksson, L.A. in *Recent Advances in Density Functional Methods*, Vol. 3, Barone, V.; Bencini, A.; Fantucci, P. Eds.; World Scientific: Singapore, in press.

50. Qin, Y.; Wheeler, R. A. *J. Am. Chem. Soc.* **1995**, *117*, 6083.

51. Ban, F.; Lundqvist, M. J.; Boyd, R. J.; Eriksson, L. A. (submitted for publication).

52. (a) Miertus, S.; Scrocco, E.; Tomasi, J. *Chem. Phys.* **1981**, *55*, 117. (b) Miertus, S.; Tomasi, J. *Chem. Phys.* **1982**, *65*, 239. (c) Cossi, M.; Barone, V.; Cammi, R.; Tomasi, J. *Chem. Phys. Lett.* **1996**, *255*, 237.

53. Cabana, A.; Bachand, J.; Giguere, J. *Can. J. Phys.* **1974**, *52*, 1949.

54. (a) Steenken, S.; O'Neill, P. *J. Phys. Chem.* **1978**, *82*, 372. (b) Anbar, M.; Neta, P. *J. Phys. Chem.* **1966**, *70*, 2660.

55. Raghavan, N. V.; Steenken, S. *J. Am. Chem. Soc.* **1980**, *102*, 3495.

56. Chipman, D. M.; Liu, R.; Zhou, X.; Pulay, P. *J. Chem. Phys.* **1994**, *100*, 5023.

57. Hagen, K.; Hedberg, K. *J. Chem. Phys.* **1973**, *59*, 158.

58. Portalone, G.; Schultz, G.; Domenicano, A.; Hargittai, I. *Chem. Phys. Lett.* **1992**, *197*, 482.

59. Hulsebosch, R. J.; van den Brink, J. S.; Nieuwenhuis, S. A. M.; Gast, P.; Raap, J.; Lugtenburg, J.; Hoff, A. J. *J. Am. Chem. Soc.* **1997**, *119*, 8685.

Modelling the Action of an Antitumor Drug: Tirapazamine

7.1 Introduction

A unique feature of many cancerous tumors is the existence of hypoxic regions, that is, regions of oxygen-poor cells.[1-3] Such cells are often quite resistant to more conventional forms of antitumor treatment such as radiotherapy and chemotherapy.[4] Consequently, there has been considerable effort to identify potential antitumor drugs that specifically target such cells. One such class of potential hypoxia-specific drugs is the benzotriazine di-*N*-oxides of which a particularly promising candidate is 3-amino-1,2,4-benzotriazine-1,4-dioxide,[5-7] or tirapazamine (shown in Scheme 7.1).
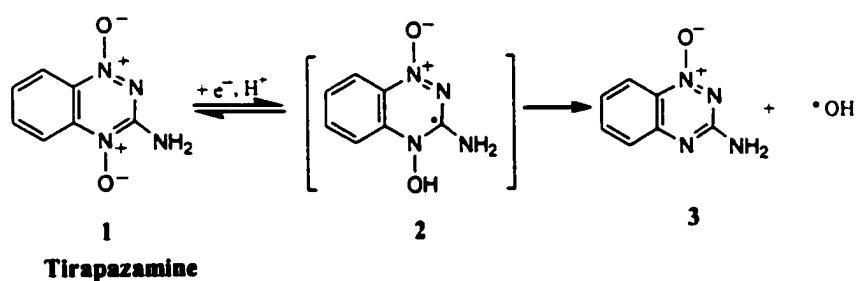
Scheme 7.1 Schematic illustration of the activation of tirapazamine by one-electron enzymatic reduction.

Tirapazamine has been the subject of extensive experimental investigations,[8-11] and has been shown to derive its biological activity from its ability to cause DNA

cleavage in hypoxic tumor cells. It is known that in vivo, under hypoxic conditions, tirapazamine may undergo an enzymatic one-electron reduction to form the activated intermediate **2**, see Scheme 7.1. It has been proposed that **2** may abstract hydrogen directly from DNA.[7] However, it has been found that **2** decomposes to **3** releasing a hydroxyl radical, and it has been suggested[11] that both **2** and •OH are involved in DNA cleavage. In either case, a sugar-C_1' radical is formed which then reacts further to give the corresponding deoxyribonolactone (Scheme 7.2) and the DNA strand is cleaved. However, radical-mediated DNA cleavage depends on molecular oxygen.[12] Thus, the involvement of **2** and •OH does not explain the remarkable selectivity of tirapazamine towards hypoxic tumor cells.
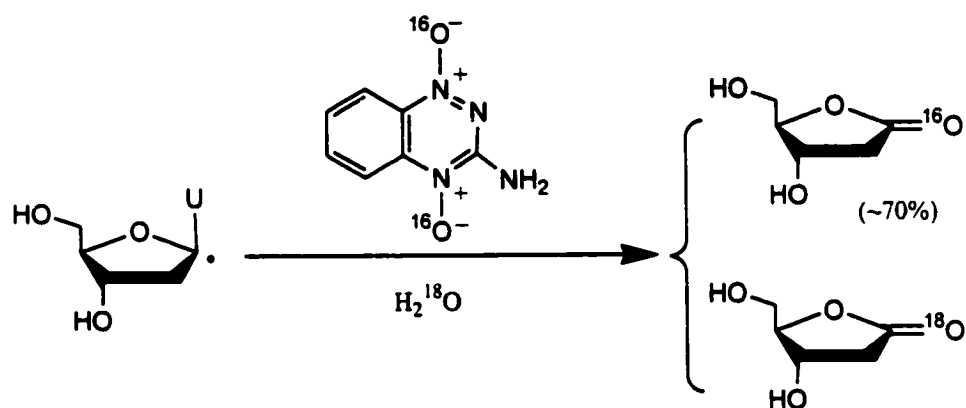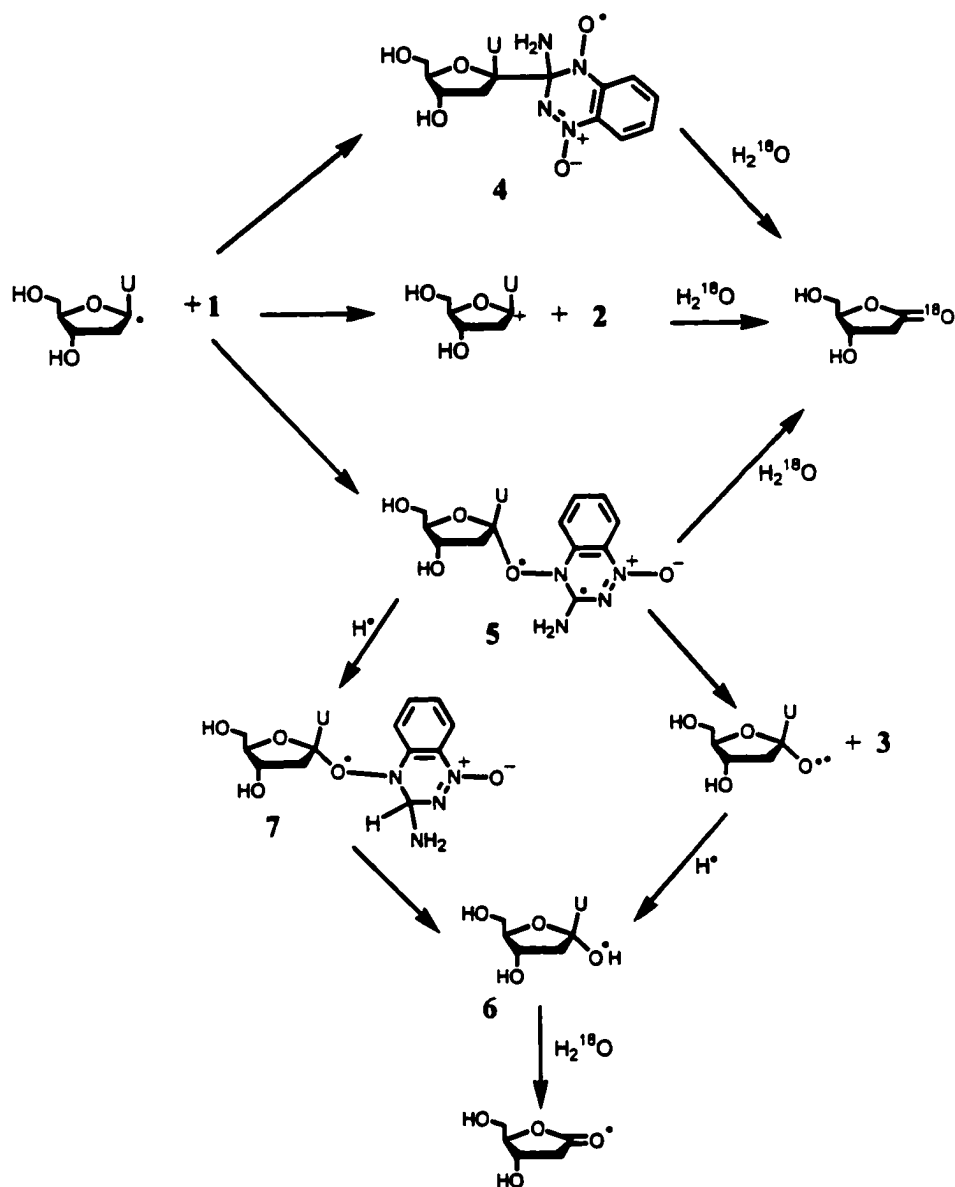

Scheme 7.2 Schematic illustration of the product distribution for the reaction of tirapazamine with a sugar-C_1' DNA radical.

Experimentally, it has been suggested[8,10] that for DNA exposed to γ-radiolysis, the presence of tirapazamine increases the amount of strand cleavage. Hence, it has been proposed that tirapazamine may act as a molecular oxygen surrogate or mimic in radical-

mediated DNA damage reactions. Hwang et al.[10] have performed a systematic experimental study of the reaction of tirapazamine with sugar-C_1' DNA radicals. From oxygen isotope labelled product analysis of the final deoxyribonolactone it was found that the reaction proceeds predominantly by direct transfer of an N-oxide oxygen, in particular the O_4 oxygen, of the tirapazamine moiety to the sugar-C_1' radical. Only a minor amount was derived from direct attack of H_2O at the sugar-C_1' position (Scheme 7.2).

For the observed predominant direct oxygen transfer, Hwang et al. and coworkers[10] proposed the formation of the sugar-drug covalent adduct intermediate 5, which may then react further by two possible mechanisms (see Scheme 7.3). In one mechanism, the cross-linked N—O bond of intermediate 5 cleaves to produce an alkoxyl radical. Subsequent reduction of the alkoxyl radical forms the sugar-derived species 6 which can then hydrolyse to produce the corresponding deoxyribonolactone which leads to cleavage of the DNA strand. In the alternative mechanism, an initial reduction of 5 occurs to give the neutral intermediate 7. The cross-linked N—O bond then breaks, and hydrogen transfer to the oxygen of the now cleaved N—O bond gives the sugar-derived species 6 which, as described above, can then react further to give deoxyribonolactone and DNA strand cleavage. However, experiments do not differentiate between the two proposed reaction mechanisms.

Scheme 7.3 Schematic illustration of the experimentally proposed mechanisms for the reaction of the sugar-C_1' radical with tirapazamine.

For the minor pathway, Hwang et al.[10] suggested that it may indicate an electron-transfer mechanism by which the sugar-C_1' radical activates tirapazamine, i.e., via formation of a sugar-C_1' cation intermediate. However, the exact mechanisms by which such an electron transfer may occur were unclear. It has been suggested[8] that the minor

pathway may proceed via the carbon-carbon covalent adduct intermediate 4, or that the reaction may possibly occur via the carbon-oxygen covalent adduct intermediate 5 (see Scheme 7.3).[10]

The reliability and computational efficiency of DFT methods offers an attractive theoretical approach to gain insight into large biological systems. Numerous biological radicals derived from the DNA bases,[13a-d] sugar moiety[13e,14] and amino acids[15] have been extensively studied using density functional theory. In the present study, density functional theory methods have been used to investigate the possible mechanisms by which tirapazamine may act as a surrogate for molecular oxygen in radical-mediated DNA cleavage.[16] At the levels of theory employed in the present study, the reactions of 2'-deoxyuridin-1'-yl radical with tirapazamine were modelled by 8 and 9, respectively (Figure 7.1).
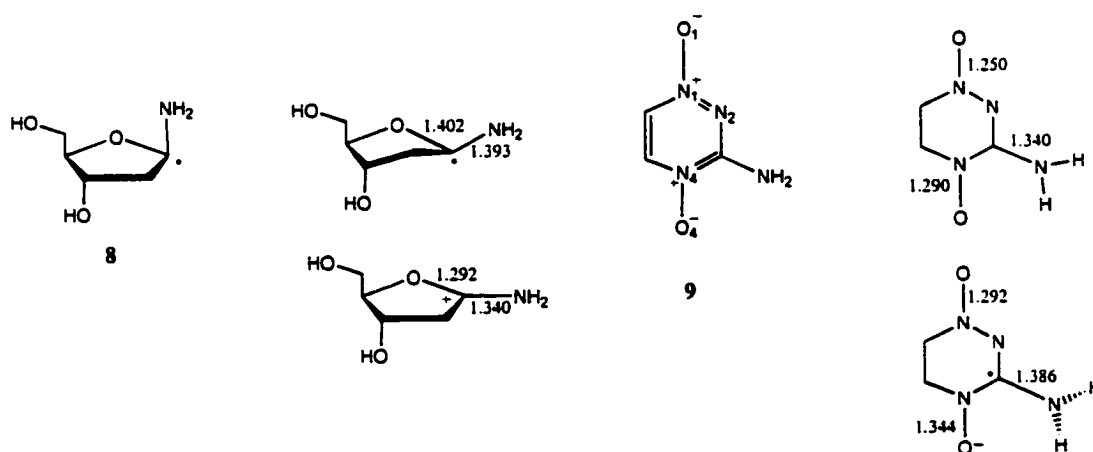

Figure 7.1 The model systems 8 and 9 used in place of 2'-deoxyuridin-1'-yl radical and tirapazamine, respectively. Selected optimized parameters of the neutral and cationic forms of 8 and the neutral and anionic forms of 9 are also shown.

7.2 Computational Methods

All geometry optimizations were performed with the B3LYP hybrid density functional in conjunction with the 6-31G(d) basis set using the GAUSSIAN 98 suite of programs. Harmonic vibrational frequencies and zero-point vibrational energy (ZPVE) corrections were calculated at the same level of theory. Relative energies were obtained by performing single point calculations at the B3LYP level in conjunction with the 6-311G(d,p) basis set using the above optimized geometries and with inclusion of the appropriate scaled[17] ZPVE, i.e., B3LYP/6-311G(d,p)//B3LYP/6-31G(d) + ZPVE.

For all open- and closed-shell systems, the unrestricted (UB3LYP) and restricted (RB3LYP) B3LYP procedures were used, respectively. The symbols U and R have been neglected for simplicity.

7.3 Results and Discussion

7.3.1 Oxidation of the Sugar-C_1' Radical by Tirapazamine

Hwang et al.[10] suggested that the sugar-C_1' radical may be oxidized by tirapazamine to form the sugar-C_1' cation. The feasibility of electron-transfer from the sugar-C_1' radical to tirapazamine was probed by comparing the calculated ionization energy of 8 and the calculated electron affinity of 9.

The optimized structures of the sugar-C_1' neutral radical **8** and its cation, and of

the neutral drug **9** and its anion are shown in Figure 7.1. The sugar-C_1' radical centre of **8**

is pyramidal by approximately 36°, while the sugar-C_1' centre of the corresponding cation

is planar. The shortened C—N and C—O bonds in the cation indicate the presence of

strong π-electron delocalization across the O—C—N moiety. The optimized structure of

9 is a conjugated system with an almost planar structure. In the corresponding anion,

however, O_4 protrudes out of the plane of the six-membered 1,2,4-triazine ring by

approximately 4° while the amino group is pyramidal. In both neutral **9** and the anion,

the two N—O bonds differ with the N_1—O_1 bond having relatively more double bond

character than the N_4—O_4 bond.

The calculated ionization potential for the sugar-C_1' radical **8** is 459.9 kJ mol^{-1},

while the calculated electron affinity of **9** is just 60.7 kJ mol^{-1}. Hence, due to the very

large difference between the ionization potential of **8** and electron affinity of **9**, it is

unlikely that the sugar-C_1' radical can be oxidized by tirapazamine alone. The effect of

protonation on the ability of tirapazamine to oxidize the sugar radical was investigated by

comparing the electron affinity of protonated **9** with the ionization potential of **8**. The

calculated proton affinity (PA) of the O_4 site of **9** is quite large, approximately 896.4 kJ

mol^{-1}, suggesting that tirapazamine may be easily protonated. The calculated electron

affinity of protonated **9** is 588.4 kJ mol^{-1}. Comparison with the calculated ionization

potential (459.9 kJ mol^{-1}) for the sugar-C_1' radical **8** suggests that protonated

tirapazamine is more likely to be able to oxidize the sugar-C_1' radical to produce the

corresponding cation.

It must be noted, however, that the present calculations are performed without inclusion of solvent effects; they are gas-phase calculations. An experimental study[18] of the pK_a values of tirapazamine-related N-oxide species suggested that in fact, tirapazamine may not be protonated under physiological conditions.

7.3.2 Formation of Deoxyribonolactone via a C—C Covalent Adduct Intermediate

Possible reaction mechanisms by which the deoxyribonolactone moiety may be formed via some covalent adduct intermediate were also examined. The triazine ring of tirapazamine possesses several possible sites at which the sugar-C_1' radical may attack and form a covalently cross-linked product. The mechanism for formation of a sugar-C_1'—triazine-C_3 cross-linked intermediate was investigated and the energy profiles are schematically shown in Figure 7.2.

The addition of the drug (9) to the sugar-C_1' radical (8) leads to the formation of the hydrogen-bonded complex 1a, lying 23.3 kJ mol^{-1} lower in energy than the initial reactants (Figure 7.2a). The C—C cross-linked product 1c can then be formed by attack of the sugar-C_1' radical at the C_3 position of the 1,2,4-triazine ring via transition structure (TS) 1b, at a cost of 34.1 kJ mol^{-1}. It should be noted that TS 1b lies higher in energy than the initial reactants by 10.8 kJ mol^{-1}. The product 1c, which is effectively a model of species 4 in Scheme 7.3, lies 28.4 kJ mol^{-1} lower in energy than the initial reactants, and the radical centre is now localized on the O_4 N-oxide oxygen.
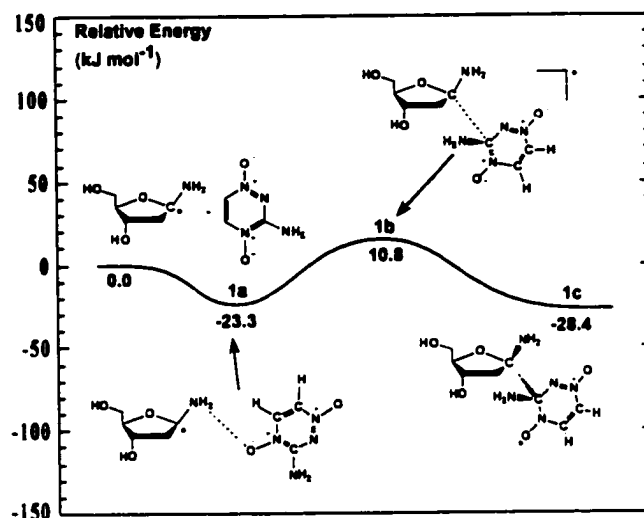
a
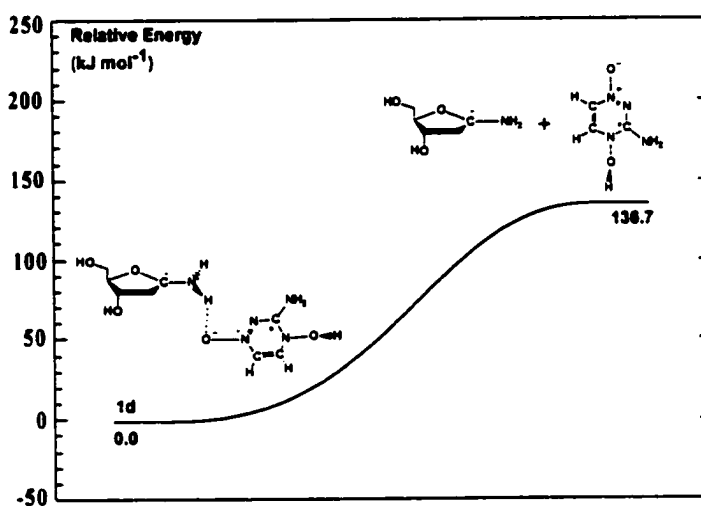
b

Figure 7.2 Schematic energy profile for the formation of (a) the carbon-carbon cross-linked product, and (b) the sugar-C_1' cation via decomposition of the complex 1c.

All attempts to locate possible transition structures for cleavage of the C—C bond of 1c by hydrolysis, i.e., by attack of H_2O at the sugar-C_1' or triazine-C_3 positions or by addition across the C_1'—C_3 bond, were unsuccessful. An alternative possible mechanism

is that the C—C cross-link bond may break heterolytically to give the corresponding sugar cation and 3-amino-1,2,4-triazine radical anion. However, as described above, the triazine moiety has a relatively low electron affinity while that of its protonated derivative is considerably higher. Thus, the effects of protonation on the C—C covalent adduct **1c**, more specifically protonation at the O_4 site, were examined.

Upon protonation, **1c** was calculated to dissociate without a barrier to form the complex **1d**, which is illustrated schematically in Figure 7.2b. Complex **1d** is an intermolecularly hydrogen-bonded complex between the sugar-C_1' cation and what can be thought of as the protonated derivative of the 3-amino-1,2,4-triazine anion. In other words, protonation of the C—C covalent adduct **1c** at O_4 induces an intramolecular redox reaction, with an electron transfer from the sugar to the drug moiety and cleavage of the sugar-C_1'—drug-C_3 bond.

Energetically, the dissociation of **1c** to give **1d** upon addition of a proton at the O_4 position is favoured by approximately 1133.1 kJ mol^{-1} (not shown), indicating a large proton affinity for **1c**. At the present level of theory, the proton affinity of H_2O is calculated to be approximately 700 kJ mol^{-1}. Thus, the considerably larger proton affinity of **1c** suggests that once formed it may be easily protonated with little or no barrier to give **1d**. As mentioned above, the present calculations neglect the effects of solvation. However, from an experimental study[18] of the pK_a values of tirapazamine-related radical species, the radicals were more likely to be protonated under physiological conditions than their closed-shell parents. Furthermore, they suggested that the observed values may be due to protonation of the N-oxide oxygen rather than at a nitrogen. The

dissociation of complex **1d** to the sugar-C_1' cation and drug derivative (see Figure 7.2b) is calculated to require approximately 136.7 kJ mol^{-1}. The inclusion of solvent effects would stabilize to a greater extent the dissociated products than **1d**, thus giving a lower dissociation energy. The above results suggest that the decomposition of **1c** may be an alternative *indirect* oxidation reaction pathway for the generation of the sugar-C_1' cation.

The resulting fate of the sugar-C_1' cation is still a matter of much discussion.[19,20] Hence, possible reactions by which the sugar-C_1' cation may react directly with H_2O to give the resulting deoxyribonolactone were also investigated.

7.3.3 Formation of Deoxyribonolactone by Reaction of H_2O with the Sugar-C_1' Cation.

For the model system, the addition of a single water molecule to the sugar-C_1' cation results in the formation of complex **1e**, lying lower in energy by 47.1 kJ mol^{-1} (Figure 7.3a). The hydrolyzed product **1g** is formed by the addition of the water across the C—N bond via TS **1f**, at a cost of approximately 178.6 kJ mol^{-1}. **1g** lies 19.8 kJ mol^{-1} higher in energy than the initial reactants. The high barrier for the hydrolysis of the sugar-C_1' cation by a single water is probably due in part to the need to form a tight four-membered ring in TS **1f**. Thus, the reaction of the sugar-C_1' cation with two H_2O molecules was considered, as one may act as a base to enhance the nucleophilicity of the other, or may assist in stabilizing transition structures or intermediates.
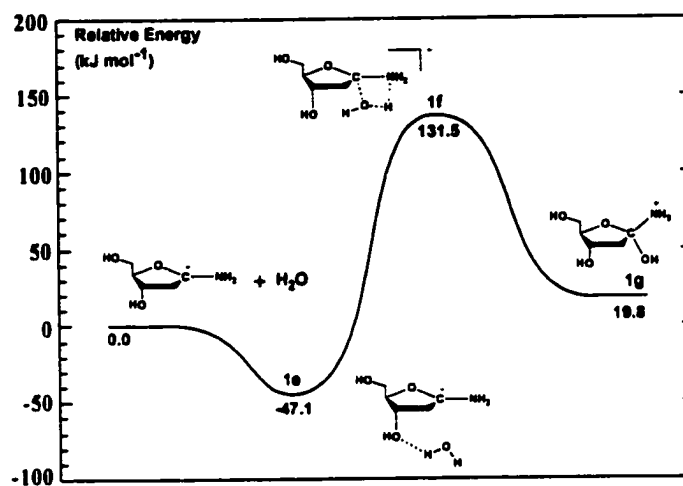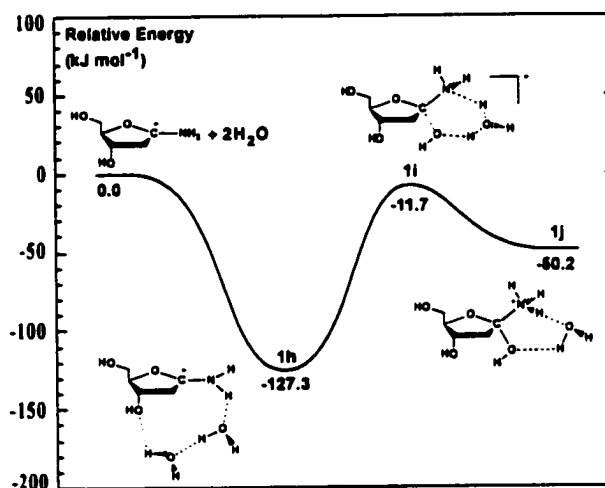
Figure 7.3 Schematic energy profiles for the reaction of the sugar-C_1' cation with (a) one water molecule and (b) with two water molecules.

Upon addition of two H_2O to the sugar-C_1' cation, they are able to form complex

1h (Figure 7.3b), which lies lower in energy than the initial reactants by approximately

127.3 kJ mol^{-1}. In complex **1h**, the two water molecules have formed a hydrogen-bond

bridge between the amine group at C_1' and with the –OH group at C_3'. Addition of a

water across the C—N bond assisted by another water is then able to proceed via TS **1i**,

with a barrier of 115.6 kJ mol^{-1}. The final complex formed, **1j**, lies approximately 50.2

kJ mol^{-1} lower in energy than the initial reactants. In TS **1i** it can be seen that one H_2O

moiety acts as a proton donor to the amine N, while concomitantly acting as a proton

acceptor from the H_2O moiety that is attacking the C_1' centre (see Figure 7.3b). It should

also be noted that TS **1i** lies 11.7 kJ mol^{-1} lower in energy than the initial reactants. Thus,

it is possible for complex **1j** to be formed directly from the initial reactants via TS **1i**,

without passing through **1h**. Comparison of the above energetics of the mechanisms for

hydrolysis by one and two H_2O molecules, also provides a very clear example of the

effect of explicitly including greater solvent effects for some processes. In order to

simplify the calculations performed to determine the fate of complex **1j**, the complexed

H_2O moiety in **1j** was neglected, i.e., only reactions of **1g** were considered (see Figure

7.4).

The C_1'—NH_3 bond of **1g** may be cleaved via TS **1k** with a barrier of just 11.4 kJ

mol^{-1} to give the complex **1l**, lower in energy than **1g** by 5 kJ mol^{-1}. The leaving NH_3

group may then abstract a proton from the C_1'—OH group to give the

deoxyribonolactone···NH_4^+ complex **1m**, lying 111.8 kJ mol^{-1} lower in energy than **1g**.

At the present level of theory, no transition structure interconnecting **1l** and **1m** could be

located (as indicated by the hashed line in Figure 7.4). However, in **1j** the NH_3 moiety is only weakly complexed to the sugar-C_1' centre ($r(C_1'\cdots NH_3)$ = 2.702 Å) and is almost perpendicular to the $-OH^+$ group ($\angle N-C_1'-OH$ = 90.8°). Thus, it is most likely that any transition structure interconnecting **1l** and **1m** will have quite small barriers (Figure 7.4). This may also explain the difficulty in locating the transition structure.
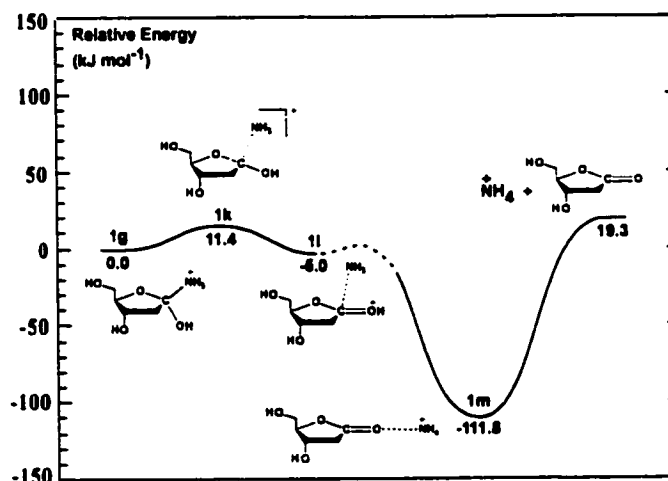

Figure 7.4 Schematic energy profile for formation of deoxyribonolactone from the protonated sugar-C_1' hydroxylated derivative.

The present calculations show the reaction of the model system cation with one and two water moieties. In DNA itself, the reactions may differ due to the presence of more solvent and the nature of the nucleobase. Such calculations are not practical at the present level of theory. However, the end result of the reaction of the cation with water will be the same: formation of the deoxyribonolactone.

7.3.4 Formation of Deoxyribonolactone via a C—O Covalent Adduct Intermediate.

The predominant mechanism for formation of the deoxyribonolactone moiety was proposed to occur via direct attack, and transfer, of an N-oxide oxygen of tirapazamine, see Introduction (Scheme 7.3). In particular, it was proposed to occur by formation of a bond between the sugar-C_1' radical and tirapazamine via O_4, 5, which could then react further to eventually give deoxyribonolactone. However, no such covalent adduct intermediate was experimentally observed and furthermore, the exact mechanisms by which it may eventually form deoxyribonolactone were unclear. Thus, the mechanism for formation of the proposed C_1'—O_4 covalent adduct intermediate was investigated.

As mentioned previously, when the sugar-C_1' radical and drug interact they can form the intermolecularly hydrogen-bonded complex 1a lying 23.3 kJ mol^{-1} lower in energy (Figure 7.5). The O_4 N-oxide oxygen can then attack the sugar-C_1' radical site via TS 2a, at a cost of just 16.3 kJ mol^{-1}, to give the C_1'—O_4 covalent adduct intermediate 2b which lies considerably lower in energy by approximately 67.4 kJ mol^{-1}.

Possible reactions of the C—O covalent adduct intermediate 2b were then examined. In particular, formation of the deoxyribonolactone moiety via homolytic cleavage of the O_4—N_4 bond (mechanism A) and via addition of hydrogen (H$^{\bullet}$) to the drug-C_3 radical site of 2b (mechanism B) was investigated. These two mechanisms are the same as those proposed by Hwang et al. (see Scheme 7.3).[10] In addition, considering

the previous findings for the C—C covalent adduct intermediate **1c**, the effects of protonation on **2b** (**mechanism C**) were also examined.
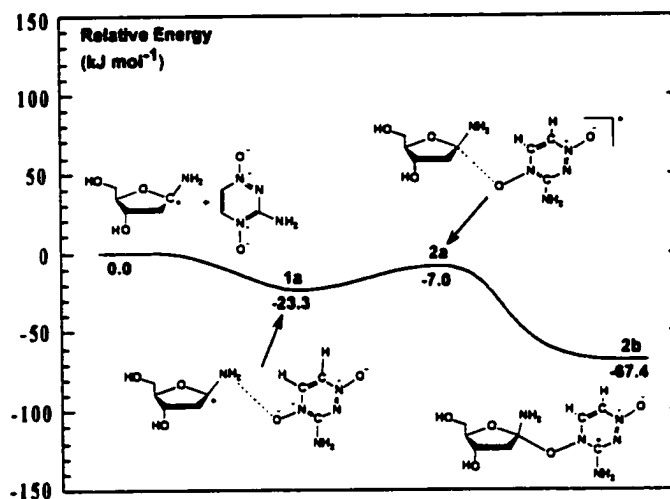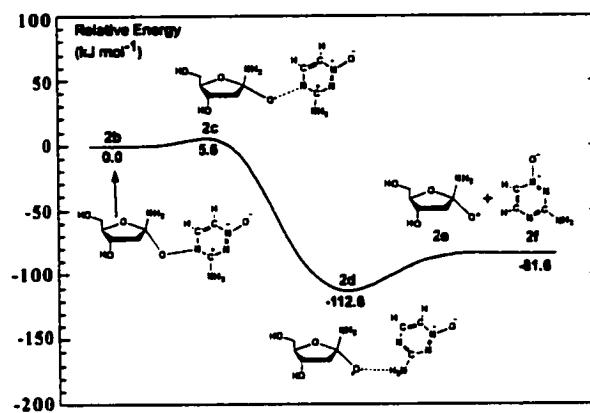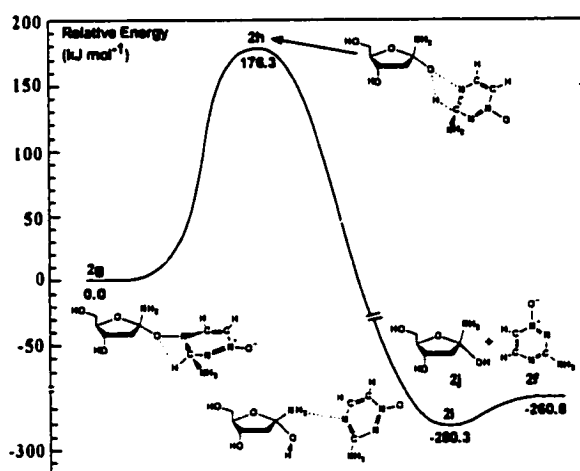

Figure 7.5 Schematic energy profile for the formation of the carbon-oxygen cross-linked intermediate.

The schematic energy profile obtained for **mechanism A** is shown in Figure 7.6a. The O_4—N_4 bond of **2b** may cleave homolytically via TS **2c** at a cost of just 5.6 kJ mol^{-1}, to give complex **2d**, lying lower in energy than **2b** by 112.6 kJ mol^{-1}. Complex **2d** is an intermolecularly hydrogen-bonded complex between the alkoxyl radical derivative (**2e**) of the sugar-C_1' radical and the drug metabolite (**2f**). The small barrier to dissociation of **2c** may suggest why the C—O covalent adduct intermediate **5** (see Scheme 7.3) was not observed experimentally. **2f** corresponds to the model equivalent of **3** (see Scheme 7.1). It requires just 31.0 kJ mol^{-1} for **2d** to dissociate completely to **2e** and **2f**.
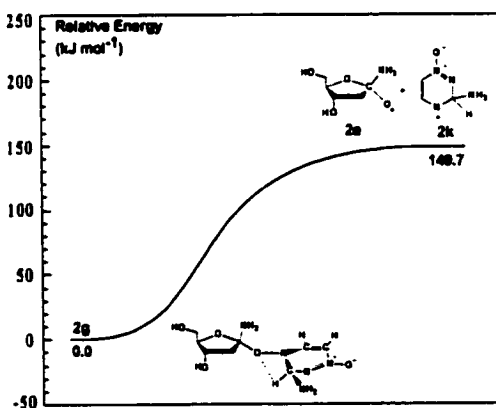
Figure 7.6 Schematic energy profile for (a) mechanism A, (b) for mechanism B (part A) and (c) mechanism B (part B) (see text).

The calculated hydrogen affinity of the alkoxyl radical **2e** is quite large, approximately 420.5 kJ mol^{-1}. This suggests that such a radical species may relatively easily obtain a hydrogen to form the sugar-C$_1$' hydroxylated species, **6** in Scheme 7.3. Once the hydroxylated species is formed it may then react further to give the corresponding deoxyribonolactone, with concomitant cleavage of the DNA backbone.

For the proposed[10] alternative, **mechanism B**, the calculated hydrogen affinity for the drug-C$_3$ centred radical **2b** is just 241.3 kJ mol^{-1}. This is quite a low hydrogen affinity on account of the enhanced stability of the ring-carbon centred radical. Furthermore, it is significantly lower than that of the alkoxyl radical **2e**. This suggests that such a process may encounter a considerable energy barrier, as predicted by the empirical relationships of Evans-Polanyi and Semenov.[21] For completeness, however, the reactions that the hydrogenated derivative **7** (see Scheme 7.3) may undergo to give the deoxyribonolactone moiety was considered. The addition of hydrogen (H$^{\bullet}$) to the drug-C$_3$ radical centre of **2b** gives **2g** in Figure 7.6b. The schematic energy profiles obtained for further reactions of **2g** are shown in Figure 7.6b (part A of mechanism B) for the formation of a sugar-C$_1$' hydroxylated derivative **2j**, and in Figure 7.6c (part B of mechanism B) for the formation of the sugar alkoxyl radical **2e**. In Figure 7.6b, an intermolecularly hydrogen-bonded complex **2i** between the sugar-C$_1$' hydroxylated derivative (**2j**) and **2f** can form, lying lower in energy by 280.3 kJ mol^{-1}! However, this reaction proceeds via TS **2h** at a considerable cost of 176.3 kJ mol^{-1}. Thus, even if **2g** were formed, it is unlikely that such a reaction will occur. Alternatively, the O$_4$—N$_4$ bond of **2g** may undergo homolytic cleavage at a cost of 149.7 kJ mol^{-1} to give the

alkoxyl radical (2e) and the radical drug derivative 2k (Figure 7.6c). While this alternative mechanism still requires a considerable amount of energy, it is significantly less than that required for formation of 2i from 2g. The alkoxyl radical formed can then react as described previously to eventually form deoxyribonolactone.

The protonation of 2b (mechanism C) can conceivably occur at several sites on the drug moiety, in particular at the O_1 or O_4 positions. Protonation at the bridging O_4 position results in cleavage of the O_4—N_4 bond to give the sugar-C_1' hydroxylated derivative 2j, while protonation at the O_1 position results in a shortening of the O_4—N_4 bond and a lengthening of the sugar-C_1'—O_4 bond of 2b, i.e., emphasises the sugar–drug nature of 2b. As might be expected, the calculated proton affinity of O_1 (1029.0 kJ mol^{-1}) is higher than that of the bridging O_4 (975.6 kJ mol^{-1}). Thus, while protonation of 2b is not expected to enhance the ability of tirapazamine to transfer an oxygen to the sugar-C_1' radical, it is not expected to inhibit or lead to radically different reaction mechanisms than those already considered above.

7.4 Conclusions

Possible mechanisms by which tirapazamine may react with DNA sugar-C_1' radicals to form the sugar derivative deoxyribonolactone with concomitant cleavage of the DNA strand, have been investigated by use of the B3LYP density functional theory method.

Experimentally proposed mechanisms involving ionization of the sugar-C_1' radical by tirapazamine were investigated. The present results predict the electron affinity of tirapazamine to be considerably lower than the ionization energy of the sugar-C_1' radical. Thus, it is unlikely that the sugar-C_1' radical can be oxidized by tirapazamine. However, the electron affinity of the protonated form of tirapazamine is estimated to be greater than the ionization energy of the sugar-C_1' radical. Hence, protonation of tirapazamine may be a prerequisite for it to oxidize the sugar-C_1' radical.

The proposed formation of a sugar-C_1'—drug-C_3 covalent adduct intermediate 4 is found to occur with a modest barrier. Protonation of the drug moiety of 4 is predicted to result in heterolytic cleavage of the C—C bond, without a barrier, to give the sugar-C_1' cation.

In both of these above mechanisms, the resulting sugar-C_1' cation will react with solution H_2O to give deoxyribonolactone with inclusion of an oxygen from H_2O. At the present level of theory, it is impossible to distinguish which mechanism may be responsible for the experimentally observed minor pathway; the conversion of a sugar-C_1' radical to deoxyribonolactone by incorporation of an oxygen from a solution H_2O molecule. It is possible that both mechanisms occur to different degrees.

The energetically preferred pathway, in agreement with the experimental observations, occurs via direct attachment of the O_4 N-oxide oxygen of tirapazamine at the sugar-C_1' radical centre. This is predicted to be able to occur without a barrier. The transfer of the oxygen O_4 can then be completed by homolytic cleavage of the O_4—N_4 bond, which proceeds with a very small barrier of less than 6 kJ mol^{-1}. The resulting

sugar-alkoxyl radical derivative can then relatively easily obtain a hydrogen to form the sugar-C_1' hydroxylated derivative, which can then react further to give the deoxyribonolactone. The present calculations suggest this to be the preferred mechanism for formation of the experimentally observed major product; formation of the deoxyribonolactone by incorporation of an N-oxide oxygen. The experimentally proposed alternative, involving addition of H$^\bullet$ to the drug-C_3 position of the sugar-C_1'— O_4-drug intermediate **5**, is predicted to not occur due to the low hydrogen affinity of **5**.

References

1. Vaupel, P; Kallinowski, F.; Okunieff, P. *Cancer Res.* **1989**, *49*, 6449.

2. Horsman, M. R. *Int. J. Radiat. Oncol., Biol., Phys.* **1998**, *42*, 701.

3. Brown, J. M. *Cancer Res.* **1999**, *59*, 5863.

4. Denny, W. A.; Wilson, W. R. *Expert Opin. Inv. Drug.* **2000**, *9*, 2889.

5. Brown, J. M.; Siim, B. G. *Semin. Radiat. Oncol.* **1996**, *6*, 22.

6. Brown, J. M.; Wang, L. H. *Anti-Cancer Drug Des.* **1998**, *13*, 529.

7. Brown, J. M. *Br. J. Cancer Res.* **1993**, *67*, 1163.

8. Daniels, J. S.; Gates, K. S.; Tronche, C.; Greenberg, M. W. *Chem. Res. Toxicol.* **1998**, *11*, 1254.

9. Daniels, J. S.; Chatterji, T.; MacGillivray, L. R.; Gates, K. S. *J. Org. Chem.* **1998**, *63*, 10027.

10. Hwang, J.; Greenberg, M. M.; Fuchs, T.; Gates, K. S. *Biochemistry* **1999**, *38*, 14248.

11. Daniels, J. S.; Gates, K. S. *J. Am. Chem. Soc.* **1996**, *118*, 3380.

12. Pogozelski, W. K.; Tullius, T. D. *Chem. Rev.* **1998**, *98*, 1089.

13. (a) Wetmore, S. D.; Boyd, R. J.; Eriksson, L. A. *J. Phys. Chem.* B **1998**, *102*, 5369.
(b) Wetmore, S. D.; Himo, F.; Boyd, R. J.; Eriksson, L. A. *J. Phys. Chem.* B **1998**, *102*, 7484. (c) Wetmore, S. D.; Boyd, R. J.; Eriksson, L. A. *J. Phys. Chem.* B **1998**, *102*, 9332. (d) Wetmore, S. D.; Boyd, R. J.; Eriksson, L. A. *J. Phys. Chem.* B **1998**, *102*, 10602. (e) Wetmore, S. D.; Boyd, R. J.; Eriksson, L. A. *J. Phys. Chem.* B **1998**, *102*, 7674.

14. Chatgilialoglu, C.; Ferreri, C.; Bazzanini, R.; Guerra, M.; Choi, S.; Emanuel, C. J.; Horner, J. H.; Newcomb, M. *J. Am. Chem. Soc.* **2000**, *122*, 9525.

15. (a) Ban, F.; Gauld, J. W.; Boyd, R. J. *J. Phys. Chem.* A **2000**, *104*, 5080. (b) Ban, F.; Wetmore, S. D.; Boyd, R. J. *J. Phys. Chem.* A **1999**, *103*, 4303. (c) Ban, F.; Gauld J. W.; Boyd, R. J. *J. Phys. Chem.* A **2000**, *104*, 8583.

16. Ban, F.; Gauld, J. W.; Boyd, R. J. *J. Am. Chem. Soc.* **2001**, in press.

17. Scott, A. P.; Radom, L. *J. Phys. Chem.* **1996**, *100*, 16502.

18. Priyadarsini, K. I.; Dennis, M. F.; Naylor, M. A.; Stratford, M. R. L.; Wardman, P. *J. Am. Chem. Soc.* **1996**, *118*, 5648.

19. Meijler, M. M.; Zelenko, O.; Sigman, D. S. *J. Am. Chem. Soc.* **1997**, *119*, 1135.

20. Oyoshi, T.; Sugiyama, H. *J. Am. Chem. Soc.* **2000**, *122*, 6313.

21. See, for example, Laidler, K. J. *Chemical Kinetics;* 3rd ed.; HarperCollins Publishers, Inc.: New York, 1987; p 71.

Concluding Remarks and Future Directions

The computational studies in this thesis have focused on the hyperfine coupling

constants and reaction mechanisms of biological radicals. This chapter summarizes the

global conclusions of the thesis and highlights some possible avenues for future research.

8.1 Amino Acid-derived Radicals

The current studies on the hyperfine coupling constants of amino acid-derived

radicals presented a systematic approach for theoretical characterization of the identities

of the radicals observed from electron spin resonance spectroscopy. The diversity of the

structures of amino acid-derived radicals presented in Chapters 3, 4 and 5 clearly reveals

that the complex ESR spectra for a given radical arise from various possible

conformations. The computational scheme of density functional theory combined with

the Onsager model has been validated for modelling the zwitterionic forms of amino

acid-derived radicals. The reliability of density functional theory in predicting the

hyperfine coupling constants has been demonstrated by the excellent agreement between

the calculated values and the accurate experimental data available for the amino acid

derived-radicals. Comprehensive theoretical assignment of the observed hyperfine

tensors for R2 of glycine (Chapter 3) and for $R1^A$, $R1^P$ and R5 of hydroxyproline

(Chapter 5) are complementary to previous experimental studies. The size and

complexity of the hydroxyproline-derived radicals illustrates the usefulness and power of theoretical predictions.

Biological radical systems are characterized by specificity in structure. Quantum chemical calculations on isolated amino acid-derived radicals of the gas phase can only go as far as shown in this thesis to describe the origin of the structural specificity. The cases where theory and experiment were not in as close agreement, such as $NH_2C^{\bullet}HCOOH$ (Chapter 3) and $R2^C$ of hydroxyproline (Chapter 5), illustrate the limitations of calculations based on the assumption of small models in the gas phase.

A possible future extension of the present study on the hyperfine coupling properties of amino acid-derived radicals could be the validation of computational schemes for describing the crystal effects on the conformations and therefore, the hyperfine coupling constants of a target radical embedded in extended model systems. Computationally, the DFT + SCRF strategy[1] or the ONIOM method[2] are potentially effective. With the DFT + SCRF strategy for an extended model, the most important neighbour molecules of the target are explicitly included and treated at the same electronic level of theory as applied to the target, while the macroscopic environmental effects are incorporated into the SCRF method. In the ONIOM method, an essentially complete model, such as a unit cell, can be used. However, the large model system is divided into different layers according to their contributions to the properties in question, and the target layer is treated with a high level of theory, while the other layers are modelled with lower levels of theory to reduce computational cost. Such computational

strategies for investigations of biological systems in condensed phases are being tested on prototypical applications.

8.2 Mechanisms of Biological Radical Reactions

The mechanistic studies of DNA—protein cross-links (Chapter 6), and the modelling of the actions of tirapazamine (Chapter 7) have provided great insight into the reactions of biological radical systems. The advantages of computational chemistry are illustrated by the quantitative predictions of molecular structures, charge and spin distributions, energy profiles and activation energies. For example, the advantages of theoretical studies can be seen in the concerted hydrogen transfer mechanism (Chapter 6); without obtaining the optimized structure of the intermediate product 1a, chemists were unlikely to foresee such a alternative reaction pathway. Hence, as experimental investigations often provide only indirect information, a complete picture of the reaction mechanisms of interest can be drawn with the tools of computational chemistry.

The study of the cross-linking mechanisms between cytosine and tyrosine can be extended to other cross-linking systems such as thymine with tyrosine or lysine in nucleohistones.[3,4] As the formation of tyrosyl radicals has been recognized as a typical feature of oxidative stress in physiological conditions, and the coupling between tyrosyl radicals is believed to be a prime marker of oxidative stress in many diseases,[5] further research on the reaction mechanisms[6] of the reactions between tyrosyl radicals is of great importance.

The present study of tirapazamine represents the first computational investigation of an antitumor drug at such a high level of theory. As described in Chapter 7, the energetically preferred pathway occurs via direct attachment of the O_4 N-oxide oxygen of tirapazamine to the sugar-C_1' radical centre. The transfer of the O_4 oxygen can then be completed by homolytic cleavage of the O_4—N_4 bond. In addition to elucidating the reaction mechanism for such an important antitumor drug, such studies also give greater insight into the chemistry of N-oxide compounds and thus potentially other drugs.

A possible future extension of the present study on tirapazamine could be a systematic study of related representatives of N-oxide family compounds.[7] In particular, the mono-N-oxide metabolites 1 and 2 shown in Figure 8.1 are of particular interest. The detection of 1 and 2 has suggested that both of the N-oxide oxygens of tirapazmine possess similar reactivity with regards to cleavage of DNA strands. A complete computational study of one N-oxide oxygen of tirapazamine has been presented in the thesis. The reactivity of the other oxygen could be investigated. Of 1 and 2, the major metabolite is 1. Importantly, 1 and 2 are more reactive for inducing DNA strand cleavage than the parent drug. However, the possible reaction mechanisms by which this may occur are uncertain. Moreover, 1 is found to react with the sugar-C_1' radical in single strand DNA three times faster than 2, however, 2 is two times more efficient than 1 in double strand DNA. Thus, further theoretical work could be carried out for exploring this related chemistry.
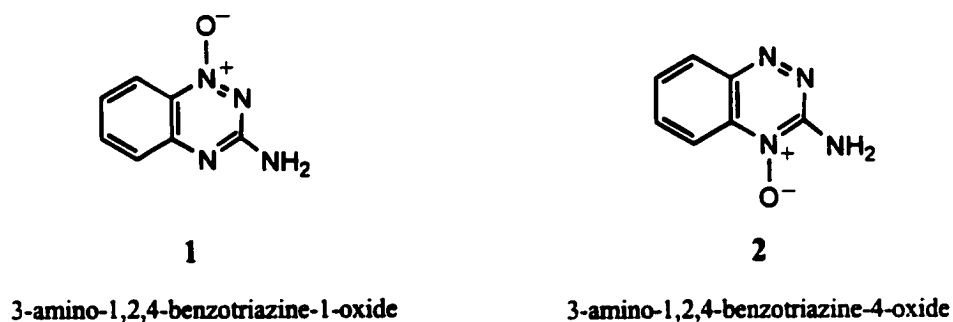
1

3-amino-1,2,4-benzotriazine-1-oxide

2

3-amino-1,2,4-benzotriazine-4-oxide

Figure 8.1   The metabolites of tirapazamine.

8.3 Outlook

At the present stage, high-level electronic structure calculations have only just started to be employed for solving the problems of biological radical systems at a realistic scale. Its best applications have been on the prediction of molecular properties, such as hyperfine coupling constants. Modelling the configurations of biological radical systems with inclusion of the effects of the environment from hydrogen bonding, van der Waals and steric interactions remains a great challenge to theoretical studies. However, an increasing amount of work with model systems at the DFT level of theory has appeared in the literature.[8,9]

The work presented in this thesis clearly illustrates the strengths of density functional theory in modelling the properties and reactions of biological radical systems. There is a potentially endless number of interesting questions to be answered for biological radicals. With the advancement of new methodologies in computational

chemistry and the development of faster computer architectures, the dream of reliable and accurate large-scale quantum mechanical calculations[10] on biological radical systems will increasingly become a reality,

References

1. (a) Rega, N.; Cossi, M.; Barone, V. *J. Am. Chem. Soc.* **1998**, *120*, 5723. (b) Adamo, C.; Cossi, M.; Rega, N.; Barone, V. In *Theoretical Biochemistry: Processes and Properties of Biological Systems*, Eriksson, L. A. Ed.; Elsevier: Amsterdam, 2001.

2. (a) Humbel, S.; Sieber, S.; Morokuma, K. *J. Chem. Phys.* **1996**, *105*, 1959. (b) Svensson, M.; Humbel, S.; Froese, R. D. J.; Matsubara, T.; Sieber, S.; Morokuma, K. *J. Phys. Chem.* **1996**, *100*, 19357. (c) Matsubara, T.; Maseras, F.; Koga, N.; Morokuma, K. *J. Phys. Chem.* **1996**, *100*, 2573.

3. Dizdaroglu, M.; Gajewski, E. *Cancer Res.* **1989**, *49*, 3463.

4. Morimoto, S.; Hatta, H.; Fujita, S.; Matsuyama, T.; Ueno, T.; Nishimoto, S. *Bioorg. Med. Chem. Lett.* **1998**, *8*, 856.

5. (a) Jacob, J. S.; Cistola, D. P.; Hsu, F. F.; Muzaffar, S.; Mueller, D. M.; Hazen, S. L.; Heinecke, J. W. *J. Biol. Chem.* **1996**, *271*, 19950. (b) Souza, J. M.; Giasson, B. I.; Chen, Q.; Lee, V. M.; Ischiropoulos, H. *J. Biol. Chem.* **2000**, *275*, 18344. (c) Leeuwenburgh, C.; Hansen, P. A.; Holloszy, J. O.; Heinecke, J. W. *Free Radical Biol. Med.* **1999**, *27*, 186.

6. Shamovsky, I. L.; Riopelle, R. J.; Ross, G. M. *J. Phys. Chem. A* **2001**, *105*, 1061.

7. Hwang, J.; Greenberg, M. M.; Fuchs, T.; Gates, K. S. *Biochemistry* **1999**, *38*, 14248.

8. Rankin, K. N.; Gauld, J. W.; Boyd, R. J. *J. Am. Chem. Soc.* **2001**, *123*, 2047.

9. Himo, F.; Siegbahn, P. E. M. *J. Phys. Chem. B* **2000**, *104*, 7502.

10. Friesner, R. A.; Dunietz, B. D. *Acc. Chem. Res.* **2001**, *34*, 351.